



BRNO UNIVERSITY OF TECHNOLOGY

VYSOKÉ UČENÍ TECHNICKÉ V BRNĚ

FACULTY OF MECHANICAL ENGINEERING

FAKULTA STROJNÍHO INŽENÝRSTVÍ

INSTITUTE OF PHYSICAL ENGINEERING

ÚSTAV FYZIKÁLNÍHO INŽENÝRSTVÍ

ROLE OF PLASTICITY IN NITINOL FATIGUE

ÚLOHA PLASTICITY V ÚNAVĚ NITINOLU

DOCTORAL THESIS

DIZERTAČNÍ PRÁCE

AUTHOR

AUTOR PRÁCE

Pejman Shayanfard

SUPERVISOR

ŠKOLITEL

prof. RNDr. Pavel Šandera, CSc.

CO-SUPERVISOR

ŠKOLITEL-SPECIALISTA

doc. Ing. Jana Horníková, Ph.D.

Ing. Luděk Heller, Ph.D.

RNDr. Petr Šittner, Ph.D.

BRNO 2020

Abstrakt

Disertace analyzuje vliv koncentrátorů napětí na průběh martensitické transformace, vznik plastické deformace a její vliv na přerozdělení napětí a vznik zbytkového pnutí a reziduálního martenzitu v okolí koncentrátorů v prvcích ze slitin s tvarovou pamětí NiTi. Vliv je analyzován v režimech superelastického isothermálního cyklování a aktuálního cyklování, t.j. teplotního cyklování pod vnějším napětím. Disertace využívá pro vyhodnocení vlivu experimentální přístup spolu s numerickými simulacemi metodou konečných prvků na modelových případech tenkých pásků ze slitin NiTi opatřených půlkruhovou vrubem. V experimentální části je vyhodnocován vliv koncentrátorů pomocí termomechanických experimentů s využitím metod obrazové korelace a rentgenové mikrodifrakce pro lokální analýzu deformací a fázových objemových podílů v průběhu cyklování v okolí vrubů. Simulace metodou konečných prvků poskytují komplementární informace o průběhu napětí, deformací a martensitické transformaci, zejména o vývoji jednotlivých složek celkové deformace, tj. elastické a plastické, a vývoji zbytkového pnutí a s ním souvisejícím zbytkovým martensitem. Disertace je dále doplněna o numerickou analýzu vlivu konstrukce stentů na lokální cyklický průběh martensitické transformace a jeho vliv na únavové vlastnosti.

Klíčová slova:

Napětíové koncentrátoři, Slitiny s tvarovou pamětí, Cyklické zatěžování, Superelastická, Tvarová paměť, Digitální obrazová korelace, Metoda konečných prvků

Abstract

This doctoral thesis deals with the analysis of the role of stress risers in NiTi elements on the local cyclic evolutions of martensitic transformation, plastic deformations, and mechanical gradients at the stress risers, under both iso-thermal cyclic loading in the superelastic regime and thermal cycling under external load in actuator regime. The methodology of investigation includes both experimental measurements and finite element simulations of notched thin NiTi superelastic/shape-memory ribbons. In the experimental part of the work, the DIC method is used to capture the spatial evolutions of strain gradients around the notch, and the X-ray microdiffraction is used to analyze the local strain fields around the notch and the plasticity induced remnant martensite at the notch-tip. Besides, the finite element results help assess the corresponding evolutions of stresses and strains, martensitic transformation, and the partitioning of total strains into elastic, plastic and residual strains around the notch. In addition, the thesis includes numerical analysis investigating the effect of the design of self-expanding NiTi stents on local cyclic evolution of martensitic transformation and its relation to fatigue performance.

Keywords:

Stress riser, Shape memory alloy, Cyclic loading, Superelasticity, Shape memory, Digital Image Correlation, Finite element method

Shayanfard, P. The Role of Plasticity in NiTi Fatigue. Brno: Brno University of Technology, Faculty of Mechanical Engineering, Institute of Physical Engineering, 2020. Doctoral thesis. 144 p. Supervisor Professor Pavel Sandera.

I declare that this thesis has been composed by myself under the guidance of my supervisor and that it has not been submitted, in whole or in part, in any previous application for a degree. Any secondary sources and contributions from colleagues in the collaboration are explicitly referenced in the text.

.....
In Brno

.....
Pejman Shayanfard

Contents

CHAPTER 1. INTRODUCTION	8
1.1. STATEMENT OF THE PROBLEM	8
1.1.1. <i>Initiation and propagation of fatigue cracks</i>	14
1.2. THESIS OUTLINE	15
CHAPTER 2. STATE OF THE ART	16
2.1. MARTENSITIC PHASE TRANSFORMATION IN NiTi ALLOYS	16
1.1.2. <i>Shape memory effect</i>	16
1.1.1. <i>Superelasticity</i>	18
2.1. NONEQUILIBRIUM STRESS-TEMPERATURE PHASE DIAGRAM OF SHAPE MEMORY ALLOYS	18
2.2. APPLICATIONS OF NiTi ALLOYS	19
1.1.2. <i>Superelastic NiTi (SE)</i>	19
2.2.1. <i>Shape Memory NiTi</i>	22
2.3. FATIGUE OF NiTi ALLOYS	23
1.1.3. <i>Structural Fatigue</i>	24
1.1.4. <i>Functional fatigue: Unrecovered Strains</i>	29
2.4. STRESS RAISERS IN PHASE TRANSFORMING NiTi	34
1.1.5. <i>Monotonic Loading</i>	34
1.1.6. <i>Fatigue Crack Growth</i>	43
CHAPTER 3. MATERIALS AND METHODS	47
3.1. INTRODUCTION	47
3.2. EXPERIMENTS	47
3.2.1. <i>Superelastic NiTi Notched Thin Ribbon</i>	47
3.2.2. <i>Shape Memory NiTi Notched Thin Ribbon</i>	48
3.3. NUMERICAL ANALYSIS	49
3.3.1. <i>Three Dimensional Macroscopic SMA Material Model</i>	49
3.3.2. <i>The Experimentally derived material parameters</i>	51
CHAPTER 4. SUPERELASTIC NOTCHED NITI RIBBON: THE EFFECTS OF MARTENSITIC TRANSFORMATION AND PLASTICITY ON THE CYCLIC EVOLUTIONS OF MECHANICAL GRADIENTS	54
4.1. INTRODUCTION	54
4.2. NUMERICAL SIMULATIONS METHOD	54
4.3. RESULTS AND DISCUSSION σ	56
4.3.1. <i>Ideal_SMA, First Loading Stage: comparison between FE and experimental DIC results</i>	56
4.3.2. <i>Plastic_SMA, First Loading Stage: comparison between FE and experimental DIC results</i>	59
4.3.3. <i>Cyclic Response</i>	64
4.3.1. <i>Fractography</i>	70
4.4. CONCLUSIONS	72
CHAPTER 5. SUPERELASTIC NOTCHED NITI RIBBON: THE EFFECTS OF MARTENSITIC TRANSFORMATION AND PLASTICITY ON THE STRESS CONCENTRATION FACTOR	73
5.1. INTRODUCTION	73
CHAPTER 6. NITI ACTUATORS WITH STRESS RISERS: ROLE OF PLASTICITY	74
6.1. NUMERICAL SIMULATION METHOD	74
6.2. RESULTS AND DISCUSSION	75

6.2.1.	<i>The evolution of the inhomogeneous martensitic transformation (MT) upon cooling-heating</i>	75
6.2.2.	<i>Cyclic Response</i>	81
CONCLUSIONS		85
CHAPTER 7. NITI ACTUATORS WITH STRESS RISERS: ROLE OF BIAS LOAD AND ACTUATION TEMPERATURE		87
7.1.	INTRODUCTION	87
CHAPTER 8. NITI SELF-EXPANDING STENTS: A FINITE ELEMENT ANALYSIS		89
8.1.	INTRODUCTION	89
8.2.	MATERIALS AND METHODS	91
8.2.1.	<i>Models and Geometry</i>	92
8.2.2.	<i>Boundary conditions</i>	94
8.3.	RESULTS AND DISCUSSION	94
8.4.	CONCLUSIONS	98
REFERENCES		99
ANNEX I		109
ANNEX II		118
ANNEX III		130
ANNEX IV		133
ANNEX V		140

CHAPTER 1. INTRODUCTION

Shape memory alloys are a specific group of metallic alloys exhibiting outstanding thermomechanical behaviors that are not seen in conventional alloys, due to a solid-state diffusionless reversible phase transformation between martensite (M) and austenite (A) consisting in the recoverable shear distortion of the crystal lattice, known as martensitic transformation. When deformed at high temperatures in the austenitic state, these alloys can recover inelastic strains up to ~40 times higher than that of steel, which is called pseudoelasticity (PE). When deformed at low temperatures in the martensitic state, unloaded and heated above austenite finish temperature without constraint, these alloys recover their original shape, which is called shape memory effect (SME). Pseudoelastic SMAs are frequently used in applications requiring large reversible deformations as in superelastic dampers [1] or superelastic medical implants [2,3], while shape memory elements are used in shape memory thermal actuators (SMTA). Among a variety of available SMA alloys, NiTi alloys remain to be a preferred choice for SMA engineering applications thanks to their good workability, biocompatibility, structural properties, and excellent stability of functional properties.

SMA elements working in applications involving cyclic and complex loadings are prone to fatigue and preliminary fracture. This represents a problem for many promising applications which motivates the need to analyze the mechanisms of fatigue and fracture. This is a problem particularly to NiTi alloys exhibiting otherwise excellent properties in comparison to other SMAs. When a NiTi element undergoes cyclic mechanical loading involving back and forth phase transformations, it withstands only some thousands of tensile cycles in the best-case scheme. This fatigue performance contrasts with the millions of cycles that one may obtain in the absence of phase transformations (though much smaller recoverable strain). The martensitic phase transformation in NiTi is thus, on one hand, a source of the reversibility of very large strains, but on the other hand, it seems to be responsible for early failure of NiTi structures, although the scientific community lacks a fundamental understanding on how the structural damage initiates and proceeds through the material.

In this regard, the role played by strain localization induced at stress raisers in conjunction with phase transformation in the evolution of the local mechanical gradients and initiation of cracks and their subsequent propagation remains unclear. Moreover, the effect of the plastic deformation at high-stress levels well beyond the transformation stress plateau has also a strong influence. Recently, the origin of superelastic fatigue and fracture became focused in the SMA field. However, the role of martensitic transformation and plastic deformation in localized deformation around stress risers has not been addressed in the fatigue and fracture analysis of SMA components.

1.1. Statement of the problem

Stress raisers can either initially exist in SMA structures (as the micro-defects induced by manufacturing processes), or can nucleate under monotonic/cyclic loading conditions. An example is the decohesion of the second particles or local cyclic plastic deformations. Besides, from a physical point of view, there is a question of why SMAs withstand millions of cycles when they deform elastically but only thousands of cycles if the martensitic transformation is incorporated in their cyclic deformation under the stress, even though the martensitic transformation is reversible. One of the probabilities is the nucleation and propagation of cracks from the root of stress raisers since the local evolution of the martensitic transformation and mechanical fields are entirely different at the high-

stress zones at stress raisers than that being experienced within the elastic bulk. Thus, the successful performance of SMA elements in engineering applications needs analysis and understanding of the localized-like cyclic/monotonic evolution of martensitic transformation and plastic deformation at the location of stress raisers.

In conventional elastoplastic materials, fatigue cracks nucleate at the surface due to local cyclic plastic deformations and grow which is the origin of the fatigue degradation and failure [4,5]. In the case of phase transforming NiTi, the micro and macro-mechanisms that lead to fatigue failure are not well known yet. The experimental evidence available in the literature suggests that cycled NiTi samples that undergo partial or complete stress-induced phase transformation between austenite and martensite suffer from premature fatigue and failure after few thousands of cycles, while NiTi samples deforming only elastically (in austenite or martensite phase), exhibit long fatigue life in millions of cycles. But there are no “local cyclic plastic deformations” at the surface which could explain the difference, both deformation mechanisms (elasticity and martensitic transformation) are completely reversible.

Accordingly, we consider that the roles of martensitic transformations and (in particular) plastic deformation remain unclear despite the growing amount of data concerning the fracture and fatigue of NiTi reported in the literature in the last decades. This becomes even more unclear and critical when the transformation and plasticity effects are considered in conjunction with strain and stress localization either induced by material behavior (by the development of the Lüders-like Martensite Band Fronts (MBFs)) or geometric stress risers (concentrators).

It is a peculiarity of polycrystalline NiTi, that the stress-induced martensitic transformation tends to localize in macroscopic deformation band fronts (MBFs) stretching over a large number of grains, which separate the elastically deformed austenite from the microstructure formed by highly strained martensite [6,7,16–19,8–15] (Fig. 1-1). This means that the stress-induced martensitic transformation, possibly accompanied by plastic deformation via dislocation slip, occurs in a particular grain only when the macroscopic MBF passes over it, while nothing happens in grains out of the MBFs. While the grains within the highly deformed Lüders-like band are almost fully transformed to the oriented martensite (M^d), the grains in the low-strain zone outside the band remain in austenite [17]. The volume fraction of martensite within the Luder band depends on the microstructure and test temperature [20]. Originally, it was thought that this macroscopic strain localization occurs only in tension since homogenous deformation occurs in compression. However, this is not the case, since macroscopic localized deformation bands were observed in bending, twisting, and other deformation modes. Also, it is known that the number of MBF increases with increasing the strain rate (Fig. 1-2) which is due to the latent heat generation/absorption and heat exchange with the environment [21].

This macroscopic strain localization becomes a problem tensile-tensile cyclic deformation because large deformation occurs locally even if small deformation is prescribed externally, which turns in a low cycle fatigue failure in places where MBFs move. On the contrary, if the cyclic deformation is homogeneous (without the band front motion) the material shows a much larger number of cycles till failure in low cycles fatigue experiments. This is demonstrated in figure 3. NiTi ribbon cycled in tension with a moderate mean strain (e.g. $\epsilon_{mean} = 3.5\%$) and large nominal strain amplitudes (e.g. in Cases I-V, Fig. 1-3a) show about 200 cycles till failure regardless of the applied strain amplitude. In this regime, the stress-plateaus exist on the stress-strain curves and the MBFs move to/from

particular sample locations. Parts of the sample cyclically swept by the moving fronts are illustrated in Fig. 1-3b while others remain loaded only elastically. The grains within the active zones undergo repeated $A \rightarrow M$ phase transformation and local cyclic strain $\varepsilon_M \approx 6\%$, which turns into a large microstructural damage accumulation there, while no damage occurs elsewhere. With decreasing external strain amplitude (cases IV-VI), as the area of the active zones decrease

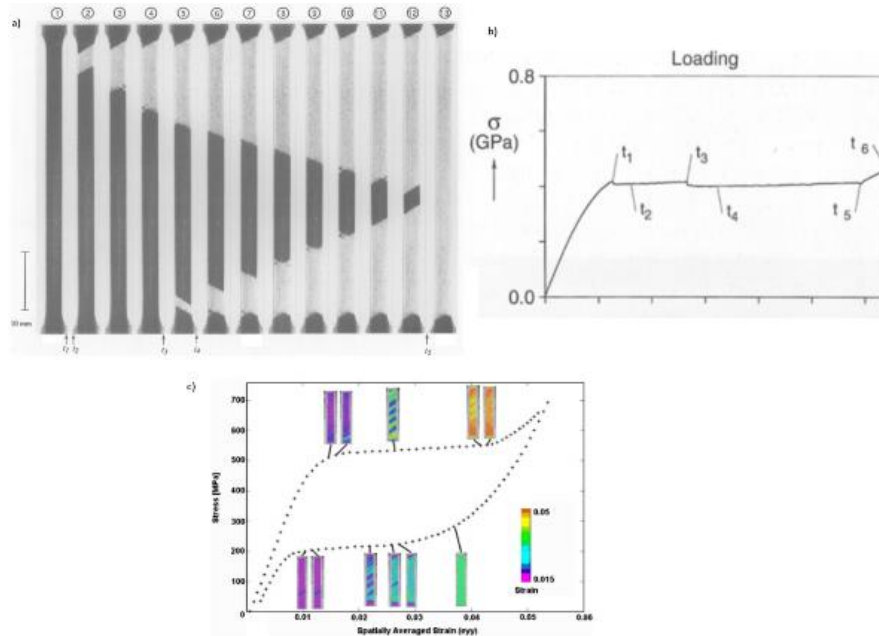


Fig. 1-1 a) Martensite band fronts (a, c) propagating during the tensile test on NiTi ribbon (b) [16]; c) The macroscopic response of a dog-bone specimen cut parallel to the RD with corresponding DIC images. The macroscopic response is the spatially averaged strain value from each DIC image plotted vs. the MTS stress value [6].

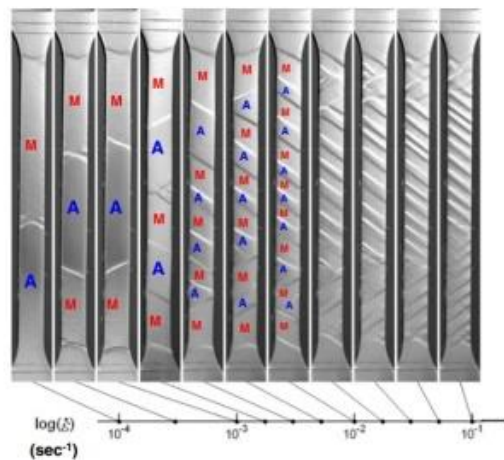


Fig. 1-2 Martensite band patterns at a fixed nominal strain of 3% under different strain rates [21]

and the deformation becomes gradually homogeneous, the number of cycles till failure increases. The fatigue failure cracks always nucleated within active zones (in cases I-IV), as it is illustrated in Fig. 1-3b, but not necessarily for the smallest strain amplitudes (V-VI) where the cyclic deformation gradually became homogeneous and the terminal fatigue crack possibly nucleated away from the active zones, preferentially in the highly deformed elastic martensite [17].

Besides, in the case of small external amplitudes and various mean strains (Fig. 4), there seems to be a difference between cases, where MBFs exist in the sample but remain immobile upon cycling (cases II and III in Fig. 4) and cases when there is no mobile MBF at all (cases I and IV in Fig. 4) [17]. But the number of cycles till failure (~ 15000 and ~ 20000 cycles, respectively) is significantly larger than ~ 200 cycles in cases when MBFs move upon cycling (Fig. 3).

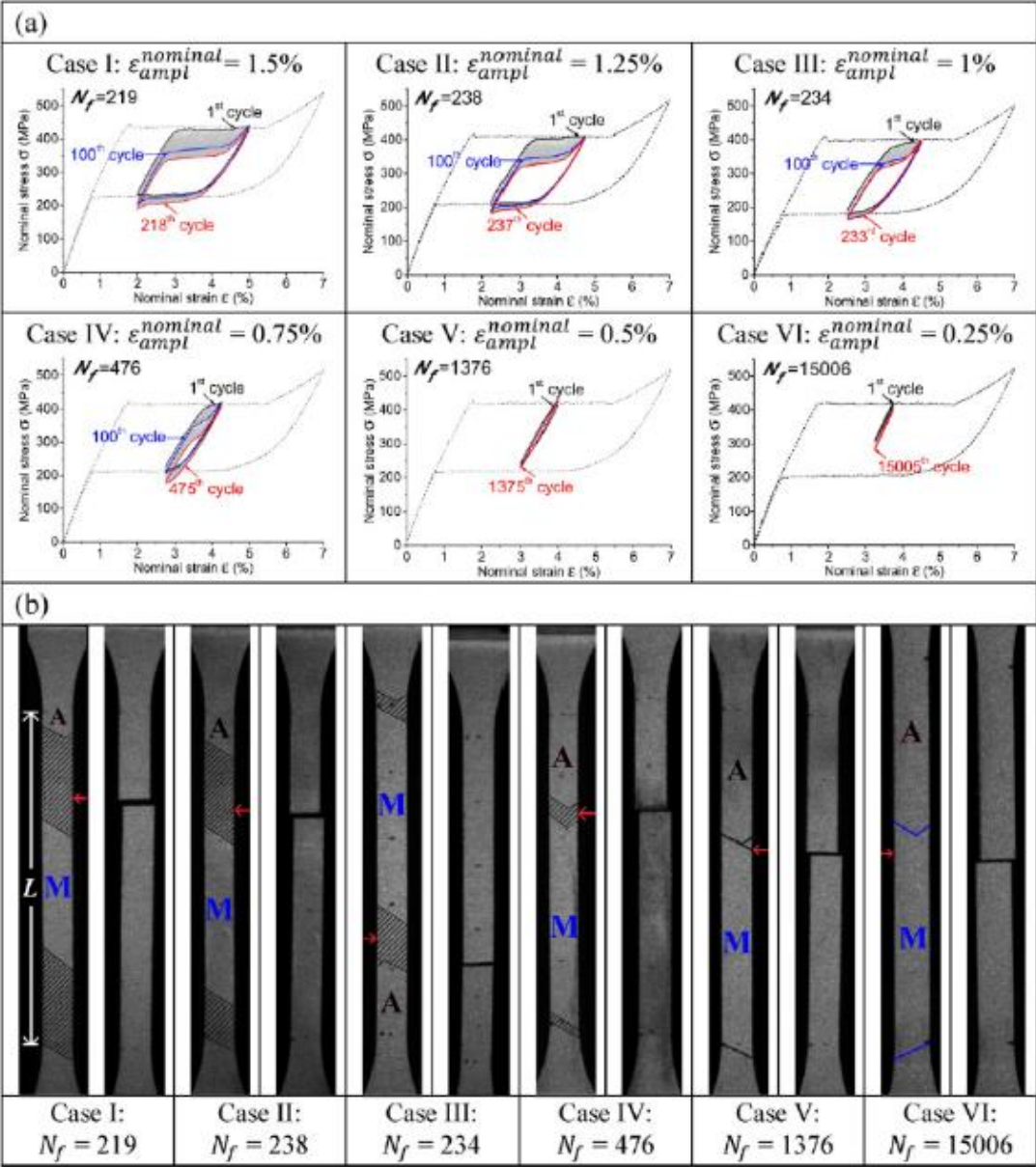


Fig. 1-3 (a) nominal cyclic stress-strain response. The dashed lines represent the iso-thermal curve, and the solid black, blue, and red lines respectively show the 1st, 100th and final cycle before the rupture. The nominal mean strain is 3.5% and the nominal strain amplitude ranges from 1.5% to 0.25%; (b) The associated Lüders-like band evolution. Active zones are indicated in the dashed area in cases I-V. Case VI without an active zone. The final fractures specimens are shown where the red arrows denote the position of the fatigue crack nucleation [17]

So far, we have discussed the localized macroscopic deformation of polycrystalline NiTi due to inherent material instability and claimed that it leads to a drastic reduction of fatigue life. However, the macroscopic strain of cycled superelastic NiTi components becomes localized also due to

geometrical reasons (stress risers). Macroscopic strain localization in cyclically deformed NiTi components is thus due to both material and geometrical instability at stress risers [6] (see Fig. 1-5).

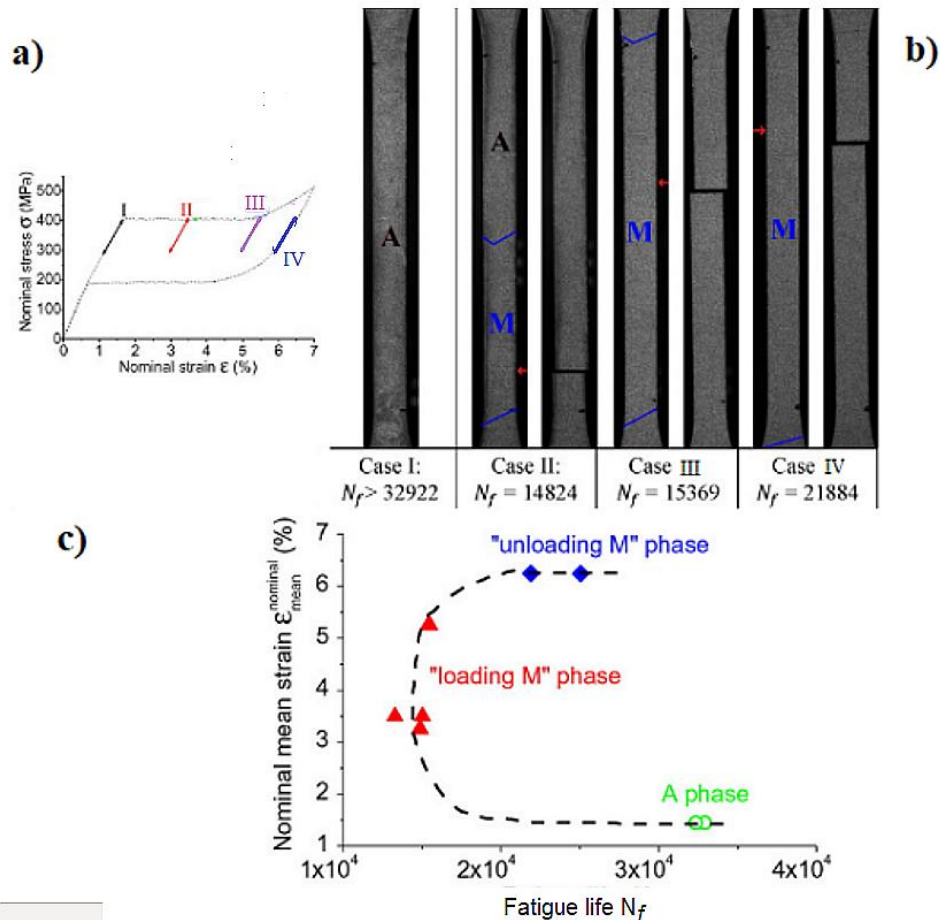


Fig. 1-4 (a) Indication of applied fatigue boundary conditions: fixed nominal strain amplitude of 0.25% (without active zones) with different nominal mean strains; b) the deformation domains and the final fractured specimens in the fatigue tests; c) The dependence of the fatigue life on nominal strain [17]

Besides MBF relates issues, premature failure originating from stress concentrations in NiTi induced by geometrical stress raisers (internal micro-notches, surface cracks, inclusions, voids, cavities, etc.) was frequently reported in the literature. In particular, brittle inclusions near the surface [22,23] are a well-known source of premature fatigue failure of NiTi. Indeed, affiliated to stress concentration effect, the martensitic phase transformation takes place preferably locally at the place of geometric stress raisers [24,25] and turns into a complex local stress and strain redistribution, which can dramatically modify the driving force parameters [26–30] and may play an important role in crack nucleation and propagation under fatigue loading conditions. Of course, the best way to improve fatigue performance is to eliminate stress risers (eliminate and/or decrease the size of inclusions). This is the goal of metallurgists producing NiTi for medical device applications. Alternatively, if we cannot get rid of the stress risers, we need to understand the mechanics of deformation under complex stress and strain field surrounding them.

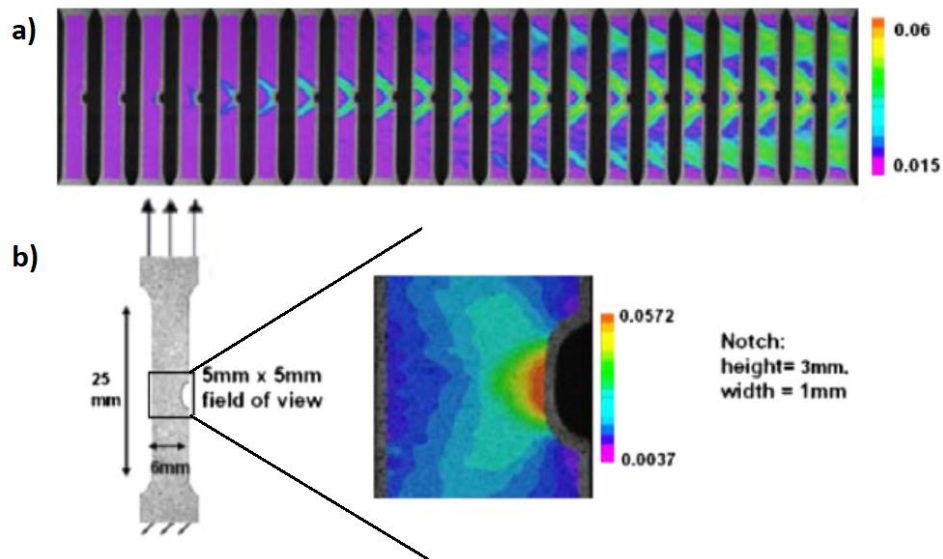


Fig. 1-5 a) full-field evolution of band localization; b) strain localization in a non-homogeneous stress field at the notch. The colormap represents the development of lobes around the notch, which initiates at the notch root and further extends towards into two symmetrically oriented bands since the strain increases [6]

Thus, beyond the necessity of experimental observations and measurements, the accurate determination of mechanical fields near notches/cracks, employing realistic stress-strain constitutive relations of SMA material, are of fundamental importance for the improvement of fatigue performance of NiTi. As the analytical models are often accompanied by mathematical difficulties and are much more complicated than the numerical ones, the combined numerical models and experimental methods can be used to investigate the cyclic evolution of martensitic transformation and plastic deformation phenomena around the cracks and notches, and their impacts on the local mechanical gradients.

Also, the cyclic behavior of SMAs could be stable, or unstable by the accumulation of irreversible strains [31,32]. The irreversible strains could be categorized into two types. The first type corresponds to the accumulation of irreversible strains during cyclic loading conditions –forward and reverse transformation between austenite and martensite– at stresses below the yield stress of the individual phases, the so-called transformation induced plasticity (TRIP). The effect of TRIP on macroscopic response can be seen as the changes in characteristics of the material, for example, the gradual changes in transformation strain, plateau stress, transformation temperatures, and the size and/or shape of the thermomechanical transformation hysteresis loop, which often could be induced by damage accumulation in the microstructural level, e.g. dislocation bands accumulation, redistribution of internal stresses –caused by gradual accumulated local plastic strains–, accumulation of internal defects, micro-cracks and voids nucleation, the evolution of remnant martensite, and the incremental increase of non-transforming austenite within the shear bands [31–36]. The second type of irreversible strain deals with the conventional plasticity induced by activation of slip systems at stresses exceeding the yield point of the α -phase¹ [37,38]. While there are many experimental shreds of evidence showing that in cyclic loading conditions, SMAs exhibit unstable response –e.g. [35,39–41] –, most of the models which are used to predict the thermomechanical cyclic response of SMAs assume the

¹ α can refer to each martensite and austenite phases.

stable material response –e.g. [42–48]–, and just a few models consider the TRIP –e.g. [36,49–53]–, and rare models have taken into account the conventional plasticity [54–57]. Therefore, the local cyclic phenomena at the stress risers in SMAparts, have never been analyzed by including the conventional plasticity.

The present thesis provides a comprehensive experimental evaluation of the local cyclic evolutions of strain fields and the martensite volume fraction around the notches in thin NiTi ribbons both in superelastic and shape memory regimes, and their correlated numerical predictions of the local and global evolutions of full-field mechanical gradients and volume fraction of martensite, and most importantly, their interaction with conventional plasticity at the root of the notches.

1.1.1. Initiation and propagation of fatigue cracks

In general, it is well-known that the fatigue resistance of metals is related to the initiation of fatigue cracks at the surface and propagation towards the bulk, particularly under cyclic tension.

In the absence of any heterogeneity, the surface cracks are initiated as a result of cyclic plastic deformation [38, 39]. Even if the nominal stresses are well below the elastic limit, persistent slip bands (PSBs) form due to dislocation dipole interaction and give rise to stress and strain concentration which results in the nucleation of cracks at the surface. According to the simple Wood’s model (Fig. 1-6) [58], upon the rising of the external load, slip arises on a favorably oriented slip-plane. Upon unloading, slip occurs in the reverse direction on a parallel slip-plane, since slip on the first plane is inhibited by strain hardening and/or by oxidation of the newly generated free surface. This first cyclic slip can form an extrusion or an intrusion in the specimen’s surface. An intrusion can turn into a crack by continuing plastic flow over the subsequent cycles (Fig. 1-6). If the fatigue loading is cyclic tension-tension this mechanism can still work since the plastic deformation occurring at the increasing load will give rise to residual compressive stresses during load release, due to the strain incompatibility between the plastically permanent deformed zone and the surrounding elastic ligament which tends to return to its original place during unloading.

In this way, the intrusion/extrusions upon continuous cyclic loading will intensify and eventually create a geometrically surface imperfection (notch effect) and a micro crack will finally initiate from the intrusion/extrusion; this simply describes the theory of how a fatigue crack will initiate in conventional metal deformed by cyclic plasticity via dislocation slip. If the compression-compression fatigue load is applied, the dislocation movement is mainly inwards (barring a few dislocations which could go in the other directions). Thus, the potential of intrusion/extrusion to form –the primary phenomenon which governs the fatigue durability– is inhibited or at least significantly delayed; such that, a longer fatigue life (higher fatigue strength) in compression cycling is seen.

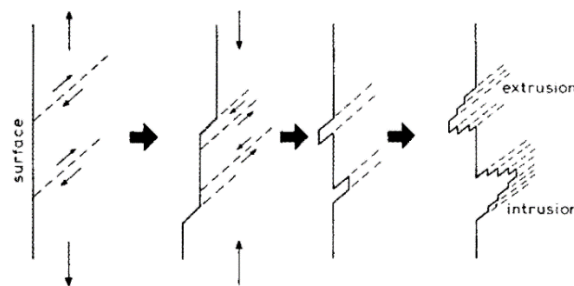


Fig. 1-6 Wood's model for fatigue crack initiation [58]

The cyclically deformed SMAs as NiTi, however, do not deform via dislocation slip but via stress-induced martensitic transformation. No one has ever seen a persistent slip band in cyclically deformed NiTi. This mechanism of homogeneous nucleation of cracks at the surface thus cannot be adopted for NiTi.

The issue also can be explained from another point of view: fatigue failure is induced by crack growth. If the stress state is ever in compression the crack is not prone to growth. In general, there is remarkably more energy needed to crush out the atoms, than that required to elongate and release them out of the bonds. Accordingly, in the present thesis, the focus is put on the cyclic loading conditions under the tensile loads, either in superelastic or shape memory regime.

1.2. Thesis outline

This Ph.D. dissertation focuses on understanding of the evolutions of the martensitic transformation and plastic deformation at the stress risers of superelastic and shape memory NiTi components subjected to monotonic and cyclic loading, and their impacts on the cyclic evolutions of the mechanical gradients around the stress risers.

Chapter 2. includes a brief introduction on the martensitic transformation which is followed by the applications of SMAs. Then, the state of the art on the functional and structural fatigue of SMAs is reviewed. At the end, the studies on the issue of the stress risers in SMAs is reviewed.

Chapter 3 is on the materials and methods.

In Chapters 4 and 5, the performed research is discussed on the phenomena in the superelastic regime in notched thin NiTi ribbons, where the material undergoes iso-thermal mechanical monotonic/cyclic loadings. In particular, in chapter 4 the role of stress raiser in conjunction with plasticity on the cyclic evolution of martensitic transformation is studied experimentally and numerically. In chapter 5 the role of both plasticity and martensitic transformation on the stress concentration factor in SMAs is studied numerically.

In Chapters 6 and 7, the phenomena in shape memory regime are analyzed in notched thin NiTi ribbons, where the material undergoes thermal cycling under an external bias force (thermal actuator SMAs). In chapter 6, the effects of the thermo-mechanical boundary conditions are studied numerically on the local cyclic evolution of martensitic transformation and mechanical gradients. In chapter 7, the role of plasticity on the local and global evolutions of the martensitic transformation, and mechanical fields are studied numerically and experimentally.

Finally, in chapter 8, the effects of the design of the self-expanding NiTi stents on their mechanical interaction with the artery and their fatigue performance are examined by numerical simulations.

CHAPTER 2. STATE OF THE ART

2.1. Martensitic phase transformation in NiTi alloys

The description of the peculiar properties of NiTi shape memory alloys can be addressed in the crystallography and thermodynamics of SMAs [59–61]. Each phase has a different crystal structure, thus, different thermo-mechanical characteristics. Parent austenite (A) is the stable phase at high temperatures which is usually a body-centered cubic crystal structure, while the martensite (M) is the stable phase at low temperatures and is tetragonal, orthorhombic, or monoclinic.

The lattice of the high-temperature austenite phase has greater crystallographic symmetry than that of the low-temperature martensite phase. The phase transformation from cubic austenite to monoclinic martensite is called the forward transformation. Every single formed martensitic crystal can have a different orientation, the so-called variant [62]. The number of variants depends on the change of symmetry during transformation. The monoclinic martensite phase in Nitinol forms in plate groups were four variants with habit plane (551) cluster about six $\langle 011 \rangle$ poles, resulting in 24 possible variants [63].

In a stress-free state, SMA materials have four characteristic transformation temperatures identified by:

- M_s and M_f , start and finish temperatures for the forward transformation (A to M)
- A_s and A_f , start and finish temperatures for reverse transformation (M to A)

In the following, the thermodynamics of phase transformation is briefly explained attributed to shape memory effect and superelasticity:

1.1.2. Shape memory effect

At a stress-free state, when the material is in the austenite phase at high temperatures, upon cooling the austenite transforms to martensite. There is no reason why the entire crystal should transform from the austenite to a single variant of martensite. Indeed, it does so in a very special manner, the different regions of the crystal transform to different variants of martensite (see path 1-2 in Fig. 2-1a, Fig. 2-2a, and Fig. 2-2b) in such a manner that there is no commitment of macroscopic change in the shape of the crystal (no macroscopic strain induces upon the path 1-2, see Fig. 2-2a). In other words, when austenite transforms to martensite under no stress, multiple martensite variants and twins –crystallographically equivalent but with different orientations differing only by habit plane– form with enough orientations which interdict net distortion (see path 1-2 in Fig. 2-2b). This transformation of the austenite to a microstructure of martensite with no net change in shape is known as self-accommodation [60,64].

Now, when the crystal is exposed to the external load (path 2-4 in Fig. 2-1a and the associated path 2-3-4 in Fig. 2-2a-b), it can accommodate the deformation by either distortion of the crystal lattice, or by a simple rearrangement of the variants to form a new microstructure. The former costs energy; thus, the latter is preferred, and dissimilar variants begin to convert to a single variant determined by alignment of the habit planes with the direction of loading (the pairs of martensite twins begin

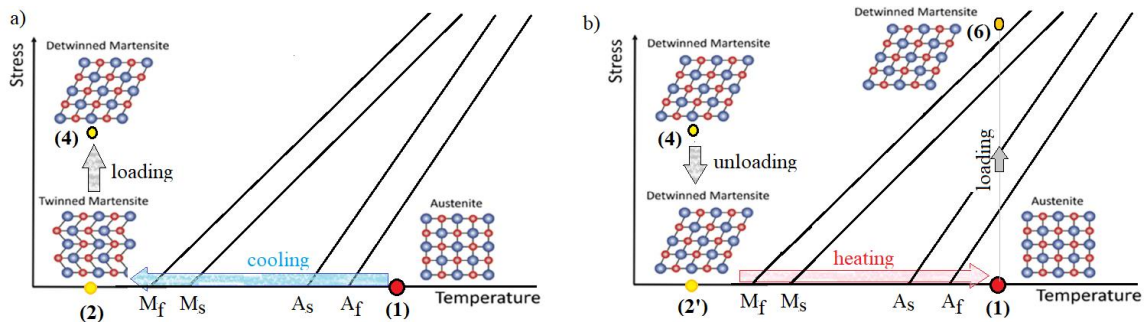


Fig. 2-1 Schematic representation of Shape Memory Effect in path 1-2-4-2'-1, and superelasticity in path 1-6-1, within the critical stress-temperature space

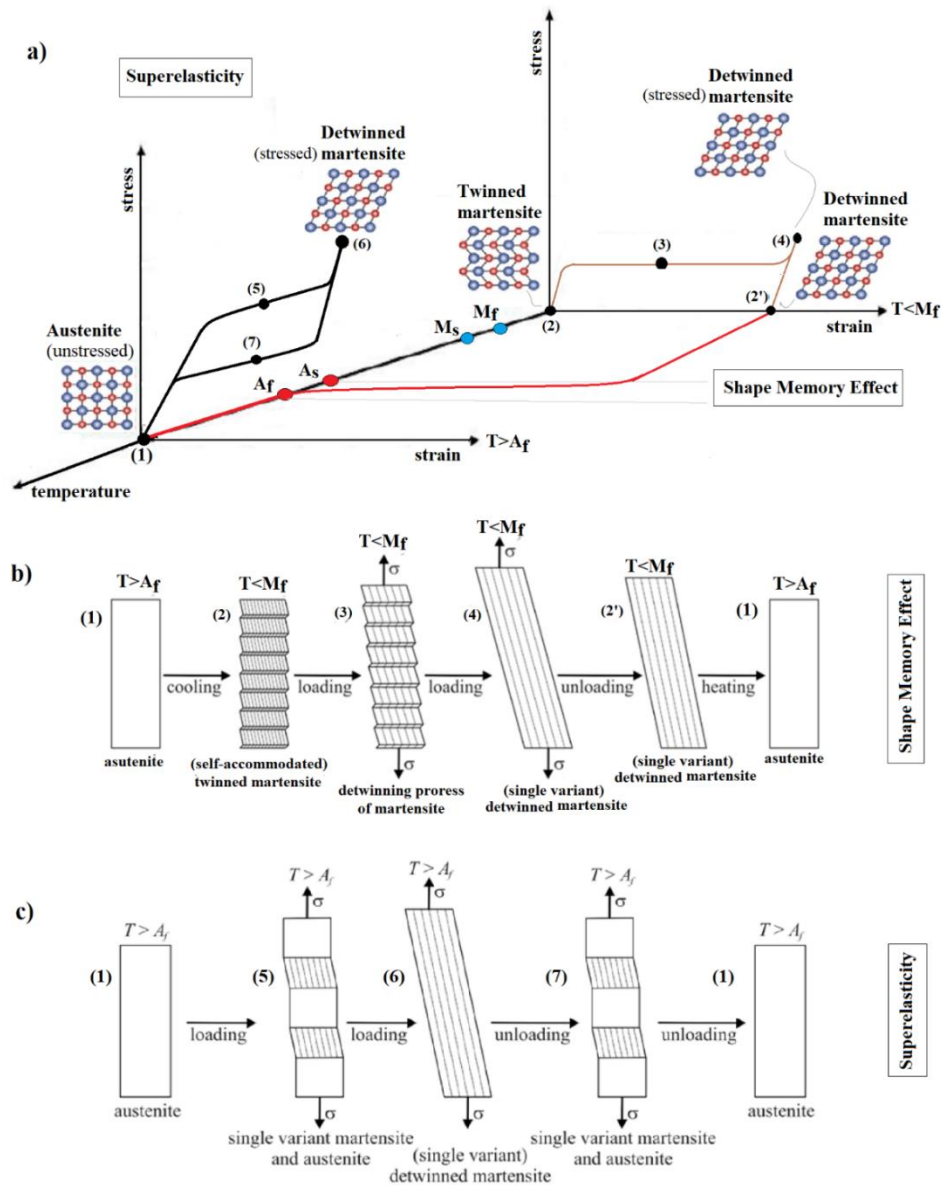


Fig. 2-2 [64] a) schematic representation of Shape Memory Effect in path 1-2-3-4-2'-1, and superelasticity in path 1-5-6-7-1, within the critical stress-strain-temperature space; b) shape memory effect, the evolution of variants upon path 1-2-3-4-2'-1; c) superelasticity, the evolution of variants upon path 1-5-6-7-1

detwinning to the stress-preferred twins, see path 2-3-4 in Fig. 2-2b), thus have equivalent energy. In consequence, changing microstructure induces a crystal change - *and inelastic strains*- without alternating its energy. Upon unloading (path 4-2' in Fig. 2-1b), since the deformed martensite and the self-accommodated martensite have identical energy, there is no objective that the crystal to again convert to multiple variants (see path 4-2' in Fig. 2-2b); therefore, only a small elastic strain is recovered, leaving a large residual strain (see path 4-2' Fig. 2-2a-b).

The retained inelastic strains are then recovered by heating (path 2'-1 Fig. 2-1b and Fig. 2-2b) and the martensite variants transform back to the single variant austenite phase. Hence, disregarding the microstructure and configuration of the crystal at low temperature, it must return to its original shape in austenite. Consequently, the shape memory property is affiliated to the energy states and the ability of the material to change the microstructure freely and there is a clear link between the macroscopic behavior with the crystallography and microstructure.

1.1.1. Superelasticity

If the SMA material is in the austenite phase (parent phase at $T > A_f$), when stress is applied (see path 1-6 in Fig. 2-1b, and the corresponding path 1-5-6 in Fig. 2-2a & Fig. 2-2c) specific variants of martensite will be formed preferentially. When the transformation is finished, the material will be in stress-induced martensite consisting of a single variant of detwinned (stress-induced) martensite. Upon unloading –since the martensite is not the stable phase in unstressed state at $T > A_f$ – a reverse phase transformation takes place. The corresponding recovery of high inelastic strains during unloading yields an identifying hysteresis (loop 1-5-6-7-1 Fig. 2-2a), known as superelasticity (pseudoelasticity).

2.1. Nonequilibrium Stress-Temperature Phase Diagram of Shape Memory Alloys

The thermodynamic stability of austenite and martensite phases depends on the external stress and temperature. A nonequilibrium phase diagram for shape memory alloys shows regions of the stability of austenite and martensite phases in stress-temperature space mutually separated by 4 transformation lines (Fig. 2-3a). The slope of transformation lines is given by the Clausius-Clapeyron equation and the mutual separation of transformation lines depends on the hysteresis associated with the phase transformation. M_f , M_s , A_s , and A_f are the transformation temperatures determined in free-stress conditions. Under the applied stresses, the transformation temperatures increase linearly with increasing stress; i.e. under the applied external stress σ_a , transformation temperatures M_s^a , M_f^a , A_s^a and A_f^a can be determined [42,65,66]. In Fig. 2-3, **A**, **M^d** and **M^t**, represent the austenite, detwinned martensite, and twinned martensite, respectively. The red strip in Fig. 2-3a corresponds to the transformation from **M^d** to **A**, either during unloading ($b \rightarrow a$) or heating ($a' \rightarrow b'$), and the blue stripe represents transformation between **A** to **M^d**, either due to loading ($a \rightarrow b$) or cooling ($b' \rightarrow a'$). Below the M_f temperature in stress-free conditions, the material is in twinned martensite and by an iso-thermal applied mechanical loading, the martensite detwinning would proceed ($a'' \rightarrow b''$). Cooling the austenite under low applied mechanical stresses ($\sigma < \sigma^s$) results in transformation from **A** to **M^t**. Strain-temperature and stress-strain curves corresponding to the paths a-b, a'-b' and a''-b'' are shown in Fig. 2-3b to Fig. 2-3d.

It does worth noting that these transformation boundaries shown in Fig. 2-3a, are not necessarily linear and are only represented as such for this schematic illustration. A more descriptive presentation

of these transformation regions and their optional representations can be found in the literature [42,67]. Also, polycrystalline SMA materials often show significantly different transformation behavior in compression as opposed to tension. This tension/compression asymmetry is not accounted for in this description, but a complete discussion can be found in [68]. Additionally, the R-phase transformation paths are not shown in Fig. 2-3a [69–71].

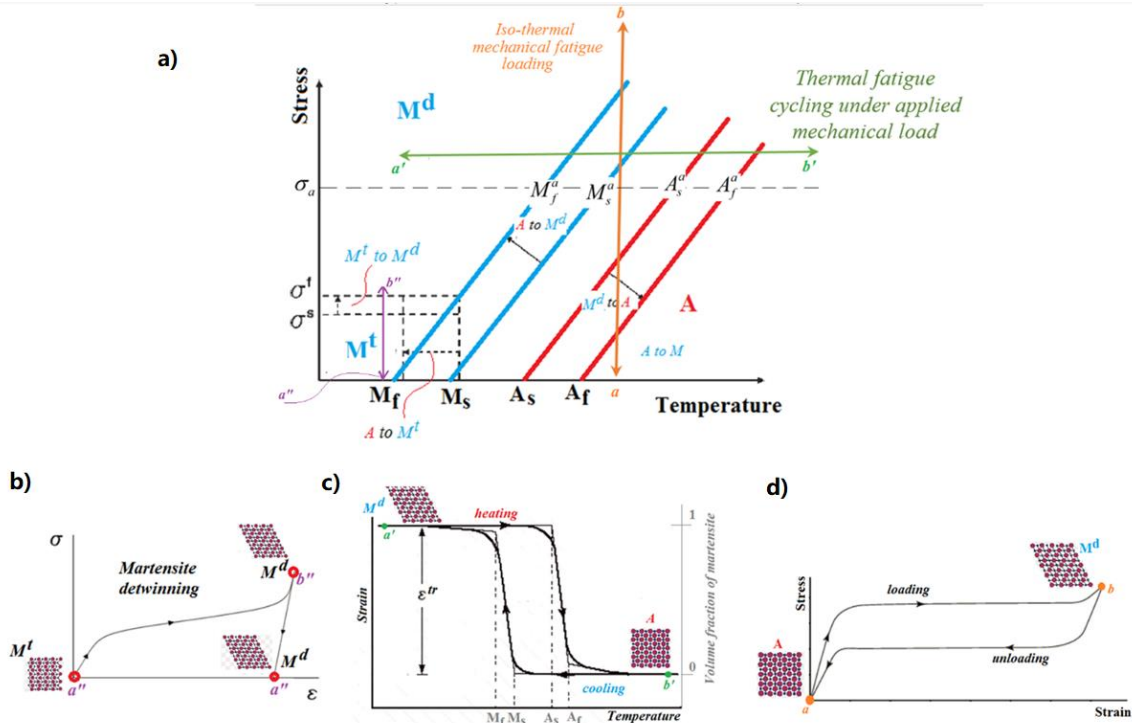


Fig. 2-3 a) Schematic phase diagram of shape memory alloys, b) M^t detwinning to M^d in loading path a'' - b'' , c) $M^d \leftrightarrow A$ transformation under stress upon loading path $a' \leftrightarrow b'$, d) $M^d \leftrightarrow A$ transformation upon loading path $a \leftrightarrow b$

2.2. Applications of NiTi alloys

1.1.2. Superelastic NiTi (SE)

- *Self-Expanding Stent*

One of the targets in modern surgery is to use less invasive techniques using small, leak-tight tools into the body called trocars. Unique properties of SMAs are utilized in a wide range of medical applications. The self-expanding NiTi stents are cylindrical mesh thin-walled devices produced either from wires, laser cut tubing, and laser welded or coiled striped etched sheets [64]. The superelastic NiTi stents are first crimped and pushed into the catheter when the catheter is in the correct site of the defect in the artery, the SE stent is released, and then it expands in opposition to the inner wall of the artery due to either a rise in temperature (induced by the recovery of the original configuration by heating to the above of its A_f , into the body) if shape memory effect is in use or just due to the releasing the load if superelasticity property is in use. This resolves the local artery's occlusion and re-opens the vessel to reach its normal flow of blood (see Fig. 2-4a). Then the delivery catheter is removed, leaving the stent in the patient's vessel. The most targeted sites reported are cardiovascular, superficial femoral, and popliteal arteries. Just in one case of them, there are over ~8 million US and ~200 million global patients suffering from peripheral artery disease, due to recent studies by Fowkes et al. [72]

and Rogers et al.[73]. It is shown that implantation of a self-expanding stent gives better outcomes than the classic balloon angioplasty [74,75].

Different sites within the stent's structure are loaded to different stress levels during the crimping (into the catheter) stage of the deployment process and when it is released from the catheter, undergo fatigue loading induced by heart pulsation. Thus, in a unique structure, there are a variety of fatigue loading amplitudes (see red arrows in Fig. 2-5) conditions at different locations of a deployed stent. This will be further discussed in CHAPTER 8.

Esophageal stents are commonly used for a variety of purposes. The most usual indication of esophageal stents is for the treatment of malignant dysphagia, benign esophageal strictures, fistulas, and leaks (see Fig. 2-4b).

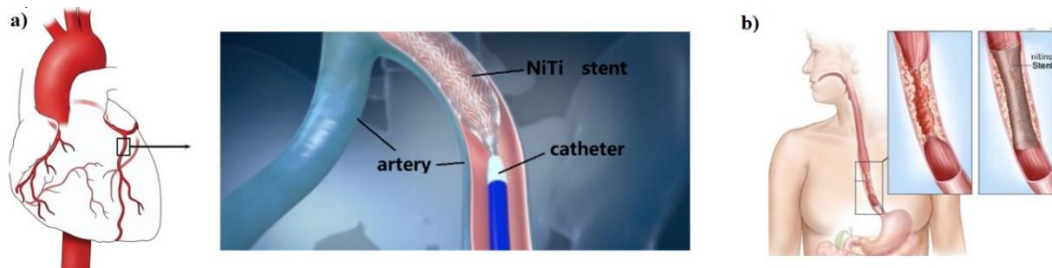


Fig. 2-4 a) cardiovascular application of NiTi self-expanding stents; b) Esophageal stents

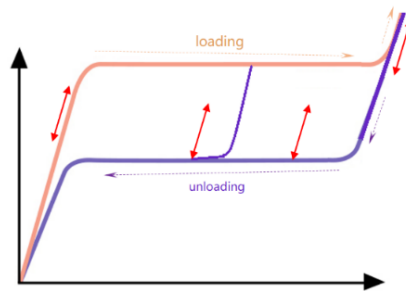


Fig. 2-5 stress-strain response of the material depending on the position and the local response

- ***Bypass heart surgery***

nitinol 'open heart stabilizers' are used in open-heart bypass surgeries to prevent regional heart movements upon operating (Fig. 2-6).

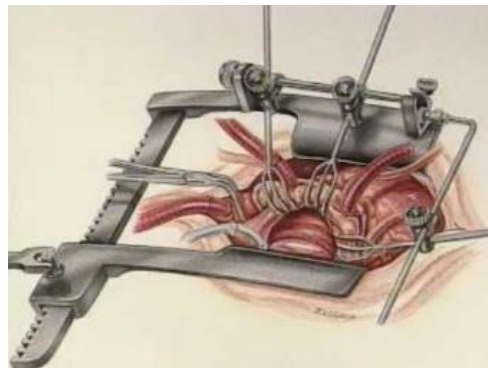


Fig. 2-6 nitinol open heart stabilizers

- *orthopedic implants*

since nitinol has similar stress-strain properties to the bone, it is a perfect alloy to produce bone fixation devices and other trauma implants. SMAs have beneficial characteristics concerning the conventional bone fixation plates since they can apply a constant force that turns into a faster bone fracture healing [76]. One example is the widely used *SE memory staples* which is an effective alternative for fixation to screw or classic plate fixation. Delivered at ambient temperatures, the Nitinol *staples* structure induces balanced pushing forces. They are pre-loaded with a particular pincer (Fig. 2-8); the legs are then inserted into the guided pilot holes (Fig. 2-7). Since the force is released, the memory of the alloy exerts an immediate and continuous compressive force on the legs. The compression maintains throughout treatment [77].



Fig. 2-7 Nitinol superelastic orthopedic staples [77]



Fig. 2-8 Particular pincer to preload the Nitinol superelastic orthopedic staples upon implementation [77]

- *Seismic applications*

Several active, passive, and hybrid energy absorption and vibration isolation devices have been developed utilizing NiTi SMAs. The passive control method utilizes the pseudoelastic behavior of NiTi. Outstanding characteristics of superelastic SMAs such as high damping capacity, ability to recover large strains without any residual deformation even after strong ground excitations, resistance to fatigue when undergoing small strain amplitudes upon earthquake, besides their corrosion and durability make them an effective candidate in designing the damping devices and base isolators as passive control systems and seismic isolation. The results from the global reports show the effectiveness of their application to control and enhance the response of structures when prone to the quake [78–80].

2.2.1. Shape Memory NiTi

▪ *orthopedic implants*

There are a variety of orthopedic implants utilizing the shape memory effect of the nitinol [64,81]. An example is the *compression shape memory staples*, also used for internal bone fixation. Their action is very similar to the *SE memory staples* explained above. The difference is that when inserting into the tissue the material is in martensite state. Then, a predefined electric current is passed through the fixator heating it to the above A_f to recover its designed closed shape and fix the fractured site in compression [82] (Fig. 2-9).

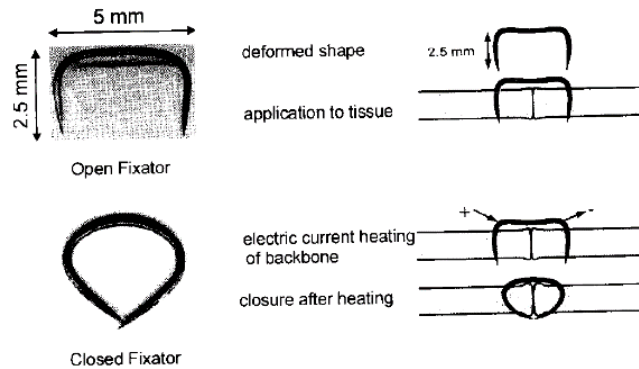


Fig. 2-9 the compression shape memory staple, a) open shape in the martensitic state, b) closed configuration in austenite (by passing an electric current) after inserting into the targeted tissue joint [82]

▪ *Thermal actuators*

Shape memory alloys are widely used as thermal actuators, in several fields such as robotics [83], biomimetics [84,85], heat engines [86–88], and sun-tracking system for solar panel system [89,90]. Actuators based on SMA show a higher power-to-weight ratio compared to other actuating technologies [91] (Fig. 2-10). Moreover, their operation is achieved with no need for the frictional and vibrating parts, making the SMA actuators to be designed in a compact volume/size and significantly more silent. An additional advantage of the SMA making them a valid alternative for to the conventional actuators is that they can work in a liquid environment with no loss of their functionality and mechanical properties.

The SMA elements used in the thermal actuator can be in different configurations based on the application's requirements [92]:

- Straight wire/ribbon in tensile mode → large linear motion/high force
- Torsion bar/tube → large rotation, small torque
- Cantilever strip → large displacement, the small force
- Belleville-type discs → small linear motion, high force
- Helical spring → large linear motions/rotation, small force/torque

For the realization of cyclic movements in an SMTA mechanism, external forces should be applied to the SMA element either by a constant force from a dead load or variable forces supplied by bias elastic springs [69,93–99]. The shape memory element is pre-loaded either in martensite or austenite states (based on the design requirements), then is exposed to the heating-cooling cycles, thus frequent

phase transformation between austenite and detwinned martensite (Fig. 2-11b), during its function. The forward and reverse phase transformations between the two phases induce a thermal hysteresis (Fig. 2-11a). Among a variety of available SMA alloys, NiTi alloys remain to be a preferred choice for SMA applications [92,100] thanks to their good workability, structural properties, and excellent stability of functional properties [101,102]. Despite their excellent properties in comparison to other SMAs, however, the poor fatigue behavior of NiTi alloys compared to conventional materials hinders their wider use [103].

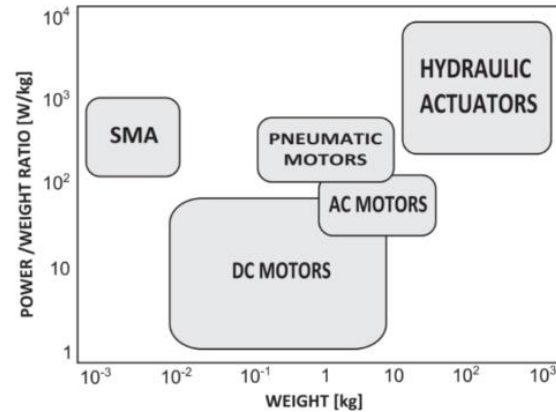


Fig. 2-10 Diagram showing the power/weight ratio versus the weight of different actuation technologies. Low-weight SMAs show better performances concerning traditional actuators [91].

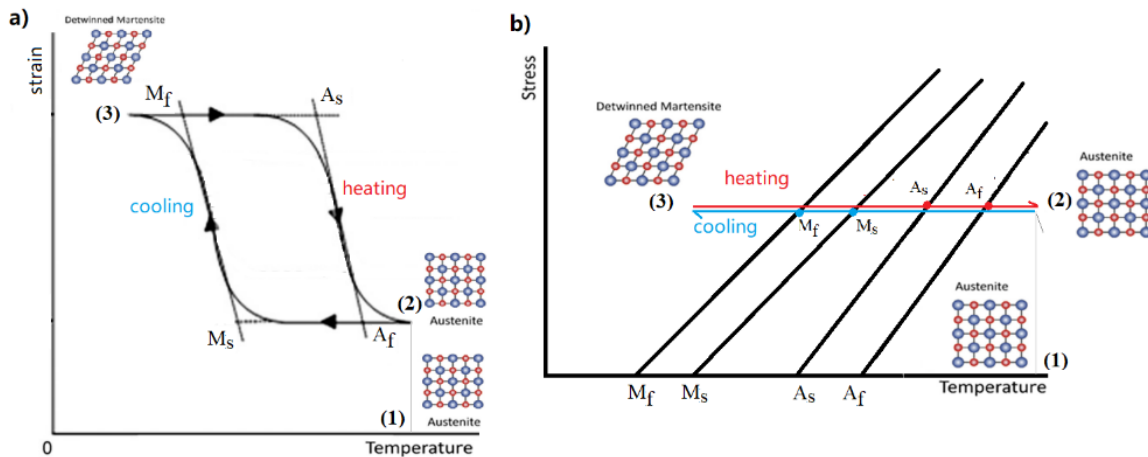


Fig. 2-11 Schematic of the: a) strain-temperature response, and b) stress-strain loading path of an SMA actuator element; preload is applied in austenite phase (or martensite), then the material undergoes heating-cooling thermal cycles under constant stress

2.3. Fatigue of NiTi alloys

Fatigue in SMAs can be classified as [104]: functional fatigue and structural fatigue. Functional fatigue addresses the degradation of the functional properties of the material over the repeated either mechanical or thermomechanical cycles. Examples are shrinking the transformation hysteresis loop, accumulation of unrecovered strains, and shift of the transformation temperatures. Structural fatigue is associated with the fatigue crack initiation and propagation which results in the rupture of the specimen over the cyclic loadings. Both issues have been attractive in the field mimicking the safety and functionality of the engineering design of SMA systems. The majority of the studies in the literature on the fatigue of SMAs have used the stress-controlled tests and stress-life representation

of fatigue, however, there are a variety of studies in which the strain-controlled test method is used. Superelastic SMAs have been used either in the systems where the SMA element is supposed to undergo force –such as reinforcing bars in concrete bridges and endodontic files– and where they are expected to undergo cyclic deformation controlled by a strain range –such as arterial self-expanding stents–. The following sections will briefly review the state of the art on the structural and functional fatigue of nitinol, respectively.

1.1.3. Structural Fatigue

Generally, the cyclic martensitic transformation can occur either by pure ‘mechanical cyclic loading’, i.e. applied stress/strain in a constant temperature in superelastic regime (path a-b in Fig. 2-3a); or ‘thermomechanical cyclic loading’, by heating/cooling under applied mechanical load in shape memory regime (path b’-a’ in Fig. 2-3a).

- *Bending & rotation-bending*

At the early stage of applications of SMAs, and more specifically nitinol, they were mainly being used in the form of wires. Thus, the first studies on the fatigue of SMAs were focused on bending and/or rotation-bending of nitinol wires [105–110]. Additionally, the development of applications of SMAs in orthodontic archwires has pioneered the motivation of the rotary bending tests [111].

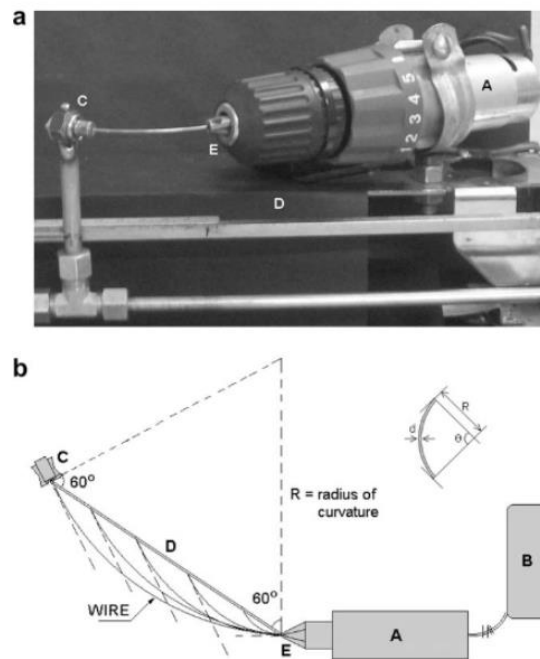


Fig. 2-12 In The test branch used by Figueredo et al. [109] in rotary bending fatigue tests, one side of the wire (E) is rotated with a motor (A). The opposite end of the specimen could rotate freely inside a hole drilled in a steel cylinder mounted in a small ball bearing (C)

Figueredo et al. [109] analyzed the low-cycle fatigue of superelastic NiTi SMA wires, by the strain-controlled rotating-bending tests with the applied strain amplitudes from 0.6% to 12% (Fig. 2-12). They found a ‘‘Z-shaped’’ $\epsilon_a - N_f$ curve, which demonstrated an increased fatigue life with the

increase in the applied strain amplitude within a specific range. In other words, it shows that in a range of 1-10% strain amplitude, the bigger the applied strain the longer the lifetime (Fig. 2-13).

Tobushi et al. [105] studied the low-cycle rotating-bending fatigue of the NiTi SMA wires in air, water, and silicone. They observed that the type of temperature controlling media has a minor effect, while the test temperature significantly influences the fatigue life in tests performed in water in the low cycle fatigue regime (Fig. 2-14).

Sawaguchi et al. [8] performed the rotating-bending fatigue experiments on nitinol wires (Fig. 2-15a). They showed that the effective parameter in the fatigue life is the maximum tensile and compressive strain amplitudes ϵ_a in the surface of nitinol wires (Fig. 2-15b-e). Accordingly, they showed that the low-cycle fatigue rupture occurs at strain amplitudes beyond 1% while reducing the amplitude below 1% significantly increases the number of cycles to failure. Further, their results showed that at strain amplitudes less than 0.75% the fatigue induced rupture does not happen up to 10^6 cycles.

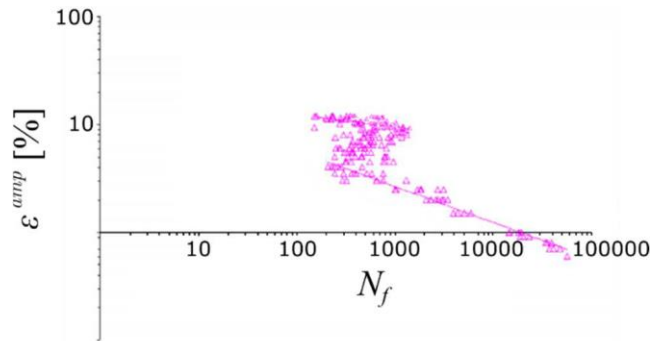


Fig. 2-13 Z-shaped Strain-N curve obtained upon rotary bending fatigue of NiTi wires, redrawn from [109]

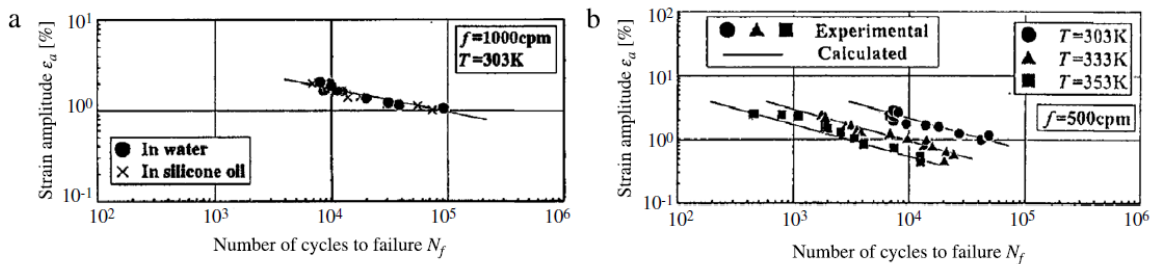


Fig. 2-14 Strain amplitude vs. fatigue life: (a) in water and silicone oil; (b) at various test temperatures in water [105]

Wagner et al. [107], investigated the effect of wire diameter and rotational speed (frequency) on fatigue rupture behavior in their bending rotation fatigue experiments and outlined that the dependence of fatigue life on wire diameter and rotational speed is no longer observed when the bending rotation fatigue experiments are conducted in a silicone oil bath at a constant temperature or low rotational speeds in air. The reason could be the fact that the main roles of the loading frequency and the wire's diameter are the heat generation effect and the ability to exchange the generated heat to the environment, respectively. Nevertheless, when there is an infinite temperature control media which supplies the iso-thermal conditions during the test, these effects would miss their importance. It is more sensible when referring to the work done by Sawaguchi et al. [8], where they found out that the wire's diameter and the loading frequency have significant effects on the number of cycles to

failure, especially in the low-cycle fatigue regime in air. This is due to a temperature increase in the wires that occurs as a consequence of the movement of martensite/austenite interfaces during the stress-induced formation of martensite.

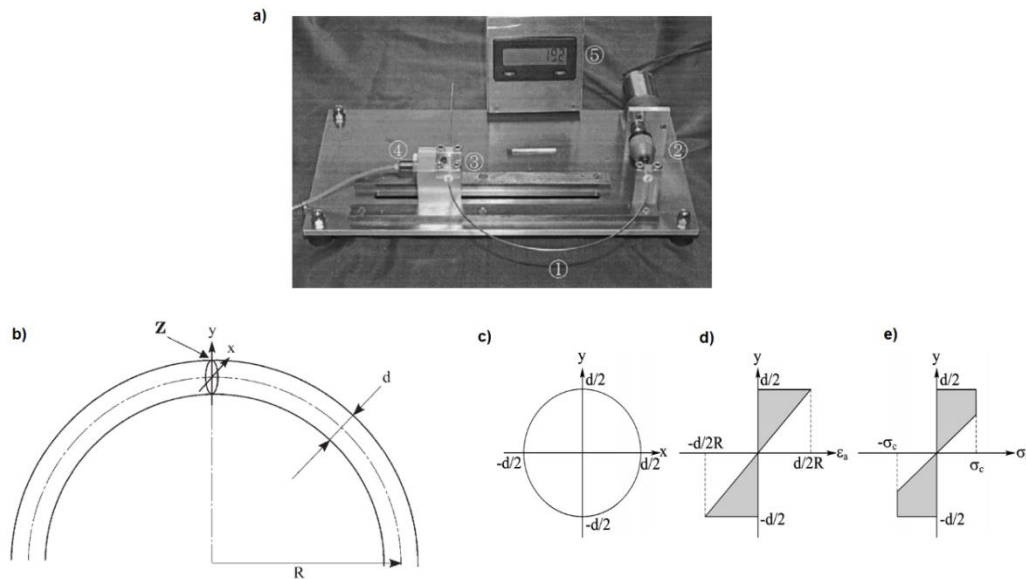


Fig. 2-15 a) bending rotation fatigue test rig used by Sawaguchi et al. [8]: 1-SMA wire subjected to fatigue loading by bending-rotation, 2-loading rotation grip connected to the motor, 3-bearing, and 4 and 5-measurement and display of fatigue cycles, b) Schematic drawing of a wire (diameter d) bent into a semicircular shape (radius of curvature R) and an x - y coordinate system attached to the central cross-section, c) cross-section of the wire, d) strain distribution across the wire, e) stress distribution across the wire. Redrawn from [8]

▪ *pure shear and uniaxial tests*

Even though Duerig et al. [112] in 1999 showed that the data acquired from the rotation-bending experiments can be equivalently utilized to predict the fatigue life under other types of loading conditions, however, the researchers have extended the experimental investigations into pure shear and uniaxial tests on the solid-bar, wires and tubes with large cross-sections as required (to prevent the buckling) [23,27,41,113–117].

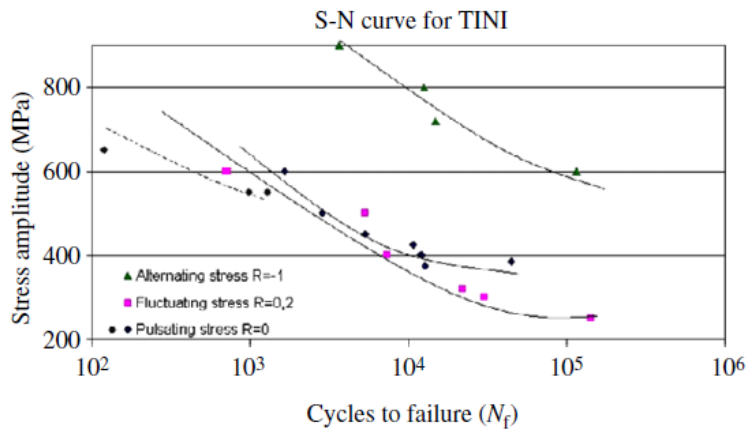


Fig. 2-16 Stress amplitude vs. fatigue life [115]

Melton and Mercier's [27] conducted force-controlled tests in a fully reversed condition ($R = -1$). They observed that fatigue behavior has a strong dependence on the metallurgical phases of the material. Superelastic nitinol exhibited higher fatigue resistance compared to the mixed-mode and martensitic nitinol. Further, in the superelastic regime, fatigue life increases by increasing the test temperature.

Moumni et al. [41,115] examined the effects of stress amplitude and mean stress on the fatigue life (Fig. 2-16) and indicated that compressive mean stress has a beneficial effect on the fatigue behavior of the alloy because it tends to close the probable micro-cracks or other types of microstructural defects, while tensile mean stress turns in an opposite effect.

Tyc et al. [118], performed tensile fatigue tests on nitinol superelastic thin wires and studied the effect of cold work/heat treatment on fatigue performance. The strain-controlled tests were done beyond the end of the superelastic plateau at a constant temperature. They found that heat treatment plays a significant role in the fatigue life of the nitinol wires since different heat treatments make difference in the magnitude of the material's maximum transformation strain; i.e. the larger the transformation strain the lower the fatigue life. Minor enhancement of fatigue behavior was also observed using a proper degree of cold work and heat treatment and the degree of impurities in works by Rahim et al. [119], Pelton et al. [120], Schaffer and Plumley [121], and Schaffer [122].

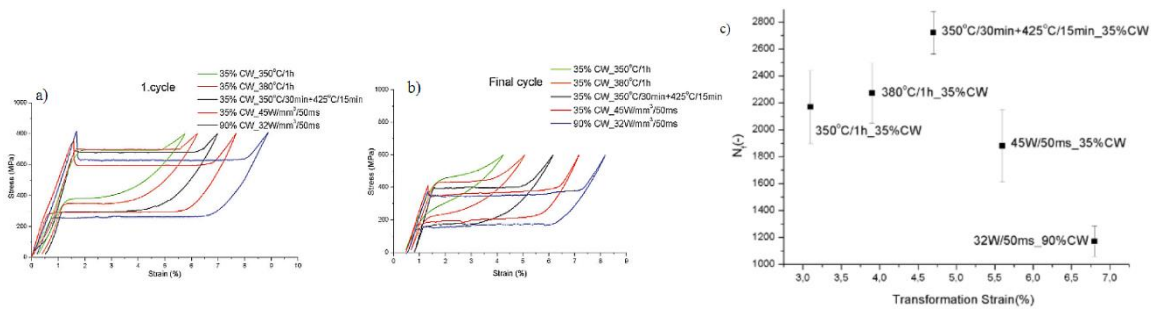


Fig. 2-17 Comparison of the superelastic response of the tested wires subjected to different types of annealing a) 1st cycle after annealing, b) the last (slow) cycle before failure, c) dependence of the number of cycles to failure on transformation strain, redrawn from [118]

In SMAs the strain-controlled fatigue tests are more deterministic since in a very narrow stress range the material undergoes large strain hysteresis and the stress-controlled experiments cannot capture the precise role of the martensitic transformation (such that the cyclically evolved volume fraction of martensite) in the fatigue performance, even though volume fraction of the stress-induced martensite was found to be a key parameter affecting the fatigue behavior of the superelastic Nitinol. It is known that for the conventional metallic alloys a positive tensile mean stress/strain can dramatically tend to drop in fatigue life, while it was reported that tensile mean strain does not necessarily decrease the fatigue life of nitinol alloys and for a range of tensile mean strains, the fatigue life of the nitinol alloys increases by increasing tensile mean strain [123][124]. Morgan et al. [124] reported longer fatigue life for nitinol specimens with a 6% mean strain compared to those with 4% and 2% mean strain, undergoing the same strain amplitudes. This behavior is not typical for conventional metallic alloys (Fig. 2-18).

Mahtabi et al. [125] studied the effect of mean strain on the fatigue behavior of round dog-bone superelastic NiTi specimens at room temperature under uniaxial loading conditions. Their results showed that the mean strain has a significant effect on the fatigue of nitinol. Especially, the data from fully reversed loading indicates the significant decrease in fatigue life when the strain amplitude exceeds 1% where the transformation strains evolve, and the partial stress-induced martensitic transformation participates in the material's deformation mechanism. Similar results can be found in [126,127]. Their results also indicated a linear relationship between the strain amplitude and the fatigue life for in all R_ϵ values (Fig. 2-19).

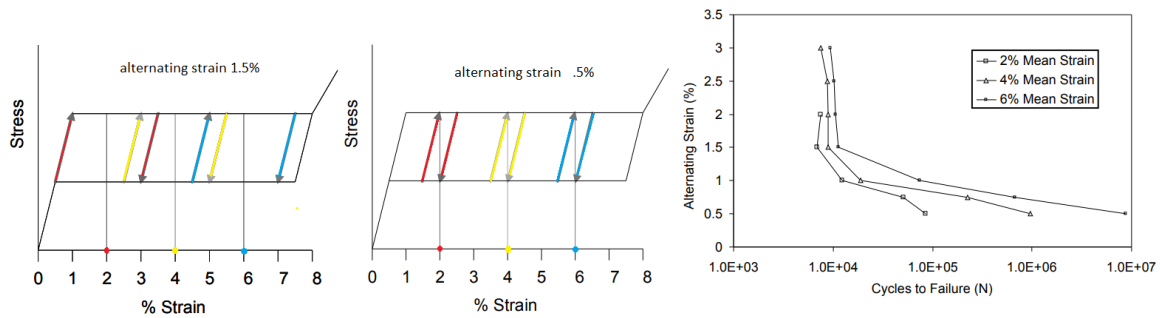


Fig. 2-18 Idealized diagrams of the stress/strain hysteresis profiles of the samples cycled at an alternating strain of a) 1.5% and b) the samples cycled at 0.5% mean strain; c) Cycles to failure of NiTi samples (38°C) [124]

In section 1.1. the work done by Zheng et al. [17] was presented, where they fundamentally address the role of the mean strain and strain amplitude on the mobile band fronts (MBFs), which in turn reveal their effects on the low-cycle fatigue of NiTi.

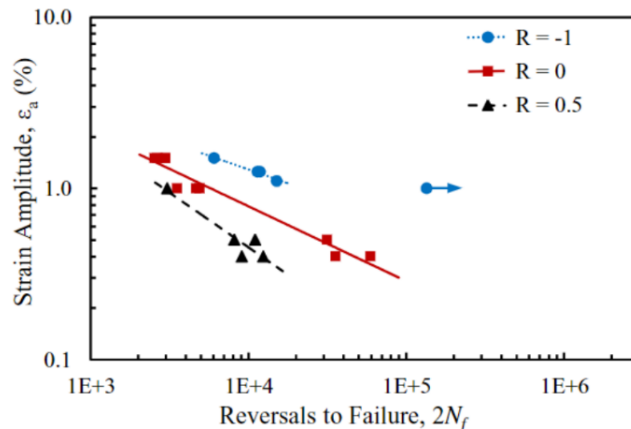


Fig. 2-19 Strain-life fatigue data for several R_ϵ values [125]

- **Micro-tubes**

In the case of nitinol stents, the design based on predictions obtained from the large specimens (wires, plates, tubes, and solid cylindrical elements) is tricky. In fact, since the size of the micro-tubes used in stent production (wall thickness around a few hundreds of microns) is physically less than an apparent macro-crack, the familiar crack propagation does not take place in fatigue failure of nitinol stents and the fatigue is phenomenologically different from those large components. Consequently, to avoid a non-conservative fatigue life prediction of stents it is necessary to directly perform fatigue tests on stents, or if not possible on micro-tubes used in their production, as it was done by Song et

al. [108,128–130], Wang et al. [131] and Matsui et al. [108]. Song et al. [128] studied the uniaxial fatigue failure features of superelastic NiTi SMA micro-tubes by doing a set of stress-controlled tensile/compressive fatigue experiments at 37°C. They concluded that the degree of martensite transformation that occurred during the cyclic deformation greatly influences the uniaxial fatigue failure of super-elastic NiTi SMA micro-tubes, and the fatigue life with more complete martensite transformation is shorter than that with incomplete one. Matsui et al. [108], performed tensile and rotation-bending experiments on superelastic nitinol thin wires and nitinol thin tubes. They observed the steep slope in the low cycle region of the strain-life fatigue curves of both nitinol tube and wires and a strain limit for infinite life between 0.6% and 0.8%. As well, they observed that in the tube, fatigue cracking initiates on the rougher inner surface, resulting in a shorter fatigue life than in the case of the wire.

1.1.4. Functional fatigue: Unrecovered Strains

In theory, the stress-strain-temperature responses of NiTi elements shall be fully reversible for millions of cycles if loaded within the material's specific limits, since they are evolved by the reversible deformation processes induced by martensitic phase transformation. These limits, for instance, for superelastic NiTi wires are rough: stresses below 1GPa strains less than 7% and temperature <100°C – depend on alloy's composition and the specimen's (preparation) history [61]–. In reality, however, upon cyclic loading lattice defects are introduced, microstructure evolves irreversibility and unrecovered strains are induced; which results in the gradual degradation of the functional properties over repeated cycles and the number of cycles till failure reduces to only a few thousand [40,132]. In general, the functional fatigue in the superelastic loading regime may refer to shrinkage of the mechanical hysteresis (reduction of the dissipated energy per cycle), change of the critical transformation plateau stresses, and accumulation of irreversible strains.

The incremental plastic deformation, occurring upon mechanical or thermomechanical cycling in NiTi wires which is conventionally known as unrecovered strain –transformation induced plasticity TRIP-, can be due to [33,132]: *i*) the residual martensite remaining at low temperature due to the stress hysteresis (strains can be fully recovered by overheating above A_f), *ii*) plastic deformation in austenite and/or martensite phase accompanying the martensitic transformation at ambient temperatures (strains cannot be recovered by further overheating far above A_f), *iii*) residual martensite locked within the deformed microstructure at ambient temperatures (strains can be partially recovered by further overheating far above A_f but not completely since they partially reappear upon cooling [133]), and *iv*) conventional plasticity via dislocation slip in austenite at high temperatures (strains cannot be recovered by overheating). A variety of studies have investigated the degradation of the functional properties and evolution of unrecoverable strains in superelastic NiTi elements under cyclic deformation [27,41,140,141,115,133–139].

Delville et al. [40] observed a larger amount of unrecovered strain for the wire with a bigger grain size (attributed to the operation of several slip systems in austenite) concerning that of wire with smaller grain size. Atli et al. [142] studied the influence of the crystallographic compatibility between martensite and austenite during the transformation process, on the residual strain and strain evolution in nitinol alloy during thermal cycling (under constant stress) at different pre-stress levels. They showed that the amount of residual strain evolved upon the initial few numbers of thermal cycles depends on the resistance to defect propagation of the SMAs; the parameter which can be controlled

primarily by grain size and the initial dislocation density. There are experimental pieces of evidence in the literature suggesting that dislocation defects are created along with twin interfaces in the stress-induced martensite [142,143]. Heller et al. [34] found out that the unrecovered strains evolve upon both forward and reverse phase transformation and it increases exponentially with increasing stress and temperature, at which the forward and reverse martensitic transformations proceed. The induced unrecovered strain during reverse phase transformation was found to be comparable or even larger than that in the forward transformation stage in most of their superelastic and actuator tests on medical graded NiTi wires (the medical-grade NiTi wires are characterized by small unrecovered strains accumulating in thousands of cycles till failure).

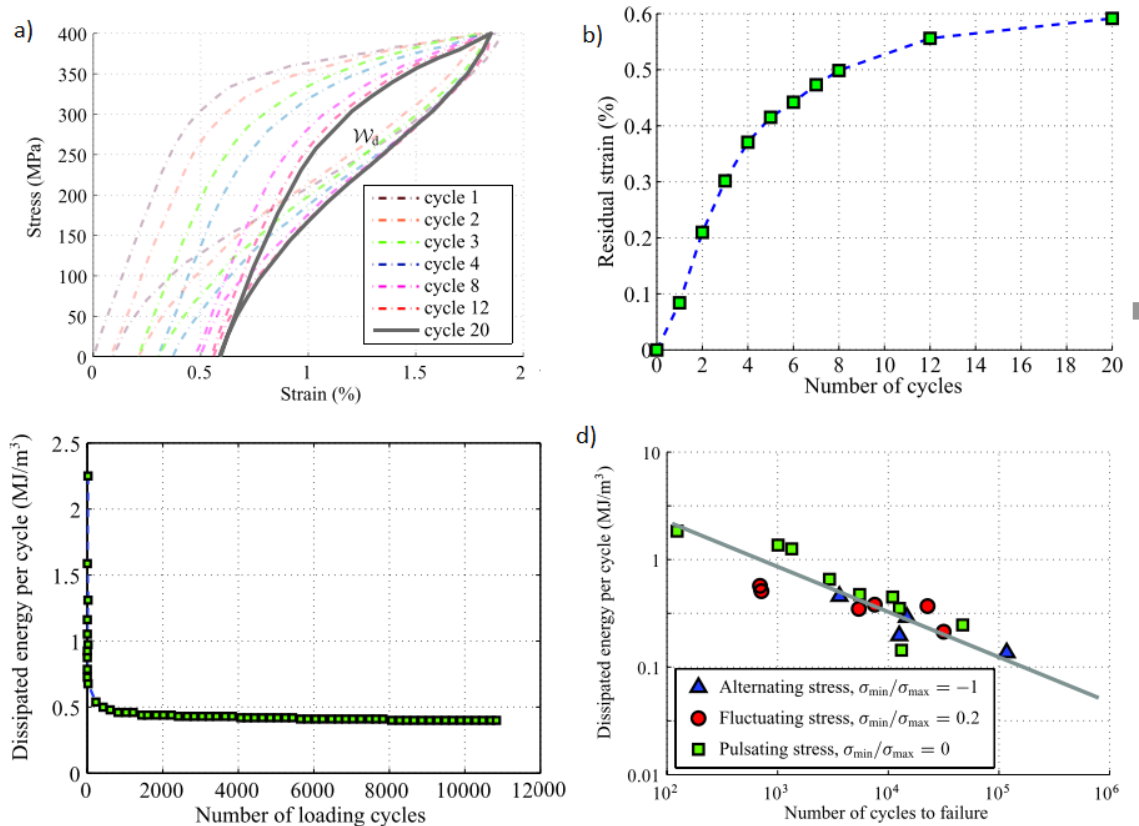


Fig. 2-20 a) experimental stress-strain response of a NiTi wire to repeated tension, b) residual strain evolution with the number of tension cycles, c) dissipated energy per cycle versus the number of loading cycles, d) experimental results for dissipated energy per cycle as a function of the number of cycles to failure [41]

It is known that the unrecovered strains will reach a saturated value after a few tens of cycles under uniaxial and biaxial loading conditions (i.e. saturates) [41,115,130,144]. It means that the unrecovered strains evolved upon per single transformation cycle gradually reduces until it vanishes, and the materials approach to its stable cyclic behavior. The importance of the irreversible strains become more revealed when it was found out that it has a linear relation to the structural fatigue of NiTi material. Moumni et al. [41,115] showed that the stress-strain response of the material stabilizes after the first few tens of cycles and presented an energy-based low-cycle fatigue criterion correlating the plastic-like shakedown; they exhibited that the stabilized residual strain, thus the dissipated energy of the stabilized cycle, is a relevant parameter for estimating the number of cycles to failure of such materials (Fig. 2-20), which was also reported by Kang et al. [145] (Fig. 2-21c).

Kang et al. [145] performed the stress-controlled tension-compression fatigue tests on superelastic NiTi SMA bars to study the instability of the cyclic behavior upon fatigue test (Fig. 2-21a) and its effect on the fatigue life. They observed that the number of cycles has almost linear dependent on the stable dissipated energy per cycle. It is showed that the stabilized dissipated energy per-cycle, thus the stabilized ratcheting strain greatly depends on loading conditions; i.e. the peak stress, strain/stress amplitude, and mean strain/stress [129,145], and it directly is linked to the fatigue life (Fig. 2-21b-c)

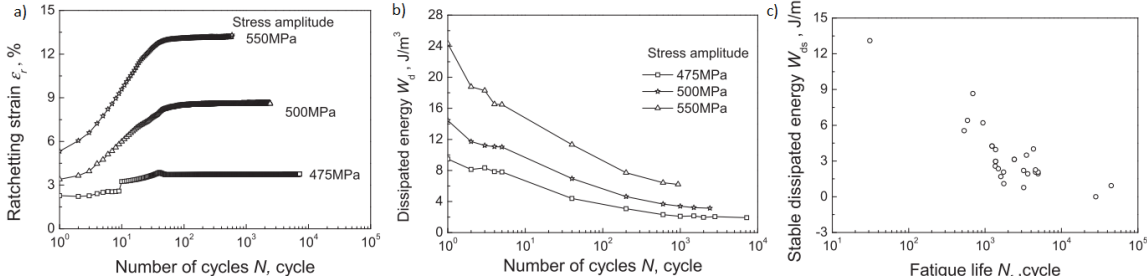


Fig. 2-21 a) Whole-life transformation ratcheting of super-elastic NiTi alloy in cyclic tension-compression tests with constant mean stress of 25 MPa and different stress amplitudes: curves of ratcheting strain ϵ_r vs. number of cycles N ; b) Functional fatigue of super-elastic NiTi alloy in the cyclic tension-compression tests with constant mean stress of 25 MPa and different stress amplitudes: curves of dissipated energy W_d vs. number of cycles; c) Relationship of stable dissipated energy and fatigue life for the super-elastic NiTi alloy obtained in stress-controlled cyclic tests [145]

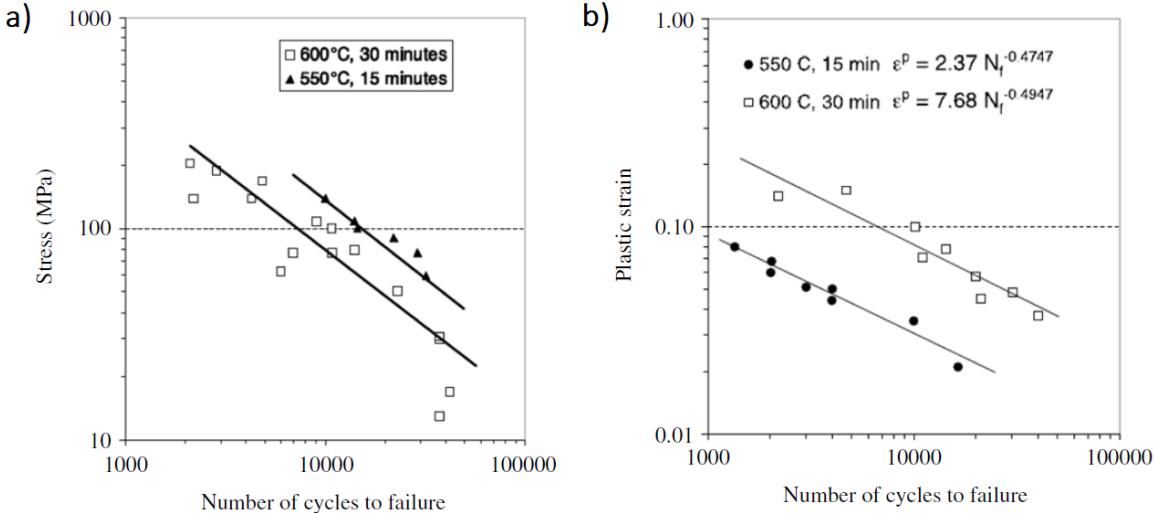


Fig. 2-22 a) constant axial stress vs. fatigue life; b) plastic strain vs. fatigue life for the case of complete thermally induced transformation under constant stress [146]

The direct relation between the accumulated irreversible strains at the stabilized cycle and the number of cycles to fatigue also has been reported in thermal cycling tests under constant external stress (i.e. under thermomechanical loading conditions) by Lagoudas et al. [146] (Fig. 2-22b). Lagoudas et al. [146] also observed that the heat treatment and the applied pre-stress have significant roles in the accumulated plastic strains –thus, on the fatigue life– of thermomechanical cycled NiTi wires [146] (Fig. 2-22a).

- *Resolving the Unrecovered Strains in SMAs by Controlling the Microstructure*

Most of the commercially available nitinol alloys display permanent irreversible changes in their functional properties hampering them in applications that need high transformation temperatures and high strength, as they generally engage in martensitic transformation below 100°C; and have low strength against dislocation plasticity, which results in their functional fatigue phenomenon [147] as outlined in the previous section. However, there have been reported a variety of methods to address eliminating or minimizing the problem, associated with the specimen's preparation methods and the materials composition.

As an example, Ni-rich compositions of binary NiTi SMAs can form metastable, nanosized Ni₄Ti₃ precipitates that significantly influence transformation temperatures, matrix strength, shape memory characteristics, and mechanical properties [148–154]. All these effects are controlled by the size, volume fraction, and the interparticle spacing of the precipitates, which are a function of aging time and temperature. Evirgen et al. [155] investigated the role of the microstructure of Ni-rich Ni_{50.3}Ti_{34.7}Zr₁₅ as a function of aging heat treatment –that result in a nanometer to submicron size precipitates– on shape memory behavior in load-biased thermal cyclic tests. Specifically, they selected the NTZ550/24h and NTZ600/100h samples, to compare the effect of significant changes in microstructures on the thermo-mechanical response of the alloy. In the NTZ550/24h sample, the precipitates were smaller than 90 nm and were absorbed by the martensite plates in which perfect shape recovery, (i.e., no unrecovered strains upon heating to austenite) was observed even at 300 MPa applied pre-stress, due to the increased matrix strength and because of the increased resistance to plastic deformation thanks to precipitation hardening (Fig. 2-23). The amount of unrecovered strains, ϵ^{irr} , is a function of the resistance to plastic deformation. During martensitic transformation, the local internal stresses arising can be much higher than the applied stress. Therefore, the material can locally undergo plastic deformation even if the applied stress levels are less than the yield strength of the material. So, when nano-size Ni₄Ti₃ precipitates form in the binary NiTi matrix, the yield strength of the transforming phases will increase, and excellent shape recovery is obtained [156] (Fig. 2-24). As is seen in Fig. 2-23b2, the NTZ600/100h sample containing large precipitates (>100 nm) –that limits the growth of martensite variants– exhibits small unrecovered strains under 200 MPa and fails at stresses above 250 MPa. This behavior was explained to be due to the presence of large precipitates that significantly alter the martensite morphology. It means that the large particles strongly interfere with the growth of martensite variants, as well as reorientation or detwinning of martensite, and precipitation hardening is less prominent compared to aged samples with relatively smaller precipitates.

Otsuka et al. [157] proposed several methods to improve the shape memory response of the NiTi-based HTSMAs (High-Temperature shape memory alloys) through increasing the strength of the transforming phases by i) quaternary alloying, ii) work hardening (cold working), iii) thermal cycling and iv) precipitation hardening. Coughlin et al. [158] showed that the precipitation heat treated alloy reaches 1278 MPa yield strength at temperatures as high as 250°C while showing very good superelasticity. The excellent superelasticity and excellent shape recovery as well as the improved dimensional stability as compared to any Ti-rich NiTi-based alloy as a result of the formation of nanosized precipitates. They remarked that when the Ni-rich Ni_{50.3}Ti_{29.7}Hf₂₀ is aged at 550 °C for 3 h, precipitates smaller than 30 nm in size, are present (Fig. 2-24b) [159] and the material shows very

good dimensional stability and a very small amount of plastic strain after 100 cycles under 200 MPa applied stress (Fig. 2-24c) [156].

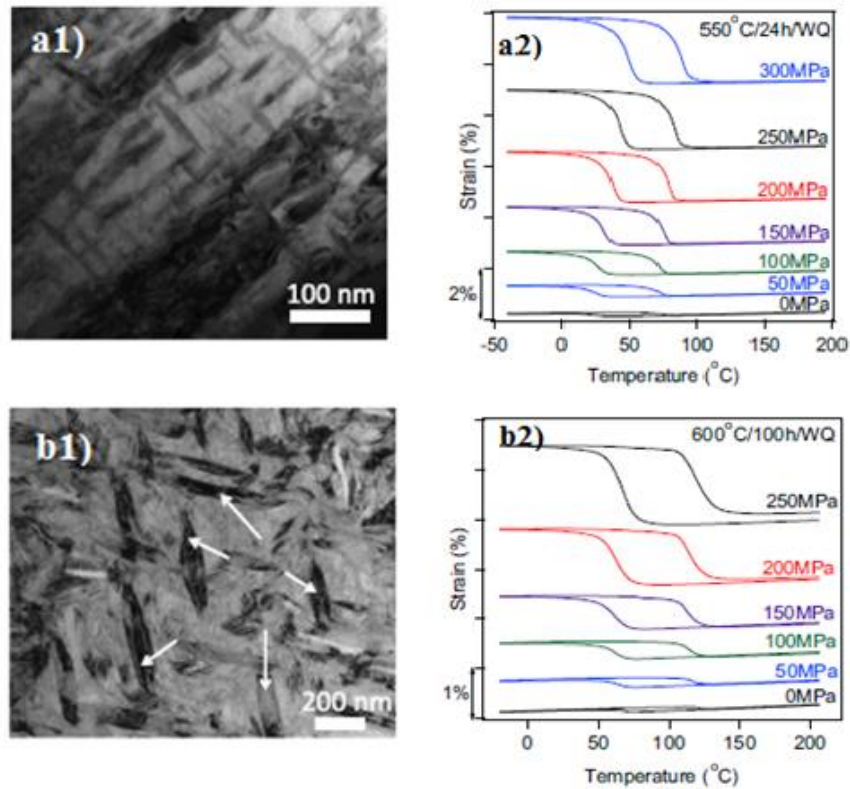


Fig. 2-23 Bright-field transmission electron microscopy images of $\text{Ni}_{50.3}\text{Ti}_{34.7}\text{Zr}_{15}$ (at%): a) sample aged at 550 °C for 24h, b) sample aged at 600 °C for 100h. precipitates are marked with arrows in image b, redrawn from [155]

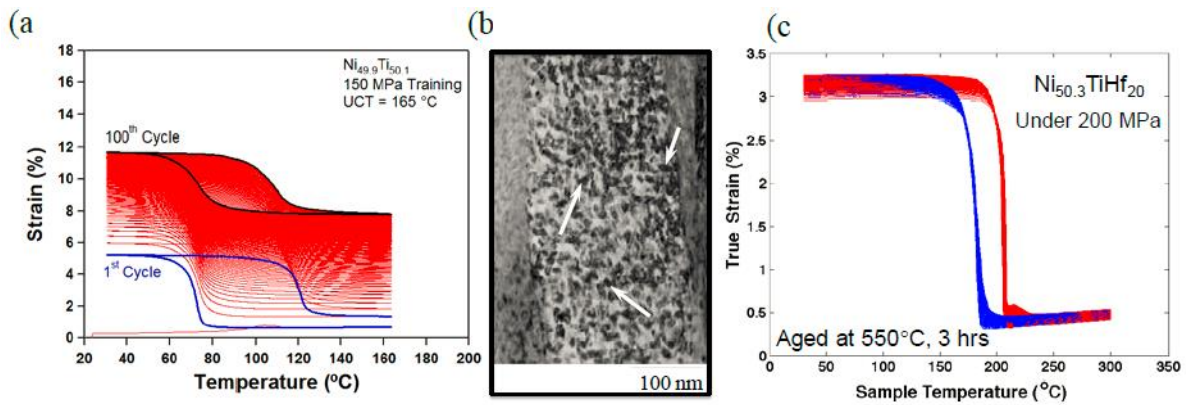


Fig. 2-24 a) Thermo-mechanical cycling response of a Ti-rich $\text{Ni}_{49.9}\text{Ti}_{50.1}$ SMA under 150 MPa demonstrating large dimensional stability. b) Ni-rich $\text{Ni}_{50.3}\text{Ti}_{29.7}\text{Hf}_{20}$ aged at 550 °C for 3 h showing nano precipitates smaller than 30 nm in size [159] and c) the corresponding thermo-mechanical response under 200 MPa applied stress for 100 cycles [156]

2.4. Stress raisers in phase transforming NiTi

1.1.5. Monotonic Loading

The most characteristic feature in the fracture of SMAs is the formation of a local transformation zone at the tip of the crack/notch. Upon the monotonic isothermal loading of an SMA material, in the superelastic (or martensitic) state, the elastic deformation occurs until the martensitic transformation (or reorientation of twinned martensite) induced by stress begins. Then, more applied load turns into elastic deformation of the detwinned martensite, which could be followed by plastic deformation of martensite [160–164] –or incorporation of B2 \Rightarrow B19' \Rightarrow B2T (i.e. stress-induced martensitic transformation into twinned austenite coupled with dislocation slip) at higher temperatures [132]– and final fracture [12,164,165] (Fig. 2-25).

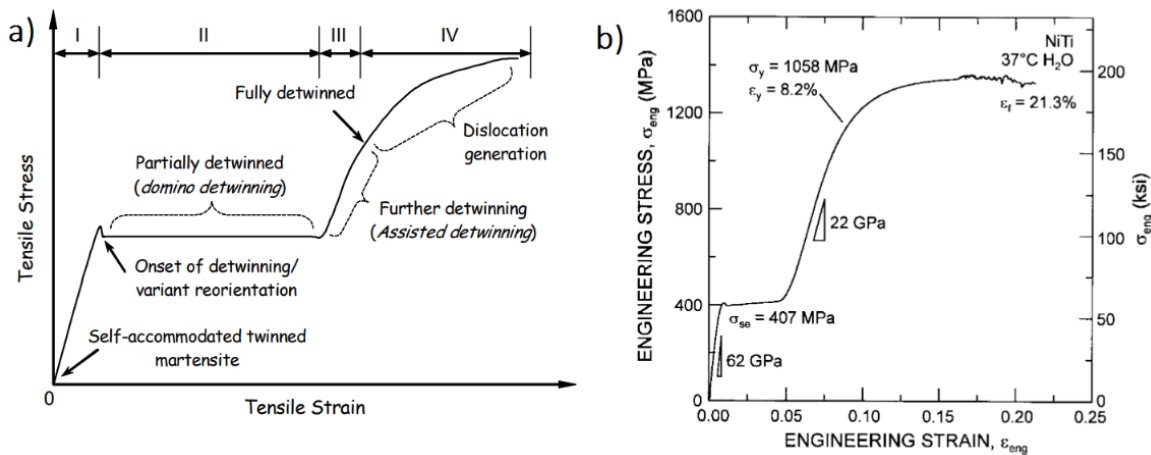


Fig. 2-25 Typical stress-strain response of shape-memory NiTi alloy under tension a) in the martensitic state [162]; b) in the superelastic state [12]

The stress level is always higher at the tip of stress raisers than that in the bulk, due to the stress concentration effect. Thus, the abovementioned phenomena take place preferably locally at the location of these geometric defects [24,25], which can result in heterogeneous progress of martensitic phase transformation in the specimen and complex local stress redistribution, and may change the driving force parameters [26–30].

The evolution of stress-induced martensitic transformation at the crack-tip in shape memory alloys was reported by Lu et al. [166], Vasko et al. [167], and Loughran et al. [168] in single-crystalline Cu-based SMAs using in-situ TEM and SEM, and by Robertson et al. [169] and Gollerthan et al. [170] in superelastic polycrystalline NiTi by in situ x-ray micro-diffraction observations. Then shape and size of the stress-induced transformation zone were assessed in the literature and several investigation techniques have been applied to analyze near crack-tip transformations, such as synchrotron X-Ray micro-Diffraction (XRD) [171,172], Infrared thermography (IR) [117,173,174], and instrumented nanoindentation [10,175]. In addition, displacement fields near the crack-tip regions have been analyzed using DIC [10,26,117,176,177] and Finite Element Method [24,28,165,178–181].

Daymond et al. [171] performed in situ synchrotron X-ray diffraction measurements to create two-dimensional maps of strain fields and texture around the tip of the crack at the root of the notch in CT martensitic NiTi specimens under plane strain conditions, averaged over the thickness, and observed strong texture ahead of the crack-tip in the as-fatigued specimen and concluded that it is

corresponding to detwinning of twinned martensite, as it was eliminated upon heating above the austenite finish temperature (A_f). Then they observed that upon subsequent application of static tensile stress, the highly textured zone reappears and grows around the crack-tip as the applied stress is increased. At the highest applied stress intensity, large tensile strains were measured ahead of the crack-tip and considerable elastic anisotropy was observed. The texture in this zone was not remarkably changed after mechanical unloading, unlike the substantial triaxial compressive residual strains developed within this zone after each unloading step, because of incompatibility between the detwinned zone surrounded by an elastic ligament which tends to return to its original configuration after unloading [5] (Fig. 2-26). Gollerthan et al. [174] used in-situ x-ray microdiffraction, SEM, and thermography and observed the formation of the stress-induced martensite and its reverse transformation to austenite at the crack-tip upon static loading and unloading of NiTi CT specimen in-plane strain, below the critical stress intensity (stationary crack). Their results showed two zones corresponding to the local stress-induced transformation from B2 to B19' form ahead of the crack-tip, one close to the crack-tip (tensile stress state) and the other at the end of the crack's cross-section (compressive stress state) which was in line with their previous synchrotron results [170] and later on in a numerical study by Hatefi Ardakani et al. [182] (Fig. 2-27).

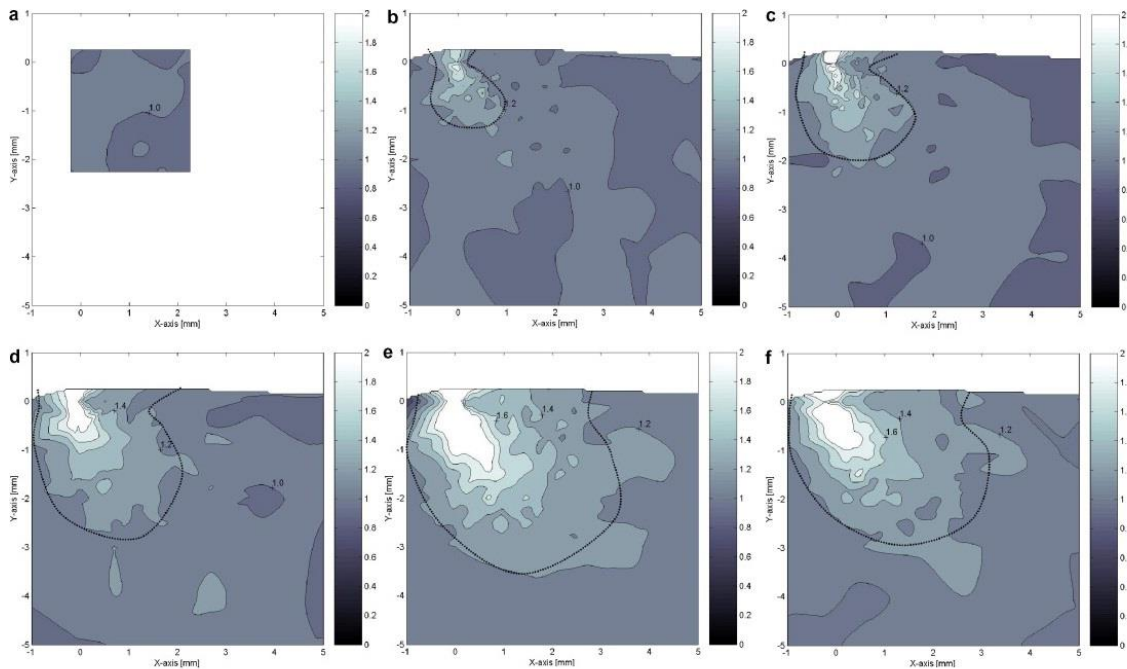


Fig. 2-26 Evolution of texture maps showing (010) normalized peak intensity parallel to the y-direction (perpendicular to crack growth) for various KI (MPa m^{1/2}); a) 0, (b) 20, (c) 25, (d) 30, (e) 35, (f) 0 (unload), redrawn from Daymond et al. [171]

Since the transformation at the stress raisers turns in local stress redistributions the accurate determination of mechanical fields near notches/cracks, employing realistic stress-strain relations of SMA material, are of fundamental importance. As the analytical models are often accompanied by mathematical difficulties and are much more complicated than the numerical ones, mostly numerical models and experimental methods were used to investigate the evolution of martensitic transformation around the cracks and notches, which are comprehensively reviewed in the following sections.

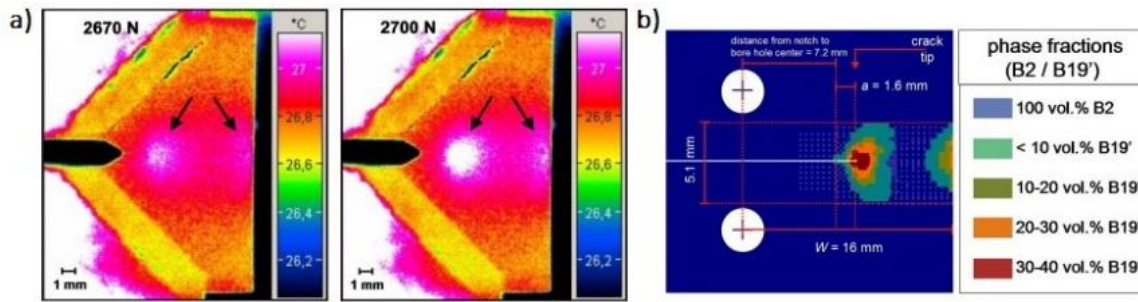


Fig. 2-27 a) Thermographic images of a pseudoelastic NiTi SMA CT specimen obtained during in situ dynamic loading sequence below the critical load for crack extension (stationary crack). Two zones with significant local heat evolution are marked with black arrows. Redrawn from Gollerthan et al. [174]; b) Formation of local stress-induced transformation from B2 to B19 at the end of CT specimen, ahead of the crack-tip, redrawn by Gollerthan et al. [170]

- *Effect of martensitic transformation and plasticity on fracture behavior*

Superelastic regime

To do fracture mechanics study in engineering design and structural analysis, fracture toughness is required to serve as a material property that can be transferred from the assessments to a structural application. Principally, the fracture behavior of metallic alloys correlates to the micro-mechanism of fracture and is usually outlined as being ductile or brittle. Brittle fracture performance results in the development of rapid and unstable crack extension since the energy stored in the test machine at the onset of crack extension is higher than the energy required for the crack to further grow. The specimen fails unstably, and quantification of the fracture resistance beyond initiation is not possible. In fact, the brittle fracture behavior can correspond to cleavage fracture or micro-ductile void growth fracture and can be induced by effects such as flawed material processing or segregation of deleterious impurities at grain boundaries. In brittle fracture, macroscopically a well-defined point of crack initiation is related to an abrupt drop in load. This single value characterizes the fracture failure and gives the value of the fracture toughness [5,183,184]. The definition of toughness as a fracture parameter value is linked to the concept of stress intensity factor and energy release rate. By definition, the stress intensity factor (SIF) is the magnitude of the crack-tip stress field for a particular mode in a homogeneous linear elastic material, usually symbolized by K_I (in mode I). According to this approach stress state at the tip of a crack is proportional to the stress intensity factor [185]. Under tensile loading, unstable crack growth occurs when stress intensity K_I attains the single critical value (K_{IC}) and this causes failure of the components. Indeed, K_{IC} is a measure of the ability of a material to resist the growth of a pre-existing crack or flaw and is used extensively to design fracture safe structures. The energy approach [186], on the other hand, states that the crack extension occurs when the energy available for crack growth is sufficient to overcome the resistance of the material, i.e. crack propagation will occur if the energy released upon crack growth is sufficient to provide all the energy that is required for crack growth [185]. The energy release rate (or crack extension force) G_I is the crack driving force in Mode-I condition. K_{IC} and G_{IC} are called the fracture toughness of the material (i.e., material resistance to fracture) [187].

Ductile fracture is a mode of material failure in which voids -either already existing within the material or nucleated during deformation- grow until they link together, or coalesce, to form a continuous fracture path that tends to absorb more energy. For ductile fracture, the plastic deformation

dominates at the crack-tip and the material resistance against fracture increases as the crack grows, and thus tougher materials exhibit slow and stable crack growth and the toughness is often described in a resistance R-curve format using the J-integral or CTOD (δ) [183,188]. J-integral is a nonlinear useful measure of fracture toughness, proposed in 1968 by Rice [189], to characterize the intensity of elastic-plastic crack-tip fields, and symbolizes the elastic-plastic fracture mechanics. The CTOD, proposed in 1963 by Wells [190], can be identically utilized as K or J in engineering fracture mechanics, while the CTOA parameter is being recently used in stable crack extension for thin-walled materials. The whole R-curve may be utilized to evaluate the ductile fracture; however, a single-point value of toughness is still used in methods that require fracture toughness in structural integrity assessment. This typical single-point value in ductile materials is defined near the onset of crack tearing characterized by a change in the slope of the R-curve [183].

In SMAs, heterogeneous proceeding of martensitic phase transformation, reorientation of martensite variants, the potential for plastic deformation upper transformation plateau stress or transformation induced plasticity, and intrinsic thermomechanical coupling [23,25,34,132,191] turn into a complex stress/strain redistribution around an existing stress raiser that can significantly change the fracture parameters and result in stable crack growth under a mechanical/thermomechanical loading condition [26,28,182]. Accordingly, SMAs –similar to ductile metals– show stable crack growth behavior, the so-called transformation toughening. It means that in quasi-static loading samples do not rupture suddenly after a specific load is reached; instead, stable crack growth is seen by rising resistance to crack advance [192]. This phenomenon is known to be due to the energy dissipated by the stress-induced martensite left behind the advancing crack-tip which must be granted by the external loading to keep the crack advance [178,192–195]. However, still, ASTM standards are being widely used in experimental assessments of fracture toughness of polycrystalline SMAs polycrystalline, the method which is designated based on the premise of Linear Elastic Fracture Mechanics (LEFM) and requires the assumption of the small scale nonlinearly deformed zone at the crack/notch-tip regardless of the mechanism. This assumption should then apply to the size of the martensitic transformation zone at the crack-tip which is an underestimation of the transformed zone [191]. The representation of crack extension in polycrystalline SMAs in the rising R-curve is very rare in the literature [192,194,196–198]. Furthermore, the use of LEFM equations –in ASTM methods– to evaluate the stress intensity factor cannot capture the realistic local response in specimens where the martensitic transformation is involved [170,199].

Gollerthan et al. [170] used SEM and X-ray Synchron diffraction methods and showed that the formation of detwinned martensite at the tip of advancing crack, decreases the resistance to crack extension (K_{IC}) (Fig. 2-28) in plane-strain. However, they used the conventional criteria of the promise of LEFM, i.e. to check if the size of the non-linear deformation zone at the crack-tip is smaller than a fraction of all the characteristic dimensions of the crack configuration (based on $(1/3\pi)(K_{IC}/\sigma^y)^2$), which is not satisfied in phase transformation zone. But, they remarked that the LEFM cannot capture the realistic response of the martensitic and pseudoelastic specimens (as it was also outlined by Sgambitterra et al. [199]) since in both cases they observed deviations from linearity in $P(\Delta)$ curves before the onset of macroscopic crack growth (Fig. 2-29a & b) -which rather increases by increasing the initial a/w ratio-. They did not observe crack-tip blunting and proposed the growth of favorably oriented martensitic variants (in martensitic NiTi specimens) and the formation of stress-induced martensite (in pseudoelastic NiTi specimens) to account for these deviations from linearity; while the very tiny deviations from linearity in austenite specimen (where the martensitic

transformation is suppressed) (Fig. 2-29c) was assumed to be related to the crack-tip blunting induced by dislocation plasticity [200,201]. Further, due to the immediate reverse martensitic transformation behind the advancing crack-tip was assumed the reason why martensite could not be detected on fracture surfaces. By an X-ray line profile analysis on the same samples, as studied in [170,174]. Ungar et al. [202] observed the remnant martensite at the fracture surface in the region of the static loading and stable crack growth, stabilized by large dislocation densities in two phases, while they concluded that at the unstable crack growth/fracture (when the load decreases while the crack propagation rate increases) the martensitic transformation is suppressed under plane strain;

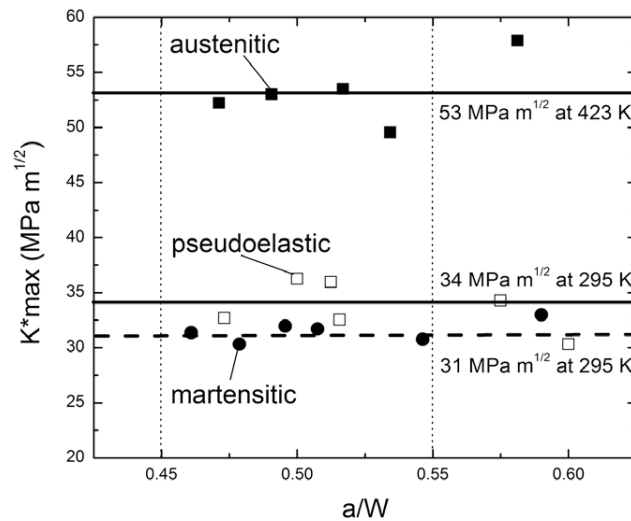


Fig. 2-28 Comparison of K_{max}^* for martensitic, pseudoelastic and austenitic NiTi SMAs, redrawn from Gollerthan et al. [170]

Attempts also have been recently done to evaluate the stress intensity factor and material's toughness by fitting the full-field displacement data obtained from Digital Image Correlation (DIC) to the traditional William's expansion series [10,117,199,203–205]. For instance, Maletta et al. [117] tried this method, for a cracked thin NiTi plate subjected to fatigue loading, and calculated the mode I stress intensity factor, and observed a marked nonlinear hysteretic in the evolution of the crack-tip stress intensity factor .vs. the remote stress intensity factor (Fig. 2-30) which was affiliated to the phase transformation phenomenon [206]. Haghgouyan et al. [203] conducted fitted the displacement fields obtained from DIC, at the critical load point –where the crack extension immediately precedes– to the asymptotic near-tip opening displacement field using a least-squares minimization from Oral et al [29]. They showed that the K_{max} (at the moment of failure) at room temperature is much higher than that measured at martensitic transformation suppressing temperature ($T > M_d$), suggesting transformation toughening effect in plane-stress.

Sgambitterra et al. [199] performed a least-squares regression on the DIC measured displacement fields at the crack-tip of thin pseudoelastic sheets undergoing cyclic tensile loading at different temperatures to understand the effect of the temperature on the stress-induced transformation mechanisms at the crack-tip. By considering the severe non-linear behavior of NiTi alloys (which deviates the stress intensity values from that obtained by the theory of LEFM), and found out that the crack-tip SIF decreases by increasing the temperature, till the higher temperatures at which the martensitic transformation is vanished ($T > M_d$) and above these temperatures, the SIF tends to stabilize (Fig. 2-31).

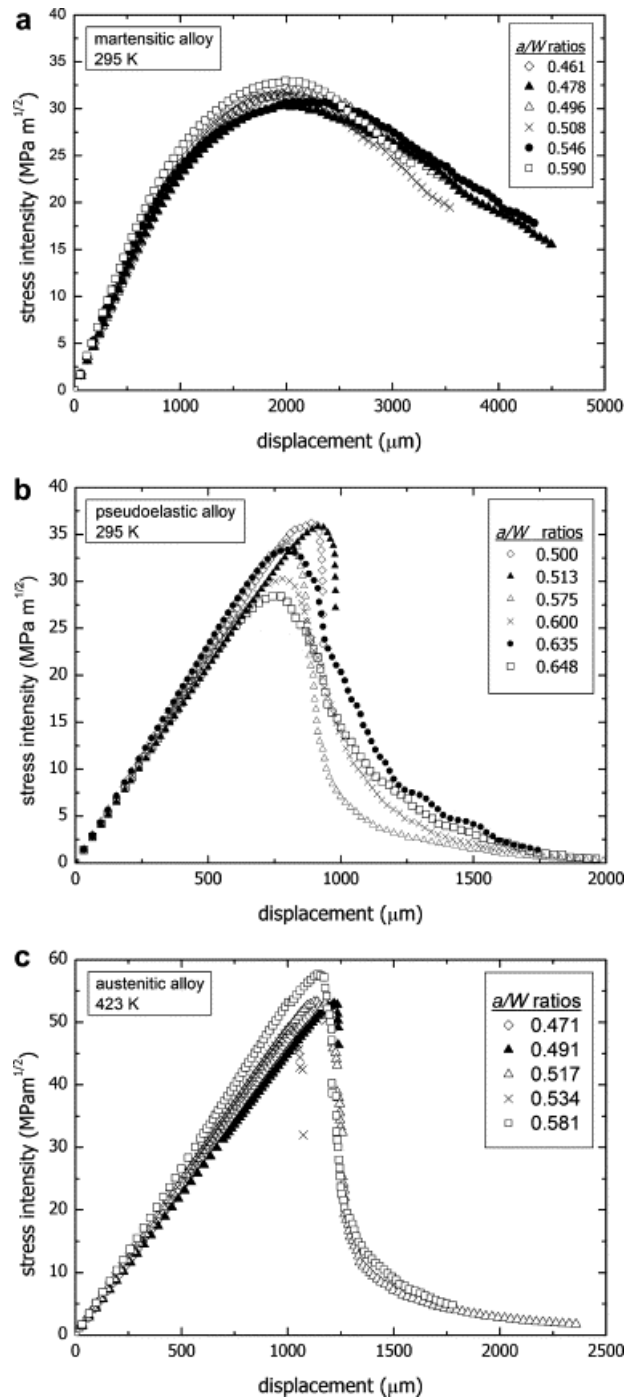


Fig. 2-29 Stress intensity (K^*) vs. displacement curves of the (a) martensitic NiTi SMA at 295 K, (b) pseudoelastic NiTi SMA at 295 K, and (c) austenitic NiTi SMA at 423 K ($T > M_d$) with varying a/W ratios. K^* displacement curves are derived from the equation given in the text for K^* , Redrawn from Gollerthan et al. [170]

Haghgouyan et al. [198] derived J_R -curve for NiTi CT samples using the concepts of Elastic Plastic Fracture Mechanics (EPFM), and the J-integral as the fracture criterion for which the specimen's dimensions are less strict to the critical stress intensity factor in compare to LEFM. They developed the ASTM E1820 (for ductile materials) to take into account the elastic moduli mismatch between austenite, self-accommodated martensite, and oriented martensite in SMAs. The extrapolated stress intensity factors from the fracture toughness (i.e. the critical J-values for crack growth) by $K_{JIC} =$

$(E'J_{IC})^{1/2}$ (where E' is the elastic moduli of the stable phase at the test temperature), was found out to be about three times larger than the ones reported in literature ($\sim 30 \text{ MPa}\cdot\text{m}^{1/2}$ for pseudoelastic NiTi at room temperature [169,170,207,208]) (see Fig. 2-32). Besides, they outlined that the fracture toughness of martensitic and transforming superelastic material are approximately the same (see Fig. 2-32) and remarked that it is probably since in both materials states the crack advances into a region of oriented martensite.

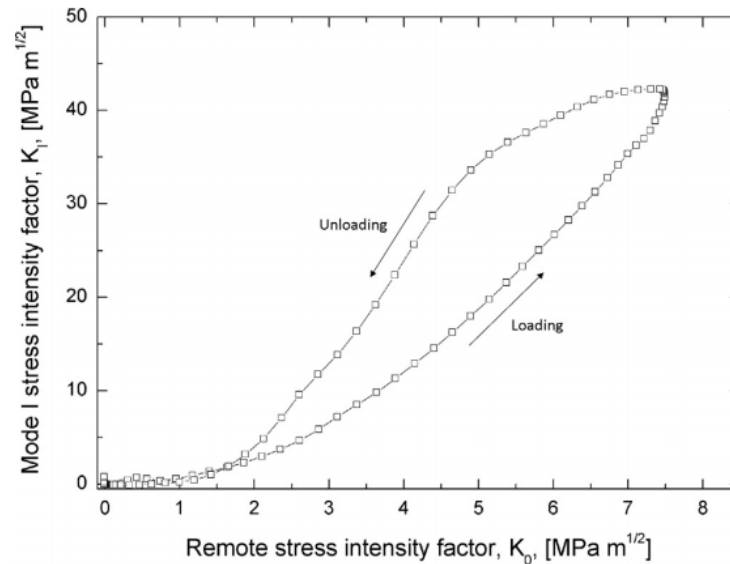


Fig. 2-30 Mode I stress intensity factor K_I as a function of the applied remote stress intensity factor K_0 [117]

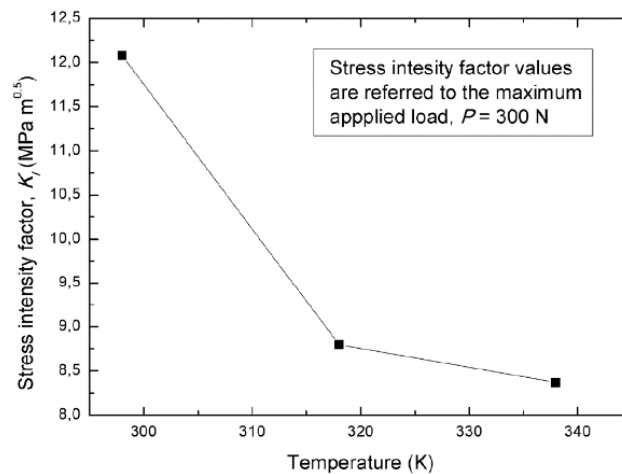


Fig. 2-31 Evolution of the Stress Intensity Factor (SIF), recorded at the maximum applied load ($P=300 \text{ N}$), as a function of the operating temperature, Sambitterra et al. [199]

The theoretical assessment of fracture parameters of SMAs has also attracted significant attention in recent years. Haghgouyan et al. [209] used the virtual crack closure technique -VCCT- in finite element analyses and experimentally measured fracture toughness to examine the stable crack growth in CT superelastic samples in mode I, in terms of the load-displacement curve, mechanical gradients, and the stress-induced martensite zone formed at the crack-tip vicinity. They explained the numerically derived load-displacement curve in three distinct stages (Fig. 2-33a): i) the linear

response correlated to a small-scale phase transformation at the crack-tip vicinity, ii) deviation from linearity, due to the large-scale transformation around the crack which is followed by iii) a gradual force relaxation without any abrupt drop representing the stable crack extension. Their curves showed a reasonable agreement to that measured by DIC, while the LEFM was seen to fail to predict the related response (Fig. 2-33b).

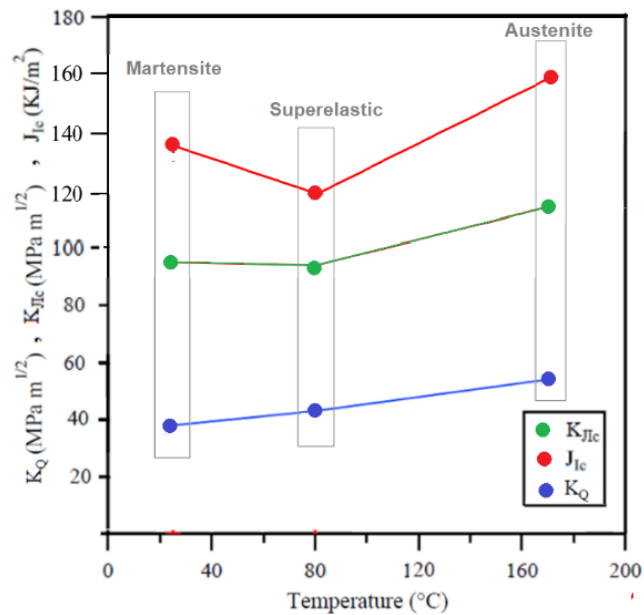


Fig. 2-32 The difference in the apparent elastic properties of the far-field material has an impact on the J_{Ic} -values but not on the extrapolated $K_{J_{Ic}}$ value. K_Q obtained from LEFM (if we assume it is valid) for comparison purposes. The K_Q values are similar to the ones reported in the literature [170,192,197,210–212] It is observed that at each testing temperature, the $K_{J_{Ic}}$ values are much higher than the corresponding K_Q values reported based on LEFM; redrawn from [198]

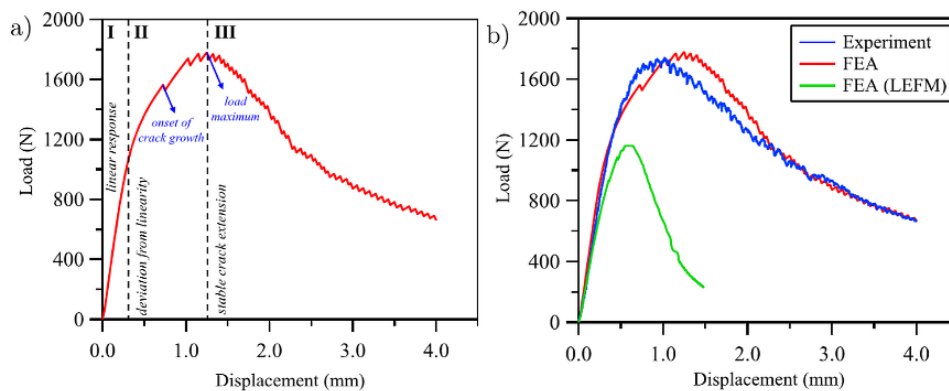


Fig. 2-33 a) Load-displacement curve under mode-I isothermal loading of the compact tension SMA model; b) comparison of the experimentally measured load-displacement curve compared to obtained in FEA and LEFM [209]

Baxevanis et al. [181] simulated quasi-static stable crack growth in SMAs under plane strain, using VCCT and finite element method, to measure the transformation toughening and its correspondence to the ratio between the far-field energy release rate and the crack-tip energy release rate. To interdict the reverse phase transformation at the crack wake and its effects they picked an analysis temperature laying between M_s and A_s . Their results revealed that the transformed material left behind the tip of the advancing crack induces crack closure stresses, thus increases the toughness. Baxevanis et al.

[213] studied the steady-state crack growth in superelastic SMAs under plane strain conditions by finite element simulations and found out that the training has a significant effect on the fracture toughness by shrinking the superelasticity stress-strain hysteresis. Their results further revealed that the toughness increase enhances monotonically as the transformation strain (ϵ^{tr}) increases.

Shape memory regime

The fracture analysis of SMA components which include stress raisers becomes even more complicated when corresponds to SMA elements subjected to thermo-mechanical loading conditions. Hence, successful implementation of SMA elements within the thermal actuator mechanisms requires the assessment of their fracture properties and studying the martensitic transformation interaction with crack/notch-tip stress state under various cyclic thermo-mechanical loadings, i.e. actuation loading conditions. So far, no experimental effort has yet been reported on the measurements of the fracture toughness of SMAs under actuation loading conditions. Indeed, there are few theoretical examinations of the evolution of mechanical gradients and fracture toughness of SMAs under thermomechanical loading conditions. Baxevanis et al. [28] numerically investigated the effect of stress redistribution caused by large scale phase transformation, on the mechanical gradients around the static crack, the energy release rate, and the crack growth driving force in in an infinite actuator center-cracked plate in plane strain. Their results revealed that that the energy release rate would reach the material's critical value upon cooling under a constant external load and crack growth initiates (also see [193] [214]).

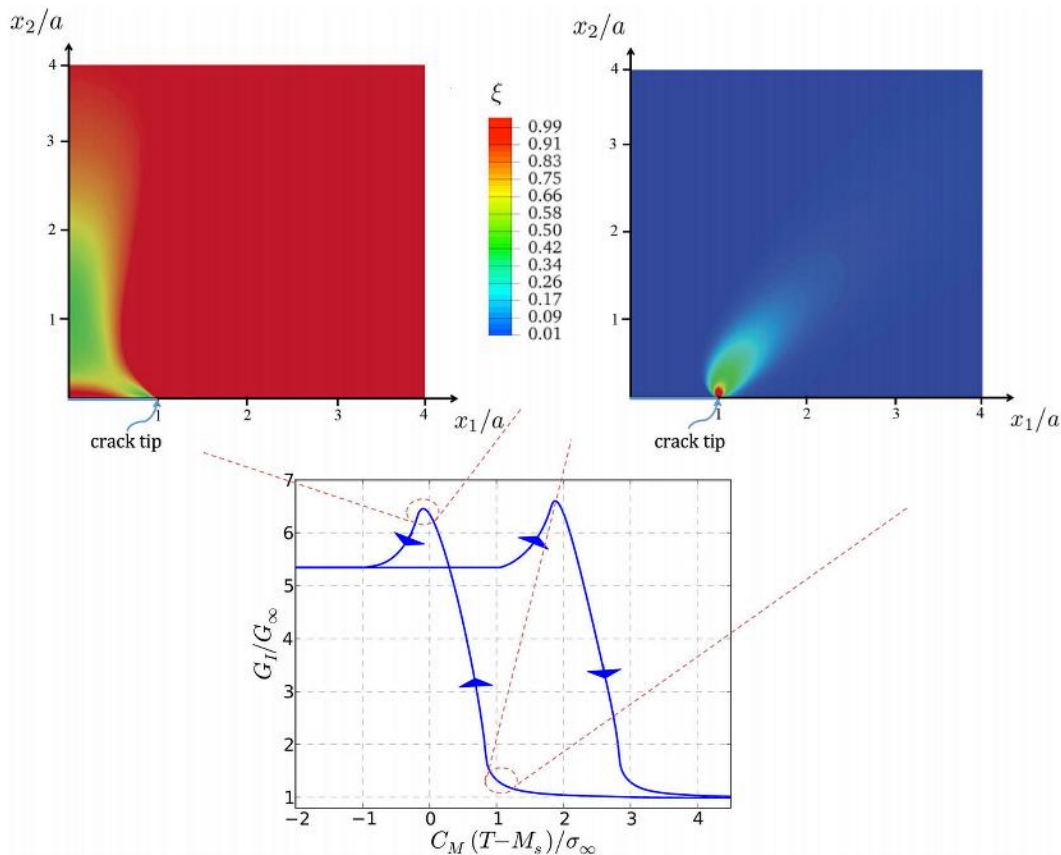


Fig. 2-34 Normalized energy release rate, G_I/G_∞ , versus normalized temperature, $C_M(T - M_s)/\sigma_\infty$, and martensite volume fraction during cooling [215]

Jap et al. [215] numerically analyzed the crack growth behavior in SMA in thermal cycling under a constant load in mode-I in plane strain using the virtual crack closure technique (VCCT). In their simulations it was assumed that the crack propagates at a critical energy release rate. They applied a pre-stress in the austenite phase which was enough high such that the critical crack-tip energy release rate is approached in cooling stage and turns into crack growth initiation. It was found out that the transformation induced stress redistribution upon cooling meaningfully increases the crack-tip energy release rate. During cooling G_I/G_∞ first increases till it reaches to a peak, and then decreases before reaching a constant value at $T=M_f$, when the whole specimen has fully transformed into detwinned martensite (Fig. 2-34). The energy release rate increase during cooling was affiliated to a ‘global’ phase transformation proceeding within a fan ahead of the crack-tip where the transformation strains have an anti-shielding effect. The subsequent energy release rate relaxation after the peak is reached was affiliated to phase transformation in regions behind the crack-tip.

Jap et al. [215] also showed that the stable crack growth occurs because of the transformation induced stress redistribution left at the crack wake, which protects the crack [28]. Such that, further cooling is required to maintain the stress high enough at the crack-tip, till the crack propagates to a distance much larger than its preliminary length, where the required temperature increment for the crack advance decreases and the crack reaches a steady-state growth at a constant temperature. Jap et al. [216] analyzed the effect of transformation induced plasticity (TRIP) during thermal cyclic actuation in plane strain by virtual crack closure technique (VCCT). It was found out that TRIP strains develop upon either forward or reverse phase transformation and accumulate during repeated cycles. Such that, the accumulation of TRIP strains increases the energy release rate and could result in approaching the crack-tip energy release rate to the material’s critical magnitude just after a few thermal cycles.

1.1.6. Fatigue Crack Growth

In most of their applications, SMAs are implemented in dynamic mechanisms that are designed to undergo cyclic loads and are prone to fatigue failure. Even though the literature suffers from the lack of understanding of the fatigue crack properties of SMAs under actuation loading conditions, there are a variety of studies were addressed the fatigue crack growth in the superelastic regime. However, in general, still, our understanding remains poor since our comprehension of the fatigue crack growth in SMAs is mainly based on the test methods (for instance ASTM) designed for classic untransforming materials.

the following important conclusions are drawn on the effects of martensitic transformation on fatigue crack growth:

- the crack growth rate in the martensite state is lower than that in superelastic and austenite [217].
- under the fatigue of thin NiTi CT samples, the residual strains and retained martensite (after unloading stages) evolve. In fact, the martensite is stabilized by plastic [169]. The martensite is stabilized by plastic strains, where the dislocation tangles pin the martensite variants to transform reversely to austenite.
- since the martensite was not seen on the fracture surface of an as fatigued specimen, it is concluded that the martensitic transformation could be prohibited upon the catastrophic fatigue crack growth [26,169].
- Interestingly, this trend was observed in monotonic fracture by Ungar et al. [202], where they observed the residual martensite at the stable crack growth regime of the fracture surface

–pinned by dislocation density–, while the martensite was not seen in catastrophic fracture surface, attributed to the reverse transformation at the crack wake upon the stable static crack growth.

The crack growth rate in SMAs is a function of several factors. These factors may include but not limited to: elastic moduli mismatch between austenite and martensite [26], grains' orientation (texture) [169] and grain average size [218], loading frequency, load parameters ($\Delta k, k_{max}, R = \sigma_{min}/\sigma_{max}$).

- *The effects of loading range and frequency*

In SMAs, there is a region at the crack-tip which frequently experiences back and forth phase transformation, and a far-field ligament permanently untransformed austenite (due to low-stress levels in distance from the crack-tip). There is also another possibility when: either both minimum and maximum applied stress intensities are high enough to cause martensite to form at the crack-tip, or when the martensite is stabilized at the crack-tip by plastic deformation; then, in addition to those two mentioned regions, there is always a permanent martensite inclusion at the very vicinity of the crack-tip. Attributed to the formation of the transformation zones around the crack-tip, the severe local stress and strain redistribution occur in these alloys which analyzes their fatigue crack growth behavior more complex. On the other side, the formation of these regions is dependent on several factors, including the load frequency, load level, and stress triaxiality (i.e. plane-stress .vs. plane-strain) [219–221]. The stress triaxiality effect arises from the fact that under plane strain conditions the high hydrostatic stresses developed in front of a crack tip could suppress the stress-induced martensite to form, as was proposed by Wang et al. [219] by numerical analysis. However, there is a serious lack of experimental proves to this theory. In contrast, the only experimental x-ray Synchron diffraction observations made by Gollerthan et al. [170] on the CT NiTi specimens in plane-strain was claimed to reveal clear evidence of the formation of stress-induced martensite at the crack-tip. Nevertheless, one should note that there are potentially two sources of uncertainty in their experimental observations,

- first is using the linear elastic criteria outlined in ASTM to check the plane-strain dominant, i.e. to examine if the size of the non-linear deformation zone close to the crack tip is smaller than a fraction of all the characteristic dimensions of the crack configuration (based on $(1/3\pi)(K_{IC}/\sigma^y)^2$). In ASTM the non-linearly deformed zone refers to the small-scale plastically deformed area at the crack-tip and σ^y refers to the yield stress. In SMAs, however, the small-scale extend of phase transformation is an absolute underestimation. Further, Gollerthan et al. [170] still used the materials yield stress in the abovementioned equation, while in SMAs the preliminary yield occurs due to martensitic phase transformation and the critical stress of transformation stress plateau ($\sigma_s^{A \rightarrow M}$) should be considered as the yield stress.
- second, synchrotron x-ray micro-diffraction mapping represents volume-averaged values through the specimen thickness, i.e., between plane stress conditions at the specimen surfaces and plane strain conditions in the center [170], and cannot guaranty the formation of stress-induced martensite at the center [222–224].

Usually, in metallic alloys and compounds, the lower the loading frequency results in higher fatigue crack growth rate, due to the more active time of the corrosion [192]. In SMAs, however, the effects of loading frequency remain inconclusive and there are contradictions between the remarks in the literature. The loading frequency persuades a strong thermomechanical coupling in SMAs that affects the fatigue behavior [52,225,226] which in turn should affect fatigue crack propagation. In fact, the changes in load frequency change the stable response of the SMA materials [226–228] –which is

reported to be achieved after a limited number of cycles [125,134]–, affects the formation of Lüders-band in NiTi [16,221,229–231], and further changes the size of the fully and partially transformed material ahead of the crack-tip [232] (see Fig. 2-35 and Fig. 2-36).

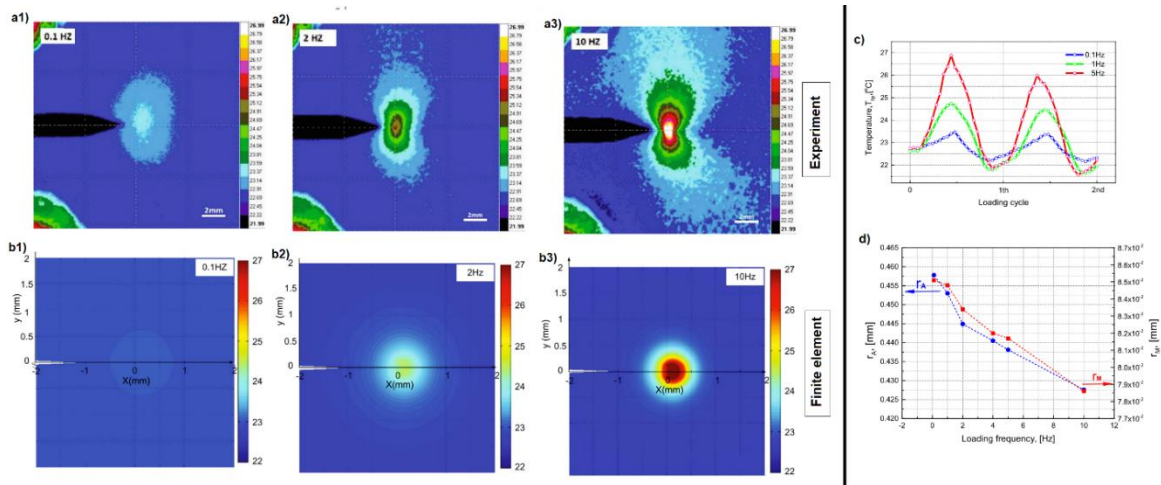


Fig. 2-35 Comparison of experimental temperature measurements (top, a1-a3) and FE simulations (bottom, b1-b3), c) Evolution of the maximum temperature, T_{max} at the crack tip at different loading frequencies, d) Extent of regions of martensite and austenite along the x-axis versus loading frequency, redrawn from [232]

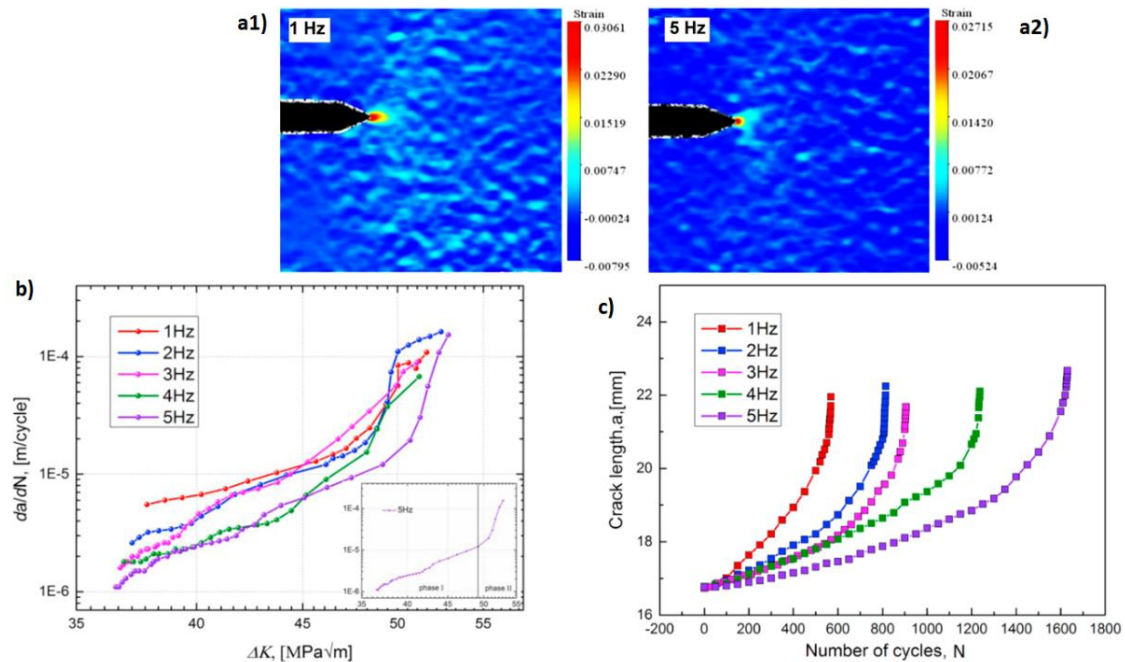


Fig. 2-36 Normal strain field around the crack tip obtained from DIC at the maximum load at (a1) 1 Hz, (a2) 5 Hz at the 300th cycle; b) da/dN vs ΔK at different loading frequencies, c) Crack length vs N at different loading frequencies.

Redrawn from [220]

Apart from the frequency effects, it was revealed that the fatigue crack growth rate is a function of both Δk and k_{max} parameters at a constant load ratio (R) [220,233] (see Fig. 2-37 and Fig. 2-38), and stress triaxiality (i.e. plane strain vs. plane stress). For superelastic NiTi in the near-threshold regime, it is shown that the ΔK_{th} decreases with an increasing load ratio. For instance, Stankiewicz et al. [146] reported a ΔK_{th} reduction from 2.5 $MPa\sqrt{m}$ at $R = 0.1$ to 1.4 $MPa\sqrt{m}$ at $R = 0.7$. They attributed this reduction, in the threshold stress intensity factor, to lower crack closure at a higher load ratio.

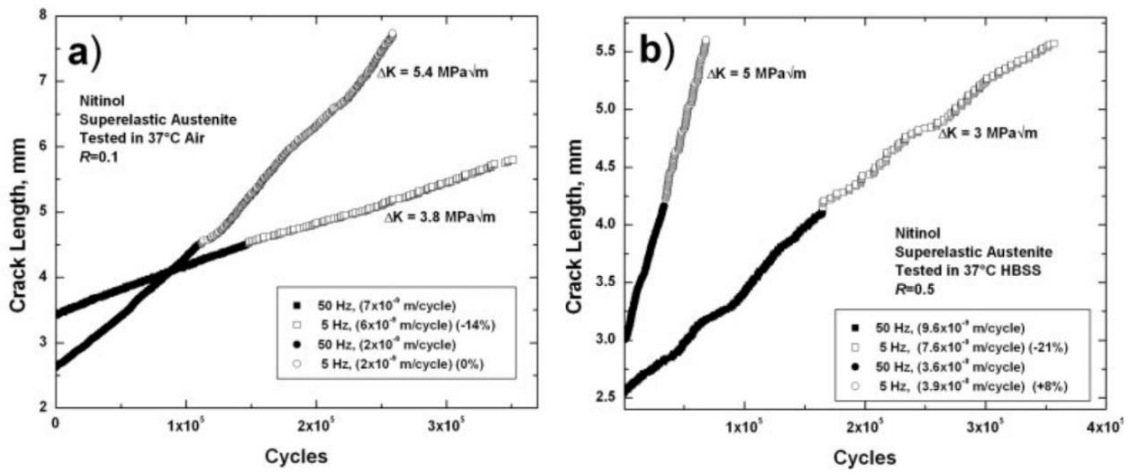


Fig. 2-37 Constant Δk experiments show effect of cyclic frequency on crack-growth rates in superelastic austenitic Nitinol at 37°C in environments of: a) air with R=0.1, b) HBSS with R=0.5, using 0.4mm thick CT specimens laser-cut from flattened thin-walled Nitinol tubing [233]

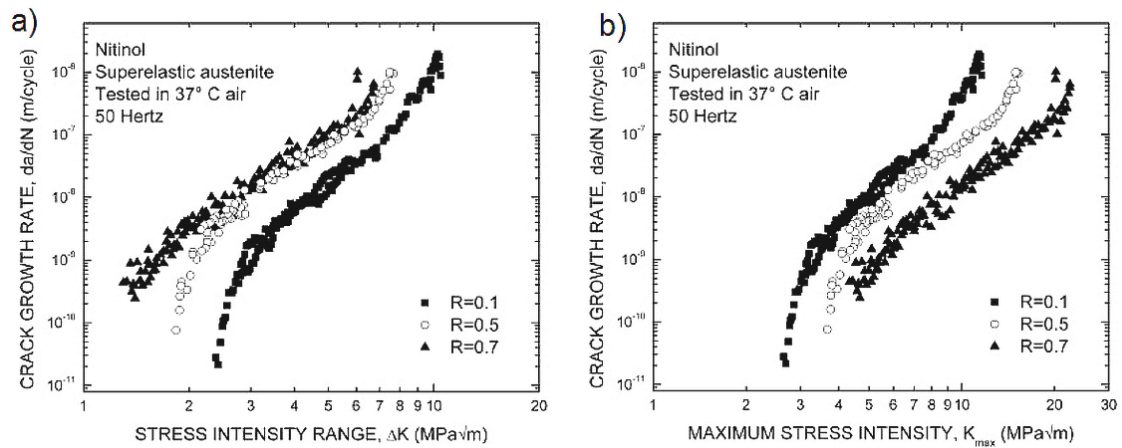


Fig. 2-38 The effect of the a) load ratio and Δk , b) the effect of k_{max} , in 37°C air at a frequency of 50 Hz, using superelastic austenitic Nitinol 0.4mm thick CT specimens laser-cut from flattened thin-walled Nitinol tubing [233]

CHAPTER 3. Materials and Methods

3.1. Introduction

Superelastic and shape memory NiTi notched thin ribbons are subjected to iso-thermal tensile cyclic loading-unloading and thermal cycling under stress, respectively. The DIC method is used to capture the evolution of the strain fields. The structural changes in NiTi around the notch were analyzed using synchrotron X-ray micro-diffraction. The finite element (FE) method is used to thoroughly analyze the evolution of the mechanical gradients, the deformation mechanism, and the martensite volume fraction around the notch. In FE numerical simulations, a recently developed three-dimensional phenomenological macroscopic model for shape memory alloys proposed by Choudhry and Yoon [57] is used, which is implemented in MSC Marc finite element commercial package. This model enables us to combine the SMA constitutive behavior (martensitic transformation) with the plasticity of both the austenite and martensite phases. However, the yield stress of the austenite phase is set to infinity. Suppression of the austenite yielding is in agreement with experimental proof [34] showing that the MT plateau stress is below the yield stress of austenite at room temperature range. In other words, the term plasticity in the present thesis refers to the martensite yielding at high stress levels beyond the martensitic yield stress [37,162,234], which differs from the plasticity coupled by forward and reverse phase transformation (TRIP) [33,34,235], as it was discussed in section 1.1.

In the following, the experimental procedure is explained, and the constitutive material model used in FE simulations is briefly introduced. Indeed, the geometrical aspects of FE models and the applied loading conditions for each case-study are discussed in the corresponding chapter in the thesis.

3.2. Experiments

The experiments on the present Ph.D. thesis (DIC measurements and X-ray microdiffraction observations) are used to verify the predictions made by numerical simulations, which were performed by students' co-supervisor, Dr. Ludek Heller in the institute of physics of Czech academy of sciences in Prague. The experimental results and their correspondence to numerical predictions were analyzed by the author of the present thesis.

3.2.1. Superelastic NiTi Notched Thin Ribbon

Straight annealed superelastic NiTi ribbon 0.098 mm thick and 1.178 mm wide were purchased from Memory-Metalle GmbH. A semicircular notch of radius 0.15 mm was electro-discharge machined at one side of 50 mm long NiTi ribbon samples.

Basic room-temperature superelastic deformation behavior of NiTi ribbon was evaluated on notch-free samples using a tensile test until rupture and complete superelastic cycling until fatigue failure while monitoring the evolution of residual strain. Localized cyclic strain evolution around the notch was analyzed by digital image correlation (DIC) during the superelastic cycling of the notched specimen. DIC method employed fine airbrush for random patterning the surface, 5 Mpx Stingray camera, and Ncorr – Open source 2D digital image correlation software.

Further, structural changes in NiTi around the notch were analyzed using synchrotron X-ray micro-diffraction performed during superelastic cycling until fatigue failure. Approximately 5 μm small monochromatic beam at 65 keV (0.18964 Å) was used to scan the area around the notch while Frelon

100x100 mm camera (2048x2048 px with 50 $\mu\text{m}/\text{px}$) was used to detect diffracted x-rays. Python-based Fabio and PyFai libraries were used to full and azimuthal integration of 2D diffractograms. Integrated spectra were then post-process using GSAS II software, particularly using its scripting capability, to evaluate residual martensite phase fractions and elastic strains in austenite in the unloaded sample after a selected number of superelastic cycles. Residual martensite phase fractions were evaluated by Rietveld fit of fully integrated 2D diffractograms. Elastic strains in austenite were evaluated from azimuthally integrated 2D diffractograms as follows. In total 19 1D diffractograms were extracted from individual 2D diffractograms by azimuthal integrations over the range $\pm 5^\circ$ from azimuthal angles ranging from 0 to 180° with 10° increments. Individual 1D diffractograms were then Rietveld fitted by using a scripting tool of GSAS II software considering fixed lattice parameters while allowing for small lattice parameter changes by switching on the HStrain fitting parameter. Thus, azimuthal variations in lattice parameters were obtained and recalculated to strain variations by considering a referential stress-free lattice parameter. Azimuthal strain variations were then fitted by the theoretical periodical function of the azimuthal angle as expected for plane strain state, which resulted in estimates of plane strain tensor components in the laboratory coordinate system.

3.2.2. Shape Memory NiTi Notched Thin Ribbon

The experiments were done on a thin NiTi ribbon. The SMA ribbon was cut into double-edge-notched test specimens using Electrical Discharge Machining (EDM) [236]. The geometry of the test specimens is illustrated in Fig. 6-1a. Deformations on the surface of the NiTi thin ribbon including two-sided semi-circular notches (see Fig. 6-1a) were measured during cyclic thermal actuation under constant tensile force corresponding to 200 MPa of nominal tensile stress in the notch-free cross-section that was applied while the ribbon was kept above A_f temperature through passed electrical current. The thermal actuation was then realized through periodical 10 seconds long electrical pulses followed by 14s of cooling that supervises cyclic thermally induced reverse and forward transformations as exhibited in Fig. 4. 2D strain fields were evaluated by Digital Image Correlation (DIC) method where Basler acA2000 camera was used to record images of the speckle pattern deposited onto the ribbon surface by airbrush. The recorded images were post-processed by the DIC method implemented in RT Mercury software² resulting in spatially resolved 2D strain tensors identified for individual images. Besides, virtual extensometers were used to identify longitudinal and transverse strains within and outside the notch zone to characterize the deformation behavior in those zones.

Note that even though the model used in present simulations does not account for the localized nature of martensitic transformation in thin ribbons as reported in experiments [237,238] or implemented in models [239], the simulation naturally predicts an inhomogeneous course of martensitic transformation that is governed by inhomogeneous distribution of stresses around the notch.

² http://www.sobriety.cz/t_optical_systems_en.htm#software

3.3. Numerical Analysis

3.3.1. Three Dimensional Macroscopic SMA Material Model

To consider the potential conventional plastic deformation at high-stress levels beyond the martensitic transformation plateau at the tip of the notch of the thin NiTi ribbon, a thermo-mechanical SMA model [57] is used which is already implemented in MSC Marc Finite Element program. This model discretizes the total incremental strain into:

$$\Delta \boldsymbol{\varepsilon} = \Delta \boldsymbol{\varepsilon}^{el} + \Delta \boldsymbol{\varepsilon}^{ph} + \Delta \boldsymbol{\varepsilon}^{pl} + \Delta \boldsymbol{\varepsilon}^{th} \quad \text{Eq. 3-1}$$

In which ‘‘El’’, ‘‘Th’’, ‘‘Ph’’ and ‘‘Pl’’ represent Elastic, Thermal, Phase transformation, and Plastic, respectively. The elastic strain ($\Delta \boldsymbol{\varepsilon}^{el}$) is taken to be related to the elastic modulus, \mathbf{L} , and Cauchy stress:

$$\Delta \boldsymbol{\varepsilon}^{el} = \mathbf{L}^{-1} : \boldsymbol{\sigma} \quad \text{Eq. 3-2}$$

The thermal strain is not used in this study and $\Delta \boldsymbol{\varepsilon}^{ph}$ is the phase transformation strain which is composed of trip strain and twin strain as follows:

$$\Delta \boldsymbol{\varepsilon}^{ph} = \Delta \boldsymbol{\varepsilon}^{Trip} + \Delta \boldsymbol{\varepsilon}^{Twin} \quad \text{Eq. 3-3}$$

In which for $\Delta \boldsymbol{\varepsilon}^{Trip}$ it is assumed to be the phase transformation strain, while $\Delta \boldsymbol{\varepsilon}^{Twin}$ is supposed to be related to the reorientation of randomly oriented thermally induced martensite.

$$\Delta \boldsymbol{\varepsilon}^{Trip} = \Delta f^M g(\sigma_{eq}) \boldsymbol{\varepsilon}_{eq}^T \frac{3}{2} \frac{\boldsymbol{\sigma}'}{\sigma_{eq}} + \Delta f^M \boldsymbol{\varepsilon}_v^T \mathbf{I} + \Delta f^A \boldsymbol{\varepsilon}^{ph} \quad \text{Eq. 3-4}$$

In present simulations, the former is taken into account as the simulations are performed in the superelastic regime under iso-thermal loading conditions. Such that, reorientation of thermally induced martensite does not play role in present calculations. In Eq. 3-4, the non-negative parameter Δf^M is the increment at which the martensite is formed, the negative Δf^M parameter represents the increment of formation austenite upon reverse phase transformation ($M \rightarrow A$), and σ_{eq} is equivalent Von Mises stress. $\boldsymbol{\varepsilon}_{eq}^T$ and $\boldsymbol{\varepsilon}_v^T$ are the deviatoric and volumetric parts of transformation strain, respectively. The function $0 \leq g(\sigma_{eq}) \leq 1$ is a measure of the extent to which the martensitic transformation strains are aligned with the deviatoric stress. In Eq. 3-4 the two first terms explain the evolution of transformation strains due to the formation of stress-induced martensite and the last term expresses the recovery of accumulated phase transformation strains.

$$g(\sigma_{eq}) = 1 - \exp \left[a \left(\frac{\sigma_{eq}}{\sigma_0^g} \right)^n \right], a < 0 \quad \text{Eq. 3-5}$$

Which tends to contribute in the goodness of fit to the experimental stress-strain response (Fig. A.1), taking advantage of fitting parameters (g_a - g_f) when is written as follows:

$$g(\sigma_{eq}) = 1 - \exp \left[g_a \left(\frac{\sigma_{eq}}{\sigma_0^g} \right)^{g_b} + g_c \left(\frac{\sigma_{eq}}{\sigma_0^g} \right)^{g_d} + g_e \left(\frac{\sigma_{eq}}{\sigma_0^g} \right)^{g_f} \right] \quad \text{Eq. 3-6}$$

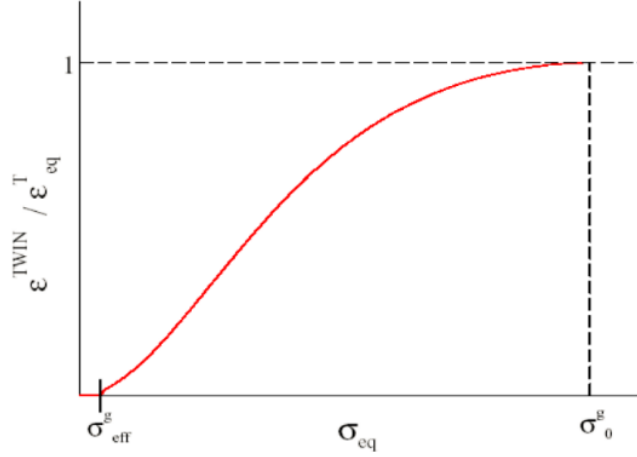


Fig. 3-1 G-function under 100% Martensite

The plastic strain increment of the two-phase aggregate, as well as for every single phase in this model is assumed to be controlled by J_2 flow theory:

$$\Delta \epsilon^{pl} = \Delta \lambda (3/2) \sigma' / \sigma_{eq} \quad \text{Eq. 3-7}$$

In Eq. 3-7, $\Delta \lambda$ is the equivalent plastic strain and it is assumed that for each phase, the increment of equivalent plastic strain is related to the applied stress as:

$$\Delta \lambda^\alpha = \Delta \lambda_0^\alpha \left(\frac{\sigma_{eq}^\alpha}{\sigma_Y^\alpha} \right)^m \quad \text{Eq. 3-8}$$

Where σ_Y^α is the flow stress for the α -th phase. Here, α represents the martensite and austenite phases. The hardening rule in this model comes then into account when the current value of flow stress of the α -th phase (σ_Y^α) is calculated depending on the current increment of the plastic strain of the same phase as:

$$\Delta \sigma_Y^\alpha = h^\alpha \Delta \lambda^\alpha \quad \text{Eq. 3-9}$$

In Eq. 3-9, h^α is the hardening coefficient. With the assumption that $\sigma_Y = \sigma_Y(T, \sigma_{eq})$ and $f = f(T, \sigma_{eq})$ then the final form of Eq. 3-9 can be simplified as:

$$\Delta \sigma_Y = \sigma_Y \left(\left(\frac{1}{\sigma_Y} \cdot \frac{\partial \sigma_Y}{\partial T} \right) \Delta T + \left(\frac{1}{\sigma_Y} \cdot \frac{\partial \sigma_Y}{\partial \sigma_{eq}} \right) \Delta \sigma_{eq} \right) = \sigma_Y (H_T \Delta T + H_q \Delta \sigma_{eq}) \quad \text{Eq. 3-10}$$

Which H_T and H_q may be written using the chain rule, thus:

$$\begin{cases} H_T = \frac{1}{\sigma_Y} \cdot \frac{\partial \sigma_Y}{\partial f} \cdot \frac{\partial f}{\partial T} \\ H_q = \frac{1}{\sigma_Y} \cdot \frac{\partial \sigma_Y}{\partial f} \cdot \frac{\partial f}{\partial \sigma_{eq}} \end{cases} \quad \text{Eq. 3-11}$$

$$\Delta f = \Delta f^M + \Delta f^A = \left(\frac{\partial f}{\partial T} \right) \Delta T + \left(\frac{\partial f}{\partial \sigma_{eq}} \right) \Delta \sigma_{eq} \quad \text{Eq. 3-12}$$

More details on this model can be found in Ref [57].

It should be noted that even though when the material enters the plastic threshold of detwinned martensite, unrecovered strain after load release is a summation of the plastic strain of detwinned martensite and the part attributed to residual transformation strain (residual martensite volume fraction)[161]; however, in the present model (as was described in the previous section) the latter is not considered and the unrecovered strain in the unloaded state is affiliated to the plastic deformation of detwinned martensite. For a better illustration of this point, a simple tensile simulation on a smooth ribbon (with same material parameters as Table 3-1) is conducted and its resultant stress-strain response and the corresponding evolution of martensite volume fraction is plotted in Fig. 3-2 using the present model [57]. As it is seen, the residual unrecovered strain after unloading (Fig. 3-2a) is just due to permanent plastic deformation of martensite, and the contribution of remnant martensite is not involved as there is not any volume fraction of (retained) martensite in the unloaded state (Fig. 3-2b).

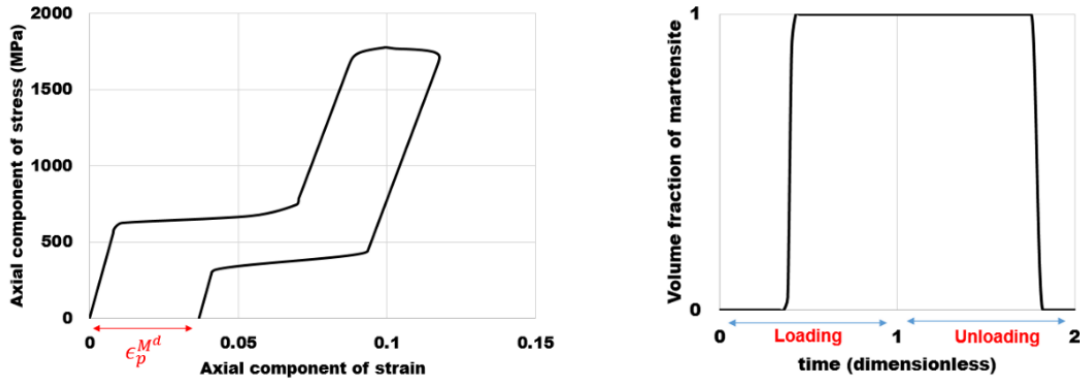


Fig. 3-2 Iso-thermal tensile-unloading behavior of superelastic NiTi, predicted by the present model; a) stress-strain response, b) corresponding time-martensite volume fraction response

Table 3-1 list of abbreviations

$\Delta f^{M \geq 0}$	increment at which martensite is formed	σ_{eq}	effective stress defined with Von-Mises yield function as: $\sigma_{eq} = \sqrt{\frac{3}{2} \sigma' : \sigma}$
ϵ_{eq}^T	Deviatoric part of the transformation in uniaxial tension	I	identity tensor
ϵ_v^T	volumetric part of the transformation strain	$\Delta \lambda$	Equivalent plastic strain inc: $\Delta \lambda = \sqrt{\frac{2}{3} \Delta \epsilon^{pl} : \Delta \epsilon^{pl}}$
h^α	Hardening coefficient		

3.3.2. The Experimentally derived material parameters

The material parameters required as inputs for the present model consist of elastic modulus of the martensite and austenite (E_M, E_A), forward/reverse transformation start and finish temperatures at zero stress ($M_S, M_f/A_S, A_f$), transformation strain ϵ^{tr} , deviatoric transformation strain (ϵ_{dev}^{tr}), temperature dependencies of transformation stresses for the forward and reverse transformation (C_M, C_A), and the

yield stress of austenite and martensite phases (σ_y^A , σ_y^M), and the yield stress of martensite, which were assessed by experiments.

▪ **Superelastic Material**

To obtain the material parameters, a set of iso-thermal tensile tests are performed on the defectless superelastic NiTi ribbons in austenite state at the temperature range from -20°C to 40°C. The extracted parameters are presented in table Table 3-2. Fig. 3-3 illustrates the correspondence between the finite element results (using the fitted parameters) of one tensile loading cycle to those obtained from experiments.

Table 3-2 Material's parameters for the superelastic NiTi ribbons

Parameter	E_A (GPa)	E_M (GPa)	C_A (MPa/°C)	σ_y^M (MPa)
Value	70	52	8.66	1800
Parameter	M_s (°C)	M_f (°C)	C_M (MPa/°C)	σ_y^A (MPa)
Value	-74	-88.8	6.66	∞
Parameter	A_s (°C)	A_f (°C)	ϑ	ϵ^{tr} (dev)
Value	-30.9	-15	0.33	5.5%

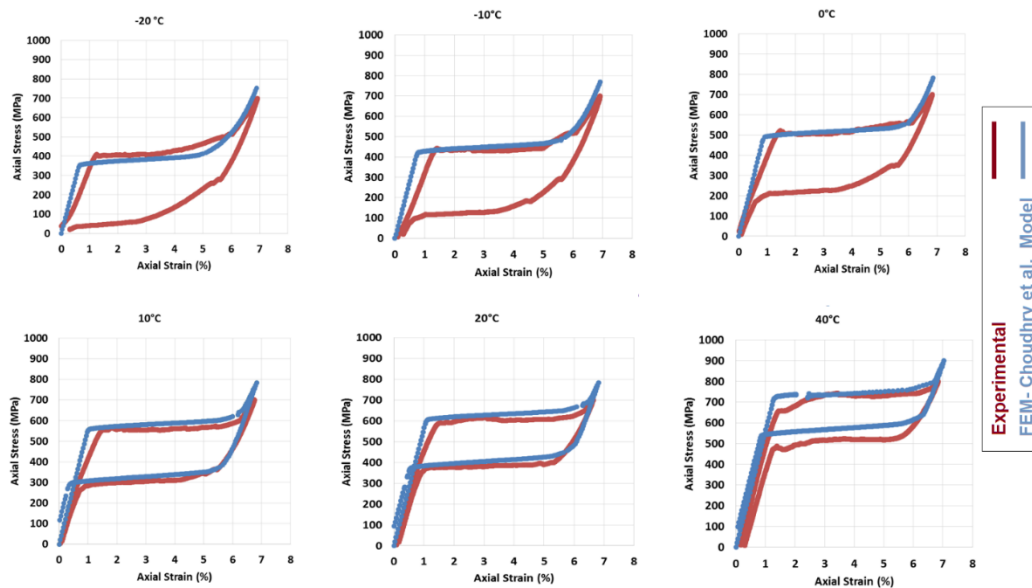


Fig. 3-3 the representation of the agreement between experimental 1D response and those obtained using Choudhry's model by fitting parameters

▪ **Shape Memory Material**

To obtain the material parameters, thermal cycling tests were performed under different levels of external stress. To this aim, the material is pre-loaded in austenite state (at a temperature above the A_f), and the cooling-heating thermal cycles are applied while keeping the stress constant, ranging from 100MPa to 300MPa. Besides, a monotonic tensile test is performed on the material in martensite state at a temperature below the M_f , to obtain the reorientation stress, as well as the yield point of detwinned martensite.

Table 3-3 Material parameters for the shape memory NiTi ribbons

Parameter	E_A (GPa)	E_M (GPa)	ϑ	A_s ($^{\circ}$ C)	C_A (MPa/ $^{\circ}$ C)	σ_y^M (MPa)
Value	70	52	0.33	51	8.6	1270
Parameter	M_s ($^{\circ}$ C)	M_f ($^{\circ}$ C)	ε_{dev}^{tr}	A_f ($^{\circ}$ C)	C_M (MPa/ $^{\circ}$ C)	σ_y^A (MPa)
Value	31.5	19	0.055	62.5	8.6	∞

The extracted parameters are presented in Table 3-3. Fig. 3-4 illustrates the correspondence between the finite element results to those obtained from experiments.

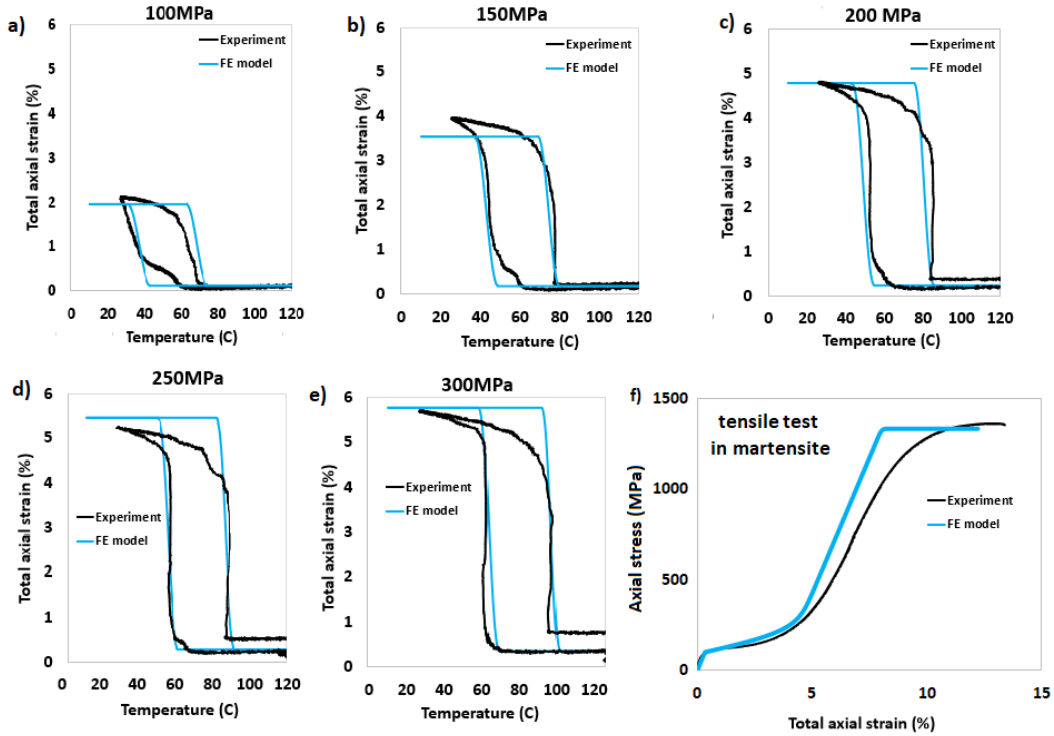


Fig. 3-4 Verification of the material properties obtained from experiments on a virgin defectless ribbon. The black curves represent the experimental results and the blue curves show the FE results

CHAPTER 4. Superelastic notched NiTi ribbon: the effects of martensitic transformation and plasticity on the cyclic evolutions of mechanical gradients

4.1. Introduction

In this chapter, the effect of martensitic transformation (MT) and plastic deformation on the local superelastic cyclic response of NiTi in the vicinity of a semicircular notch in a thin NiTi ribbon are analyzed, both experimentally and numerically. In experiments, digital image correlations and X-ray microdiffraction are used to analyze the cyclic evolution of local strains and presence of remnant martensite at the root of the notch (see explanations in 3.2.1). The finite element simulations are performed to thoroughly analyze the corresponding global and local evolutions of stress-strain-volume fraction (ξ)-temperature responses. While in experiments the tension-unloading cycles are conducted till fracture, due to the computational costs only 9 cycles are analyzed in numerical simulations.

4.2. Numerical Simulations Method

The role of MT on the cyclic evolutions of the local and global mechanical fields is analyzed in a superelastic thin notched NiTi ribbon. Then, the effects of the plasticity occurring at the notch-tip zone, where the maximum stresses are expected, on the reversibility of MT and the local redistribution of stresses and strains are investigated. The simulations are based on the experimental protocol and findings.

Three-dimensional force-controlled FEM simulations of iso-thermal cyclic tension-unloading were carried out (as it was done in the experimental part) on a thin shape memory 1.067 mm wide and 0.1 mm thick NiTi ribbon including single-edge semi-circular notch (Fig. 4-1a) with the reference notch radius as equal to $R_0=0.177$ mm, in which the maximum applied tensile force induces 745 MPa of macroscopic axial stress, which turns in completion of the martensitic transformation within the whole structure in loading stage. To study the role of the notch's radii, elastic module mismatch –between austenite and martensite–, and the maximum phase transformation strain (ε^{tr}) on the notch-tip stress/strain fields, additional parametric 2D analyses of the first loading stage are done, applying the maximum macroscopic axial stress of 1300 MPa. Six different notch radii ranging from $R_0=0.177$ to $R=34R_0=6.018$ mm were examined while considering an equal penetration of 0.144mm at the edge of the ribbon (thus, keeping the notch-cross section constant) as depicted in Fig. 4-1a-b. Also, four transformation strain values were tested as $\varepsilon^{tr} = 0\%$, 1%, 3% and 5.5% for the reference notch radius R_0 . Fig. 4-2 represents a chart of the survey to investigate the effects of the geometric and material parameters. In numerical simulations, a three-dimensional SMA constitutive thermomechanical model proposed by Choudhry and Yoon [57] and implemented in MSC Marc finite element package is used. Since this model allows us to combine SMA behavior with the plasticity of both the phases, we studied both cases of an *ideal-SMA* (neglecting the plasticity) and the case in which the plasticity occurs in detwinned martensite beyond the transformation stress-plateau (*plastic-SMA*). Further, the response of an additional reference material, *elastic-plastic austenite*, is compared to the responses of the *ideal-SMA* and *plastic-SMA* materials.

Plastic-SMA, *ideal-SMA*, and *elastic-plastic austenite* material behaviors are achieved in simulations by:

- *plastic-SMA*: the yield stress of the martensite and austenite are set to 1800 MPa and infinite, respectively (Fig. 4-1e).
- *ideal-SMA*: the plasticity was not activated in material options (Fig. 4-1e)
- *elastic-plastic austenite* (no phase transformation is incorporated): all transformation temperatures (M_S , M_f/A_S , A_f) are set to very low values and the yield stress of the austenite and martensite are set to 1800 MPa and infinite, respectively; such that, the austenite would plastically deform at high-stress levels without undergoing phase transformation upon loading (Fig. 4-1e)

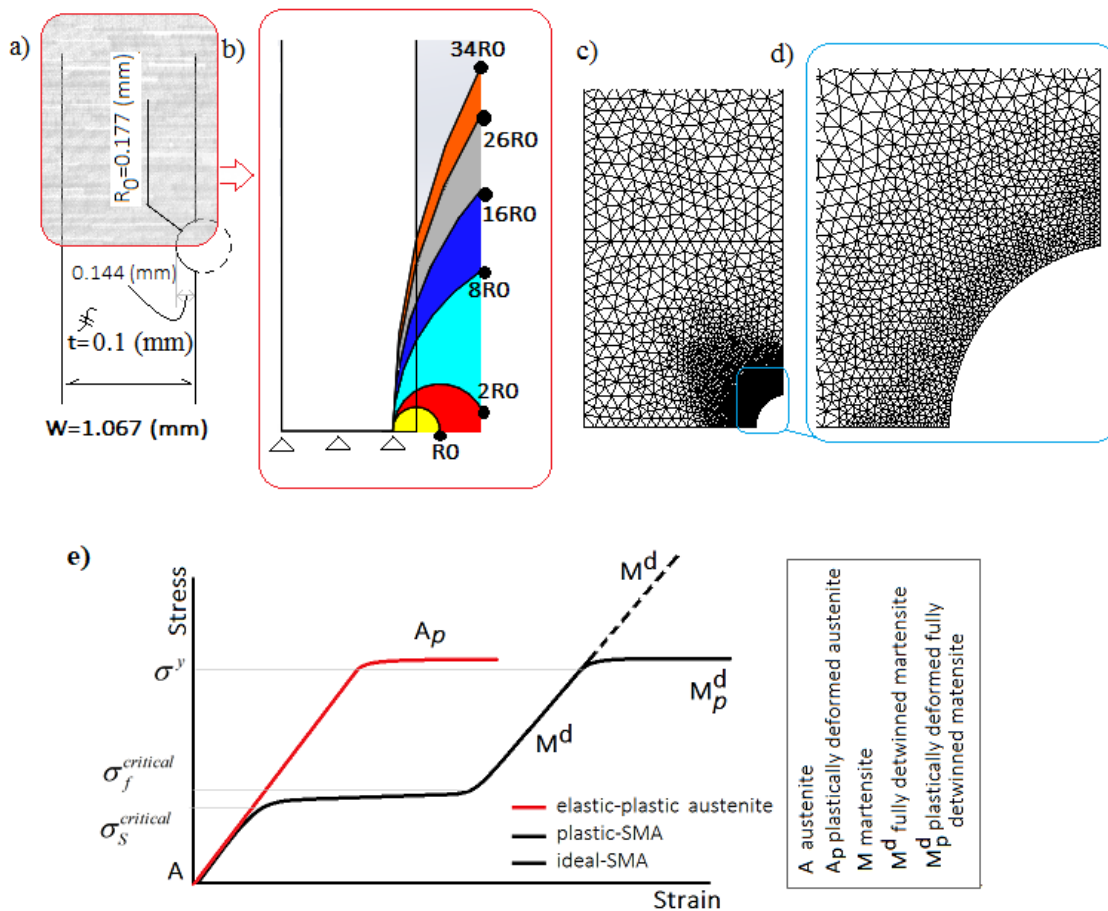


Fig. 4-1 a) the reference FEM model configuration, b) half of the notched ribbon modeled with different notch radii, due to symmetry, c) meshed model, d) mesh refinement at the notch-tip area, e) Schematic representation of the stress-strain responses of the studied material case studies

All simulations in this study are carried out at 23°C similar to the room temperature in experiments. Taking advantage of symmetry, half of the specimens are considered in simulations (Fig. 4-1b). The 3D models are discretized using element 136³ which is a full integration three-dimensional, six-node first order isoparametric arbitrarily distorted pentahedral element (Fig. 4-1c). The 2D models meshed

³ MSC Marc 2017, Documentation, Vol B: Element Library

with element 201⁴ which is a three-node, isoparametric, triangular element written for plane stress applications. The mesh was refined in the zone of expected high-stress gradients i.e. at the zone of notch-tip and its surroundings as illustrated in Fig. 4-1d. Full Newton-Raphson iterative procedure is used in FE solutions under a large strain analysis method.

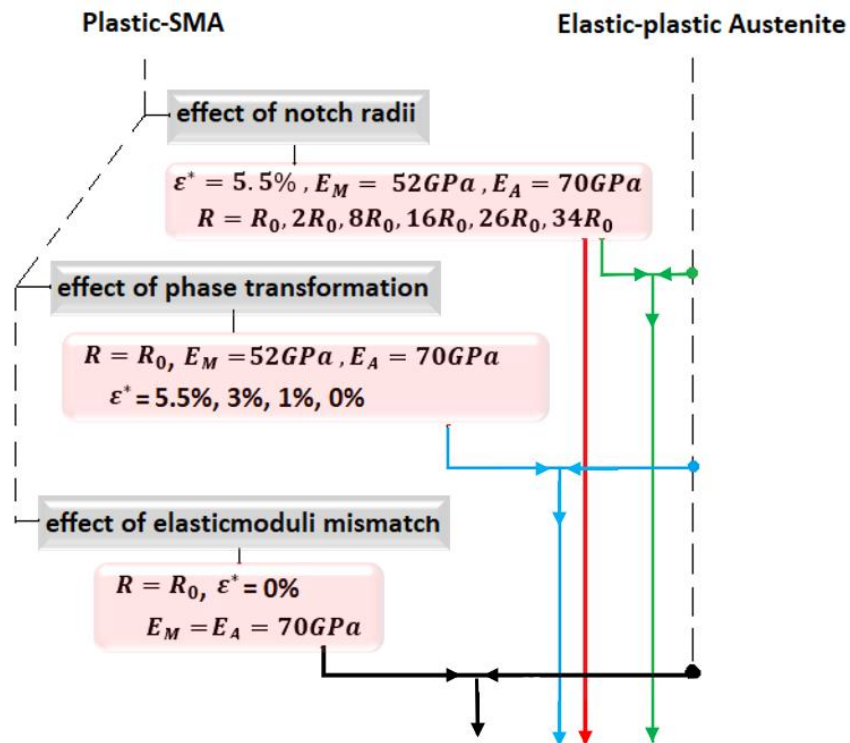


Fig. 4-2 Diagram of the performed simulations on the plastic-SMA case and their comparison with the reference elastic-plastic austenite case-study

4.3. Results and Discussion σ

4.3.1. Ideal_SMA, First Loading Stage: comparison between FE and experimental DIC results

The local stress gradient around the notch-tip evolves along with martensitic transformation spreading into the surrounding bulk. Correspondingly, the evolution of the stress at the notch-tip during incremental application of macroscopic load can be divided into four distinct stages that will be described hereinafter in stress-strain and stress-time spaces (Fig. 4-3a to Fig. 4-3d), where the important loading path turning points are denoted (points 0 to 6). The evolution of the axial component of strain in turning points 0 to 6, obtained from the DIC measurements is exhibited through the colormaps in Fig. 4-3. The associated FE colormaps of the total axial strain and volume fraction of martensite are indicated through Fig. 4-3f and Fig. 4-3g, respectively. In particular, martensite volume fraction (VFM, ξ) distributions shown in Fig. 4-3g0 to Fig. 4-3g6, were converted into simplified colormaps in Fig. 4-3h0 to Fig. 4-3h6, splitting the total transforming sample volume into three fractions according to the degree of martensite straining, i.e., detwinning. Here, the degree of martensite detwinning is supposed to be contrarily proportional to the austenite volume fraction,

⁴ MSC Marc 2017, Documentation, Vol B: Element Library

restraining the martensite from full detwinning. The three fractions are consecutively: i) near-complete austenite ($\xi \leq 0.2$), where the martensite is thought to be extremely constrained by the austenite; ii) partially detwinned martensite ($0.2 < \xi < 0.9$), where the austenite is still substantially restraining the martensite from full detwinning; iii) nearly complete martensite ($\xi \geq 0.9$), where it is almost free to fully detwin [214].

The evolution of the stress at the notch-tip is non-monotonous during the iso-thermal loading, which is due to the spatially heterogeneous course of martensitic transformation starting at higher stress zones around the notch-tip and its extending towards the bulk upon further loading. Fig. 4-3d represents the interaction between the stress evolution at the notch-tip and bulk, upon incremental macroscopic (displacement controlled) loading in four stages:

- *Stage 1: local martensitic transformation nucleation, path 0_1*

Due to the stress concentration effect of the notch, the martensitic transformation nucleates at the notch-tip while the bulk is still in elastic austenite (path 0_1 in Fig. 4-3d, also see path 0_1 in Fig. 4-3a to Fig. 4-3c). In path 0_1 the notch-tip and its very close distance are following the stress-strain response of SMAs characterized by stress plateau. The martensitic transformation at the notch-tip finishes at point 1 where the bulk remains in elastic austenite. The volume fractions of martensite at points 0-1 are illustrated via the colormaps in Fig. 4-3g0-g1 and Fig. 4-3h0-h1.

- *Stage 2: martensitic transformation spreading towards the bulk, path 1-2-3*

Since the notch-tip and its very vicinity have completed the martensitic transformation (point 1 in Fig. 4-3c-d and Fig. 4-3e1-f1-g1-h1), it can be regarded as a martensitic elastic inclusion in an austenite matrix that is being transformed within a shear-band propagating from the notch-tip, upon the continuation of macroscopic loading. The shear-band extends from the notch-tip along a diagonal direction, so-called MT-band hereafter (see path 1-2-3 in colormaps shown in Fig. 4-3e to Fig. 4-3h). The transformation strain induced in MT-band has to be accommodated by elastic deformation of martensite within the adjacent zone of fully transformed notch-tip; which indeed, turns in a sharp stress amplification at the notch-tip while the MT-band is propagating throughout the whole cross-section (path 1-2-3 in Fig. 4-3c and Fig. 4-3d).

It is important to note that, this sharp stress increase of detwinned martensite at the notch-tip in this stage, is because the transformation strain is a finite value in SMAs, which indeed allows the elastic response of detwinned martensite to arise after the forward transformation ($A \rightarrow M$) is completed at the notch-tip.

- *Stage 3: martensitic transformation at the bulk, path 3-4-5-6*

Since the MT-band is extended through the whole specimen's cross-section at point 3 (see Fig. 4-3g3 and Fig. 4-3h3) the macroscopic stress plateau appears. Then, proceeding of the martensitic transformation at the bulk in relatively constant stress (path 3-4-5-6, the black curve in Fig. 4-3d) prohibits the stress at the notch-tip to further sharp increase (path 3-4-5-6, the red curve in Fig. 4-3d). Simultaneously with the martensitic transformation completion at the bulk, the fully detwinned martensite inclusion propagates towards the MT-band direction and spans over the entire cross-section (path 3-4-5-6 in Fig. 4-3g and Fig. 4-3h).

- Stage 4: the elastic response of detwinned martensite both at notch-tip and bulk

At point 6 which the martensitic transformation at the macroscopic scale (bulk) is completed and the fully detwinned martensite is extended to the whole cross-section along the MT-band, higher external load results in elastic response of detwinned martensite at both local and global scales.

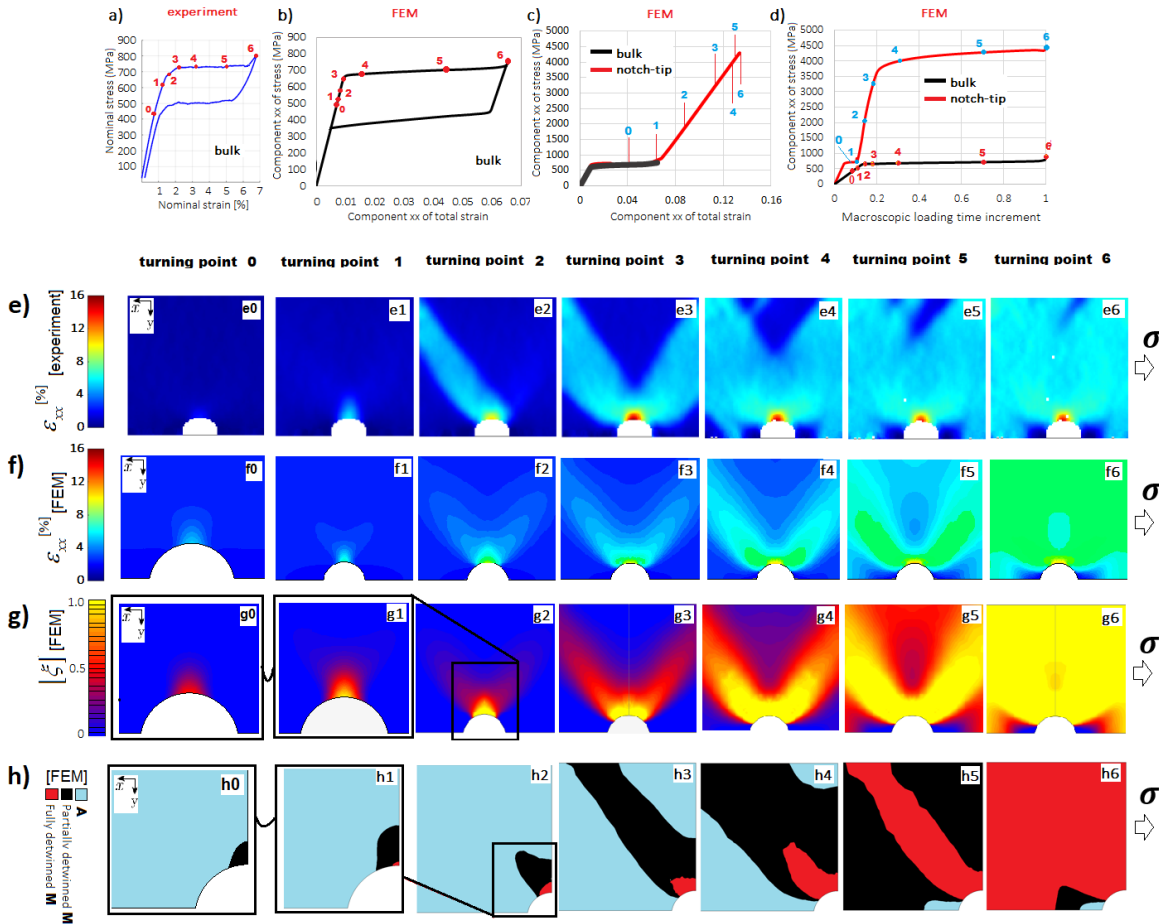


Fig. 4-3 Comparison between the DIC results and the simulation of the ideal-SMA; (a & b) bulk stress-strain responses from experiment and FEM; (c) notch-tip stress-strain response from FEM, d) interaction between the bulk and notch-tip stress upon the incremental application of the macroscopic load; (e1-e6) DIC results: evolution of the local axial strain regarding the points 1-6 denoted in Fig. 4-3a; (f1-f6) FEM results: evolution of the local axial strain regarding the points 1-6 denoted in Fig. 4-3a to Fig. 4-3d; (g1-g6 & h1-h6) FEM results: evolution of the volume fraction of martensite (forward transformation) regarding the points 1-6 denoted in Fig. 4-3a to Fig. 4-3d

Since in simulations regarding the ideal-SMA case study discussed in this section, the plasticity is not involved in the decomposition of total strain, thus, the phenomena in loading which were explained above, are fully reversible upon unloading. In reality, however, the stress at the root of the notch cannot reach such high values (~ 4.5 GPa) in martensite; since the plastic strains evolve once the stress at the notch-tip reaches the martensitic yield point. The next section, analyses the more realistic local responses, i.e. in the presence of plastic deformations.

4.3.2. Plastic_SMA, First Loading Stage: comparison between FE and experimental DIC results

To understand how excluding the plasticity in the analysis of the local martensitic transformation and deformation mechanisms would introduce significant inaccuracies, the above-explained reference ideal-SMA case-study is compared to the simulation results, in which the plasticity is considered in simulations (plastic-SMA), as it is represented in Fig. 4-4. Fig. 4-4a-d summarizes the interactions between the notch-tip and bulk responses through the stress-strain-volume fraction (ξ)-temperature diagrams of a single global loading-unloading cycle, where the important turning points are depicted as points 0-11.

Fig. 4-4e and Fig. 4-4f represent the colormaps of total axial strain obtained from DIC and FE, respectively, at turning points 0 to 6 in loading, and Fig. 4-4g illustrates their corresponding martensite volume fraction distributions which were converted into simplified colormaps in Fig. 4-4f splitting the total transforming sample volume into three fractions according to the degree of martensite straining, i.e., detwinning. Here the degree of martensite detwinning is assumed to be inversely proportional to the austenite volume fraction, restraining the martensite from full detwinning. The three fractions are consecutively i) near-complete austenite ($\xi \leq 0.2$), where the martensite is thought to be highly constrained by the austenite; ii) partially detwinned martensite ($0.2 < \xi$). The colormaps concerning the volume fraction of martensite (and their simplified colormaps) are also represented for unloading (turning points 7 to 11 in Fig. 4-4g and Fig. 4-4h, respectively).

▪ **Loading**

- *Stage 1: local martensitic transformation nucleation, path 0_1*

The phenomena upon path 0-1 are similar to that explained in stage 1 of the elastic-SMA case study discussed in 4.3.1.

- *Stage 2: martensitic transformation spreading towards the bulk, path 1-2-3*

Since the notch-tip and its very vicinity have completed the martensitic transformation (point 1 in Fig. 4-4c-d and Fig. 4-4e1-f1-g1-h1), it can be regarded as a martensitic elastic inclusion in an austenite matrix that is being transformed within a shear-band propagating from the notch-tip, upon the continuation of macroscopic loading. The shear-band extends from the notch-tip along with the MT-band (see path 1-2-3 in colormaps of Fig. 4-4e to Fig. 4-4h). The transformation strain induced in MT-band has to be accommodated by deformation of martensite within the adjacent zone of fully transformed notch-tip, in two distinct stages:

- ✓ *Stage2_a: path 1-2*

Upon path 1-2 the transformation strain induced within the MT-band is being accommodated by elastic deformations of fully detwinned martensite inclusion at the notch-tip. Thus, the stress at the notch-tip sharply increases (path 1-2 in Fig. 4-4).

- ✓ *Stage 2_b: path 2-3*

Upon path 2-3 the martensitic transformation is still being expanded over the whole cross-section along the MT-band. However, since at point 2 the notch-tip stress reached the martensitic yield point, the transformation strains evolving along the MT-band in path 2-3 would be accommodated by plastic deformation of plastically deformed fully detwinned martensite inclusion at the notch-tip. The

plastically deformed zone at the notch-tip is shown in Fig. 4-4h3 in yellow color. Plastic deformation of martensite at the notch-tip evolving in this sub-stage turns into reduced effective stress and higher values of total axial strain at the notch-tip, with respect to the ideal-SMA (path 2-3 in Fig. 4-4c-d and Fig. 4-4f-h).

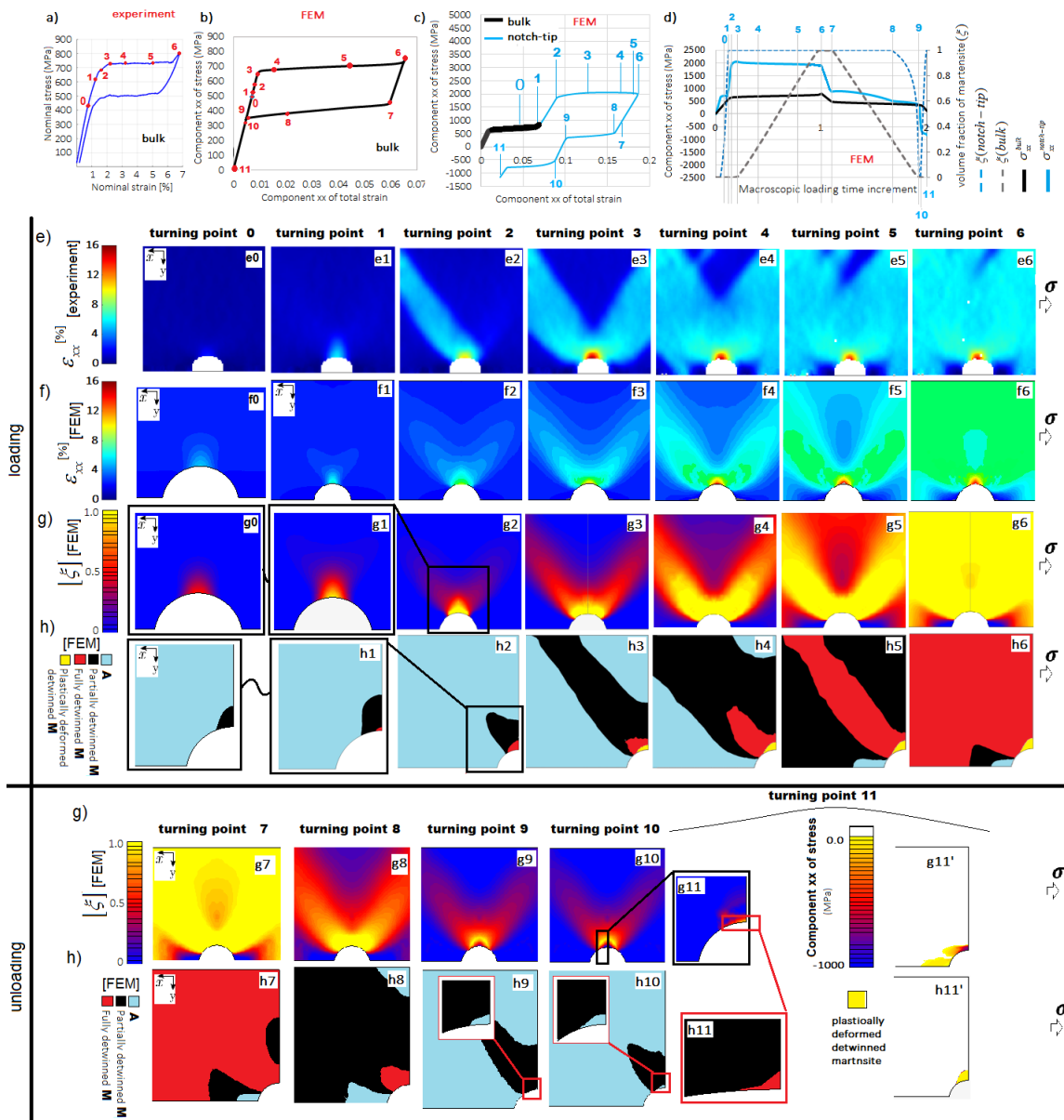


Fig. 4-4 Comparison between the DIC results and the simulation of the plastic-SMA, (a & b) bulk stress-strain responses from experiment and FEM; (c) notch-tip stress-strain response from FEM; (d) interaction between the bulk and notch-tip stress upon incremental macroscopic loading-unloading in a single cycle; (e1-e6) DIC results: evolution of the local axial strain regarding the points 1-6 denoted in Fig. 4-4a; (f1-f6) FEM results: evolution of the local axial strain regarding the points 1-6 denoted in Fig. 4-4a to Fig. 4-4d; (g1-g6 & h1-h6) FEM results: evolution of the volume fraction of martensite (forward transformation) regarding the points 1-6 denoted in fig. 4a to 4d; (g7-g11 & h7-h11) FEM results: evolution of the volume fraction of martensite (reverse transformation upon macroscopic unloading) regarding the points 7-11 denoted in Fig. 4-4b to Fig. 4-4d; (g11') local compressive axial stress at the end of macroscopic unloading (point 11); (h11') plastic zone at the end of unloading (point 11)

- *Stage 3: Superimposition of two effects: plasticity at the notch-tip and martensitic transformation at bulk, path 3-4-5-6*

Since the MT-band is spanned through the whole cross-section, the stress plateau appears in the macroscopic stress-strain response. Proceeding of the martensitic transformation in bulk at relatively constant stress, by itself, prohibits the sharp stress increase at the notch-tip. This effect, is superimposed with the yield of martensite at the notch-tip, which results in a stress relaxation at the notch-tip (see path 3-4-5-6 in Fig. 4-4d).

- *Stage 4: the elastic response of the bulk beyond the transformation stress plateau*

Loading the bulk above the stress plateau results in elastic deformation of detwinned martensite which results in stress at the notch-tip to increase till it re-reaches the yield stress; after which, further loading in elastic detwinned martensite at the macroscopic level (bulk), turns into further plastic strains at the notch-tip in constant stress.

▪ **UNLOADING**

Since irreversible strains remain at the notch-tip and its very close vicinity, during loading, upon unloading –where the reverse $M \rightarrow A$ phase transformation proceeds at the whole structure– the elastic ligament tends to return to its original configuration which induces compressive stresses on the permanently deformed notch-tip area. Whenever the value of the compressive stresses exceeds the forward plateau stress in compression⁵, it would turn into a secondary (compression-induced) forward phase transformation at the notch-tip in the unloading stage. Consequently, the phenomena upon unloading can be explained as follows:

- *Stage U_1 : elastic unloading at the bulk, path 6-7*

At the end of loading in point 6, the whole structure is in detwinned martensite. Macroscopic unloading upon path 6-7 causes the elastic response in the bulk level, i.e. elastic stress relaxation to the onset of the reverse plateau stress (see the black curve in Fig. 4-4d) which turns in a sharp stress-release at the notch-tip due to stress concentration concept (see blue curve in Fig. 4-4d).

- *Stage U_2 : reverse phase transformation at the bulk, path 7-8-9*

The reverse martensitic transformation initiates and proceeds at the bulk (path 7-8-9, dashed-black curve in Fig. 4-4d) –accompanied by macroscopic stress plateau (path 7-8-9, black curves in Fig. 4-4d)–, which extends towards the notch-tip along with the MT-band upon further unloading (see colormaps in Fig. 4-4g7-g8-g9 and their simplified colormaps in Fig. 4-4h7-h8). The reverse martensitic transformation in MT-band results in the recovery of transformation strains along with the MT-band. Recovery of transformation strains in MT-band turns in further elastic unloading of detwinned martensite at the notch-tip (see path 7-8, the blue curves in Fig. 4-4c,d). The reverse stress plateau is reached at the notch-tip at point 8, thus, the material at both the notch-tip and at the bulk completes the $M \rightarrow A$ transformation at point 9 (see colormaps in Fig. 4-4g9,h9). Interestingly, at point 9 the levels of stresses reached at the notch-tip induce the completion of reverse martensitic

⁵ Note: due to the model limitations, the tension-compression asymmetry is not considered in present simulations; thus, the forward/reverse plateau stresses in compression are equal to those under tension.

transformation at the notch-tip; however, the transformation strains are not yet wholly recovered at the MT-band at point 9 (see the colormaps in Fig. 4-4g9,h9). It means that at point 9 the austenite inclusion at the notch-tip is surrounded by a partially detwinned MT-band, where the rest of the transformation strains will recover upon further unloading in path 9-10-11 in the next stage.

- *Stage U₃: wholly recovery of transformation strains at MT-band, inducing compressive stresses at the plastically deformed notch-tip area, path 9-10-11*

Upon path 9-10-11, further external unloading releases the rest of the transformation strains from the MT-band (see Fig. 4-4g9-g11 and Fig. 4-4h9-h11), i.e. completion of reverse transformation at the entire structure. Since the entire structure completes the reverse transformation during unloading, the elastically transformed ligament tends to return to its original configuration which induced compressive stresses at the permanently plastically deformed zone at the notch-tip (and its very close vicinity). The compressive stress at the notch-tip exceeds the forward transformation stress plateau, which turns into the (compression-induced) forward A→M transformation at the notch-tip (path 10-11, dashed blue curve in Fig. 4-4d, also see colormaps of Fig. 4-4g11,h11). Fig. 4-4g11' represents the compressive stresses at the notch-tip area at the end of unloading, and Fig. 4-4h11' illustrates the plastic zone at the notch-tip. As it is seen the size of the plastic zone is not change upon unloading, since the induced compressive stresses at the notch-tip during the unloading have not reached the martensitic yield stress (compare Fig. 4-4h11' and Fig. 4-4h6).

In essence, the plastic deformation of detwinned martensite results in a double-stage phase transformation at the notch-tip during unloading. Such that, at the end of the unloading stage, a very local remnant martensite inclusion is seen at the notch-tip (Fig. 4-4h11). Further, after the first cycle, upon per loading/unloading stage, the notch-tip and its very close vicinity undergo a double-stage phase transformation ($M^d \rightarrow A \rightarrow M^d$ in loading, and vice versa upon unloading). This is further discussed in section 4.3.3.

▪ *Effects of notch radii*

A single macroscopic loading to 1300 MPa is applied to study the effect of the notch radii on notch-tip stress while considering plasticity (*plastic-SMA*). Several notch radii are examined, ranging from R_0 to $34R_0$ while considering an equal penetration of 0.144mm at the edge of the ribbon (to keep the notch-cross section constant) as depicted in Fig. 4-1a and Fig. 4-1b. Results reveal that for the sharper notches (R_0 & $2R_0$) the phenomena explained in the previous section, regarding the loading stages of plastic-SMA case-study, hold (Fig. 4-5). By increasing the notch radius ($R > 2R_0$), the stress concentration effect of the notch reduces and:

- ✓ due to a lower stress gradient between the bulk and the notch-tip, transformation at the notch-tip completes at higher external loads, i.e. at the early stages of martensitic transformation in bulk (see point 1 in curves for $8r_0$ - $36R_0$ in Fig. 4-5).
- ✓ before the notch-tip stress reaches the yield point, proceeding of martensitic transformation at bulk relaxes the notch-tip stress from the sharp increase before it reaches to yield stress. Once the bulk martensitic transformation is completed (point 6 in Fig. 4-5), the elastic response of detwinned martensite at the bulk results in the notch-tip stress to re-increase sharply till it reaches the martensitic yield stress and plastic deformations at the notch-tip evolve.

In conclusion, at higher stress concentration effects (smaller notch radii), the notch-tip plasticity occurs earlier than the martensitic transformation at the bulk (see point 1 for the curves of R_0 and $2R_0$ in Fig. 4-5); thus, the transformation strains induced within the MT-band is partly accommodated by plastic deformations of the plastically-deformed-martensite at the notch-tip (refer to stage 2_b of the plastic-SMA in section 4.3.2). Therefore, the sharper the notch, the higher plastic strains develop at the notch-tip, as it is also represented in stress-strain diagrams in Fig. 4-6.

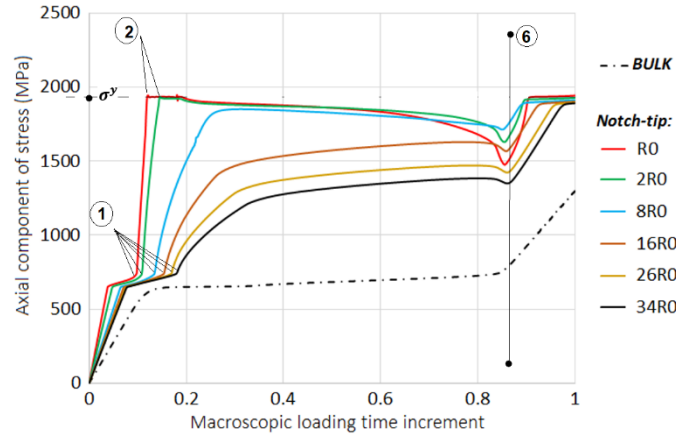


Fig. 4-5 FEM results: interaction between the evolution of the axial component of stress at the notch-tip and the bulk upon incremental macroscopic loading for several examined notch radii

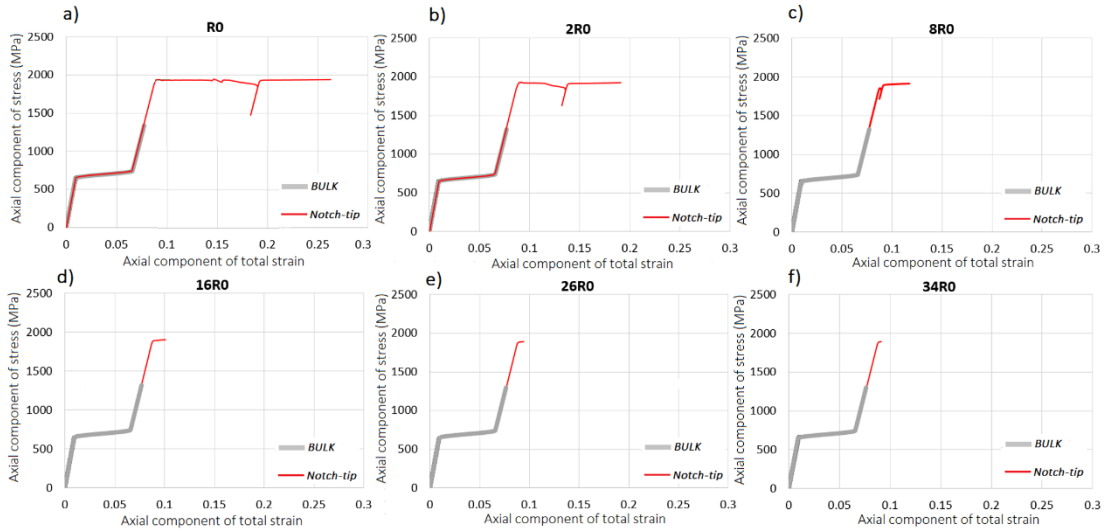


Fig. 4-6 Elastic-plastic austenite (no phase transforming) vs plastic-SMA for different notch radii ranging from R_0 to $34R_0$: comparison between the evolutions of the axial component of strain at the notch-tip upon equal macroscopic loading

▪ *Effect of transformation strain (ϵ^{tr}) and elastic modulus mismatch*

Fig. 4-7 displays a comparison of the notch-tip stress-strain response for:

- case q^I : Elastic-plastic-austenite (no phase transformation), $E = E_A = 70 \text{ GPa}$
- case q^{II} , plastic-SMA, $E_M = E_A = 70 \text{ GPa}$, $\epsilon^{tr} = 0\%$,
- case q^{III} , plastic-SMA, $E_A = 70 \text{ GPa}$, $E_M = 52 \text{ GPa}$; $\epsilon^{tr} = 0\%$
- case q^{IV} , plastic-SMA, $E_A = 70 \text{ GPa}$, $E_M = 52 \text{ GPa}$, ϵ^{tr} ranging from 0% to 5.5%

As it is expected the stress-strain response of the q^I and q^{II} are identical, which is showed in Fig. 4-7a (compare the red and the thick-blue curves). To find out the effects of the elastic moduli mismatch, the response of the q^{II} is compared to q^{III} . Since the E_M is lower than E_A , the elastic moduli mismatch results in higher induced total strains at both notch-tip and at the bulk (compare yellow and the thick-blue curves in Fig. 4-7a). The effect of the transformation strain can be achieved by comparing q^{III} and q^{IV} , where it is seen that the total strain and plastic strain gradually increase by increasing the ε^{tr} (compare the yellow, thick-gray, thin-dashed-red and thin-blue curves in Fig. 4-7a) in an almost linear manner (see Fig. 4-7b).

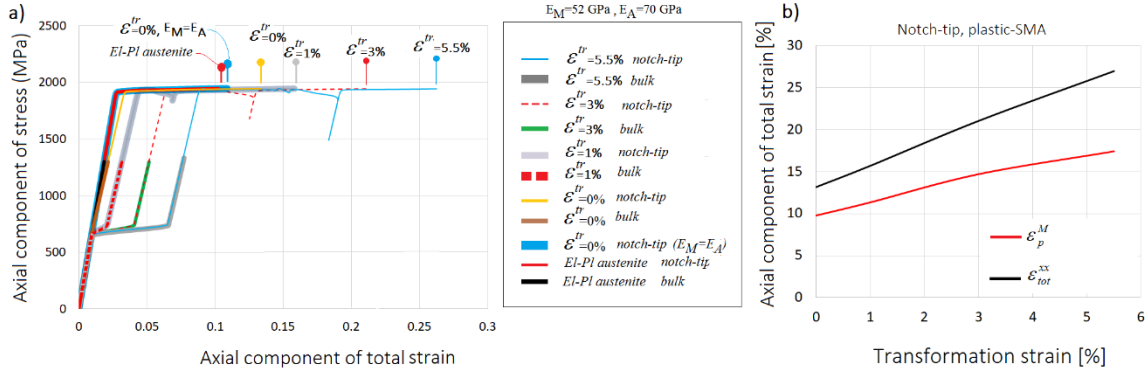


Fig. 4-7 FEM results, the effect of elastic modulus mismatch and the transformation strain on the notch-tip strain, a) comparison between elastic-plastic-austenite and plastic-SMA with different transformation strain values, b) the curve indicates the relation between the transformation strain and the notch-tip strains

4.3.3. Cyclic Response

- *Experimental evaluation of the tensile behavior of the material*

Monotonic and cyclic tensile tests until rupture are performed at room temperature on both smooth and notched samples. The cyclic response of the smooth NiTi ribbon in Fig. 4-8a shows superelasticity with small accumulated unrecovered strains which gradually increase over the cycles till it saturates to $\sim 0.6\%$ after a few hundreds of cycles (see Fig. 4-8b). Note that this accumulation of unrecovered strain in cyclic loading conditions, while the stresses are below the yield points of both phases, represents the transformation induced plasticity (TRIP) [33–36], which is not considered in analyses in the present thesis. The monotonic rupture was observed at $\sim 11.7\%$ of axial strain (Fig. 4-8a) which is well-known to occur by strain localization in necks [240]. Relatively similar behavior is seen in the notched ribbon (Fig. 4-8c-d).

- *Local cyclic responses*

The temperature-stress phase diagram of SMAs as explained in CHAPTER 1, is commonly used to predict the variation of the martensite volume fraction (ξ) (see Fig. 4-9b). In Fig. 4-9b, M_s and M_f are the initial and final temperatures of the forward $A \rightarrow M$ martensitic transformation, and A_s and A_f are the initial and final temperatures of reverse $M \rightarrow A$ transformation. σ_f^{Cr+} and σ_s^{Cr+} express the critical transformation stresses under tension when $T < M_s$, while σ_f^{Cr-} and σ_s^{Cr-} represent the critical transformation stresses in compression. C_M^+ and C_A^+ are the slopes, respectively, of the transformation bands within the phase diagram, for the forward and reverse martensitic transformations under tension, and C_A^- and C_M^- are the corresponding slopes under compression [241]. In reality, the tensile

parameter and the corresponding compressive parameters are most likely different [242]. However, Marc model (used in the numerical part of the present study) does not consider the tension-compression asymmetry. It means that in the simulation results presented hereinafter, for instance, $C_{M,A}^+ = C_{M,A}^-$.

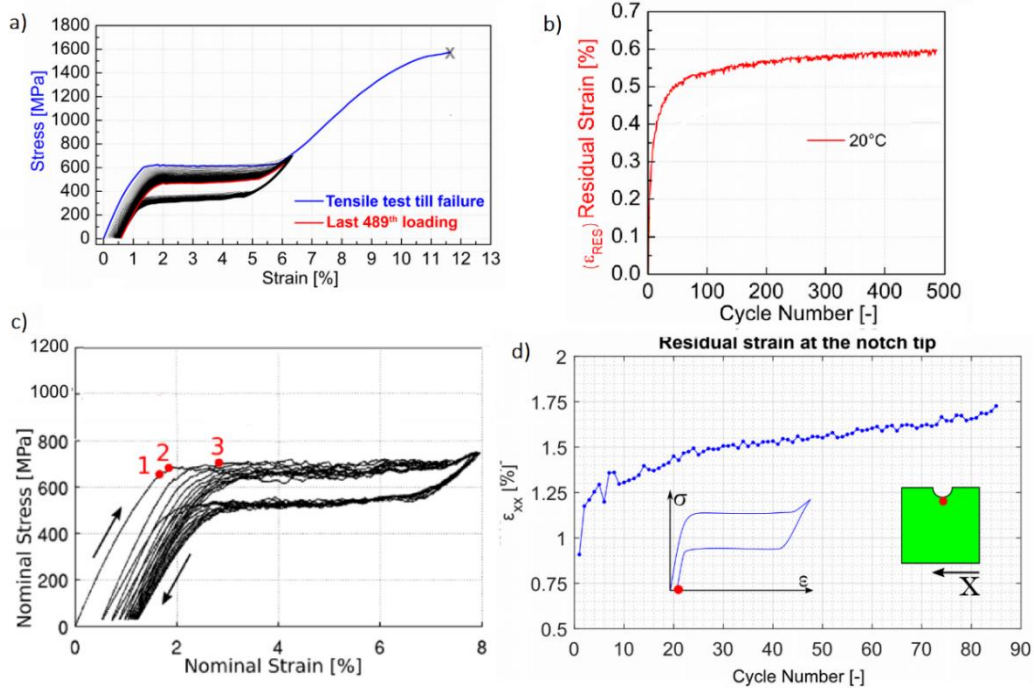


Fig. 4-8 experimental test results on the virgin sample (a, b) and the notched sample (c, d): a) cyclic tensile test till failure and the monotonic tensile test till rupture of the virgin sample, b) accumulation of the transformation induced plasticity on virgin sample c) cyclic macroscopic response of the notched ribbon, d) accumulation of residual strains at the notch-tip upon repeated tensile-unloading cycles

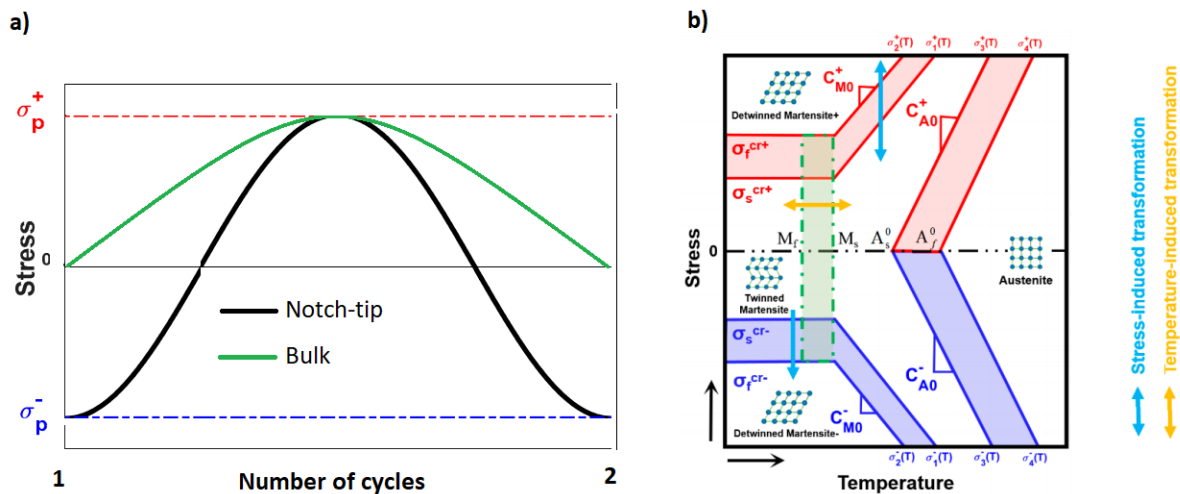


Fig. 4-9 Uniaxial tensile-compressive load applied at the notch-tip upon with peak stresses of $\sigma + p$ under tension and $\sigma - p$ under compression [241]

The stress-strain response of the superelastic material under the tension-compression was presented by Wang et al. [241], as it is represented in Fig. 4-10, which indeed mimics the local stress-strain response at the notch-tip in our notched specimens. As discussed in section 4.3.2 (Fig. 4-4), due to

the plastic deformation evolved at the notch-tip in the first loading, upon the subsequent unloading compressive stresses are induced at the notch-tip. Thus, the subsequent macroscopic tensile-unloading cycles turn into the tension-compression stress-strain response at the notch-tip as it is depicted in Fig. 4-11d, path **C-O-T** (also see the associated schematic representation of the interaction between the time-deformation response between the bulk and the notch-tip in Fig. 4-9a).

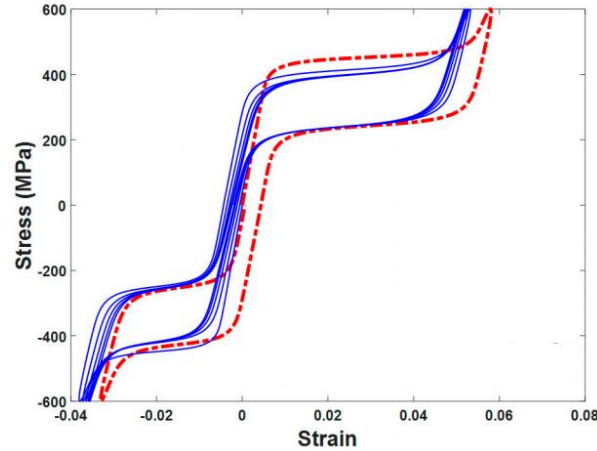


Fig. 4-10 The stress-strain behavior of a superelastic SMA material under cyclic loading conditions which begins with compression, considering tension-compression asymmetry [241]

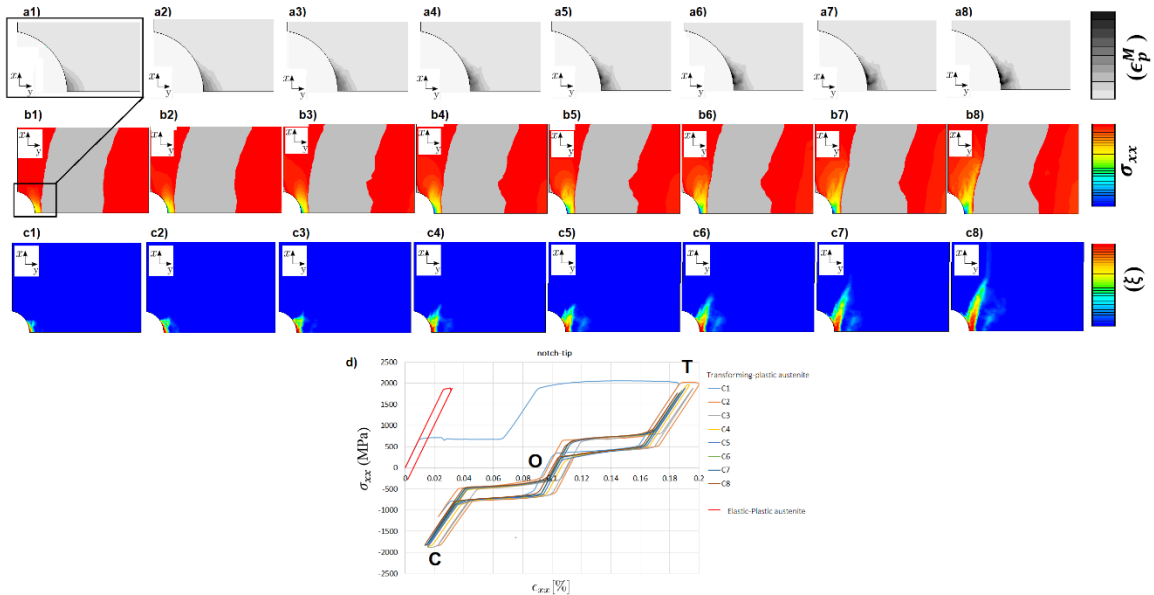


Fig. 4-11 FEM results at the unloading stages evaluated upon 8 cycles: a1-a8) the evolution of the local compressive stresses, b1-b8) evolution of the accumulated eq. plastic strain in martensite, c1-c8) accumulation of the residual (compression induced) martensite, d) cyclic evolution of axial component of stress at the notch-tip

From the second cycle, the notch-tip experiences twice (double-stage) phase transformation: $M \rightarrow A$ reverse transformation from **C** to **O**, and the forward $A \rightarrow M$ phase transition from **O** to **T**; which reversely occur when the external load is released again (Fig. 4-11d). Fig. 4-11a1-a8, Fig. 4-11b1-b8, and Fig. 4-11c1-c8, respectively, represent the evolutions of plastic strains, compressive stresses, and the remnant (compression-induced) martensite around the notch-tip at the end of unloading stages, over the simulated 8 macroscopic loading-unloading cycles. The macroscopic loading-unloading cycles arise the accumulation of plastic strains at the notch-tip as it is schematically shown

in Fig. 4-12 and through the colormaps in Fig. 4-11 a1-a8. The accumulation of plastic strains (and enlargement of the zone of the plastically deformed zone over the cycles) results in the gradual increase of the values of compressive stresses and the zone under compression around the notch (see colormaps in Fig. 4-11 b1-b8); thus, accumulation of remnant martensite (see colormaps in Fig. 4-11 c1-c8) at the end of external unloading steps. The direction of the propagation of the plastic zone and residual martensite complies with the direction of the MT-band.

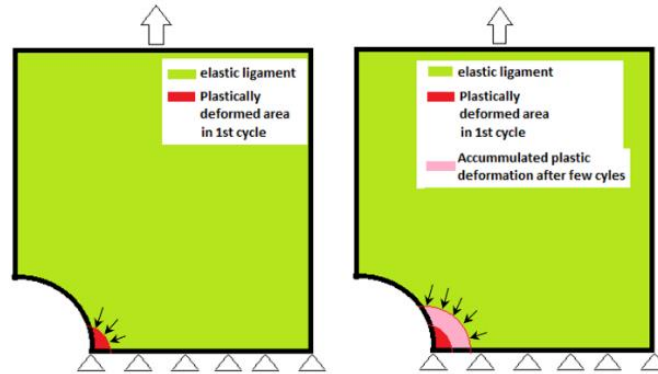


Fig. 4-12 schematic representation of the induced compressive loads (shown by arrows) from the elastic ligament on the border of the permanently deformed plastic zone at the notch-tip. Since the plastic area enlarges upon cyclic loading the notch-tip could be partially more and more shielded from the induced compressive stresses –by the added intermediate plastic ligament shown in pink color– by increasing the number of cycles.

In essence, the plasticity taking place at the notch-tip at high stresses beyond the plateau stress-induced by the stress concentration effect of the notch- turns into some changes in the cyclic responses of the material at the notch-tip:

- shifts the mean stress from $\sigma_{max}/2$ to \sim zero (if the tension-compression symmetry is assumed)
- results in $R = (\sigma_{min}/\sigma_{max})$ to change from zero to ~ -1 .
- results in the evolution of compressive stresses at the unloading course
- turns in the evolution and accumulation of plastic (unrecovered) strains
- leads to a double-stage phase transformation –forward and reverse martensitic transformation– upon per single loading-unloading stage
- Turns in remnant (compression-induced) martensite volume fraction at the notch-tip the end of external unloading steps. This is well confirmed by the X-ray microdiffraction results, discussed in the following.

As it is seen in Fig. 4-11d, after the 2nd cycle, the yield stress at the notch-tip may not reach at maximum load, while the induced compressive stress could exceed the yield point in unloading; thus, the maximum notch-tip strain at maximum load remains relatively constant (Fig. 4-13a,b), while the residual strains at the notch-tip gradually –slightly– increase over the repeated cycles till it relatively saturates after a few cycles (Fig. 4-14a,b). This saturation of unrecovered strains could be since the accumulated plastic strains –thus, increasing the size of the permanently deformed zone– after a few cycles would partially shield the notch-tip from being further affected by compressive stresses which are induced by an elastic ligament (see Fig. 4-12), thus, prohibits the additional plastic strains at the notch-tip.

The evolution of the total strain along the notch-tip cross-section at maximum load is represented in Fig. 4-15a,b, where represents a good agreement between the experimental and numerical results. At maximum load, the strain is maximum at the notch-tip and it sharply decreases at the distal point from the notch-tip till it reaches the nominal strain at the center of the notch-tip cross-section as it is seen in Fig. 4-15a,b.

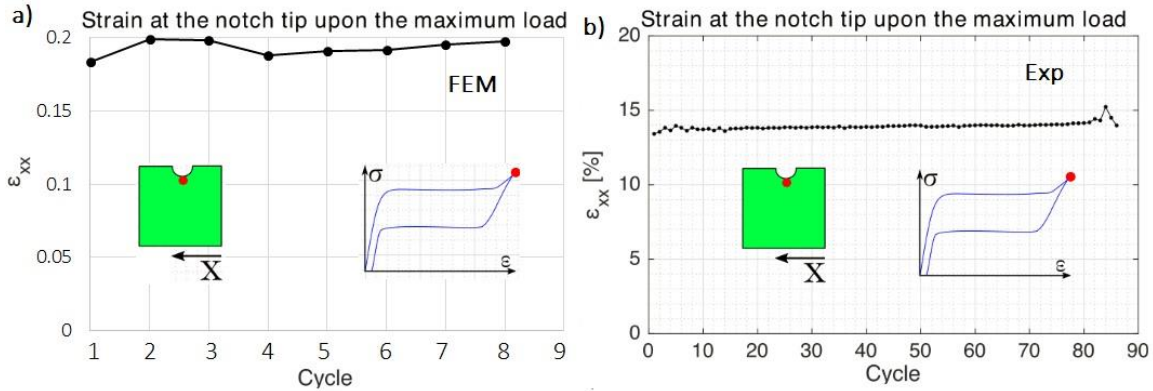


Fig. 4-13 Evolution of axial strain at maximum macroscopic load, a) FEM, b) DIC

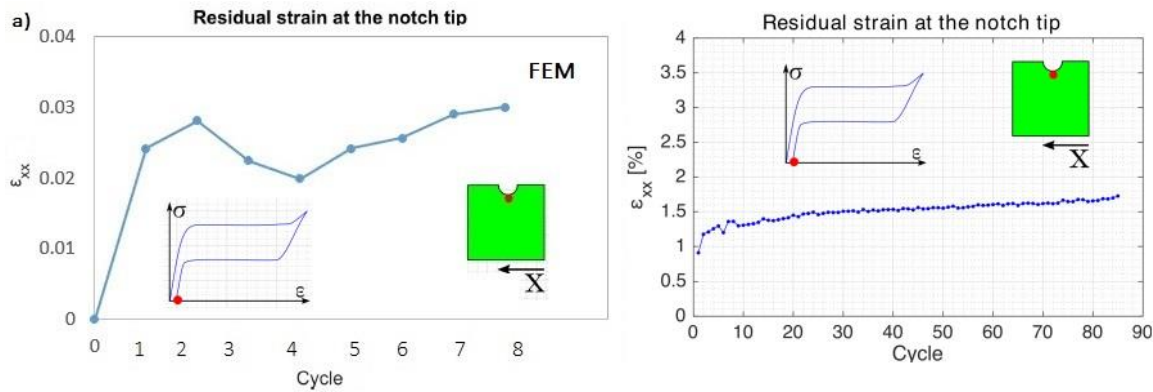


Fig. 4-14 evolution of accumulated residual axial component of strain at the notch-tip after macroscopic unloading during cyclic loading, a) FEM, b) DIC

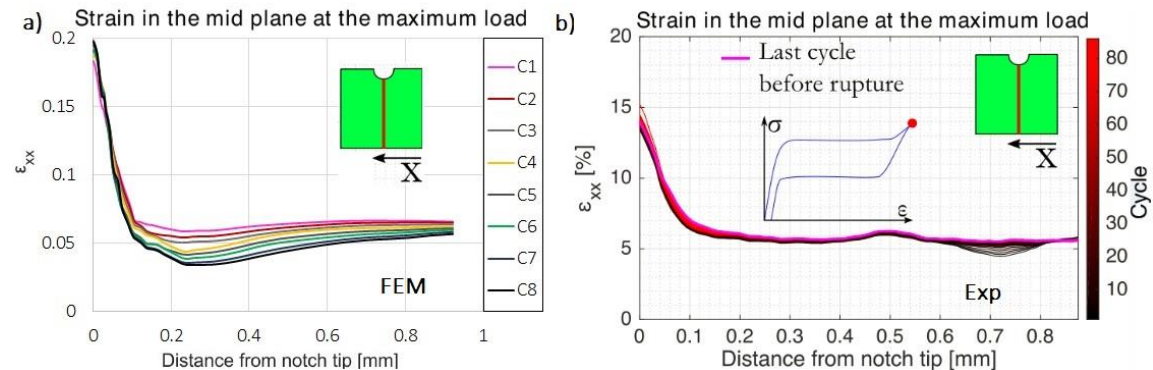


Fig. 4-15 Evolution of axial component of strain ahead of the notch-tip at maximum macroscopic load upon cyclic loading, a) FEM, b) DIC

The numerically calculated distribution of the stress ahead of the notch-tip is represented in Fig. 4-16 at both maximum stress and unloading state. At the maximum load, the stress distribution shows the conventional stress distribution in elastic-plastic materials: the stress is restricted to the yield stress to

some extent (plastic zone), it increases due to removal of the plastic deformation constraints and it gradually decreases ahead of the rest of the notch-tip ligament –which is in elastic state–, till it reaches to the nominal stress at $\sim 0.3\text{mm}$ distance from the notch-tip (Fig. 4-16a). In the unloading stages, by distancing from the notch-tip the compressive stresses remain to some extent from the notch-tip; it turns to a tensile stress state and again it collapses to zero at $\sim 0.44\text{mm}$ distance from the tip, which is indeed the nominal stress in the unloaded state (Fig. 4-16b).

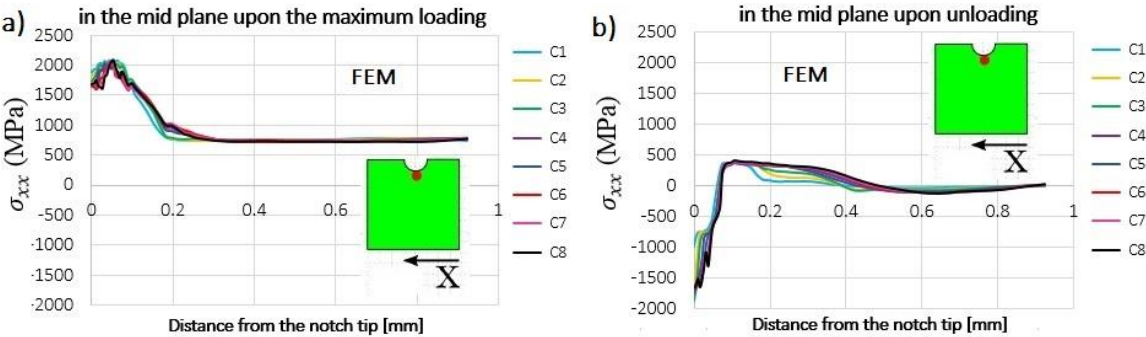


Fig. 4-16 FEM results of the evolution of the distribution of the axial component of stress ahead of the notch-tip upon cyclic loading: a) at maximum macroscopic load, b) at macroscopic unloading

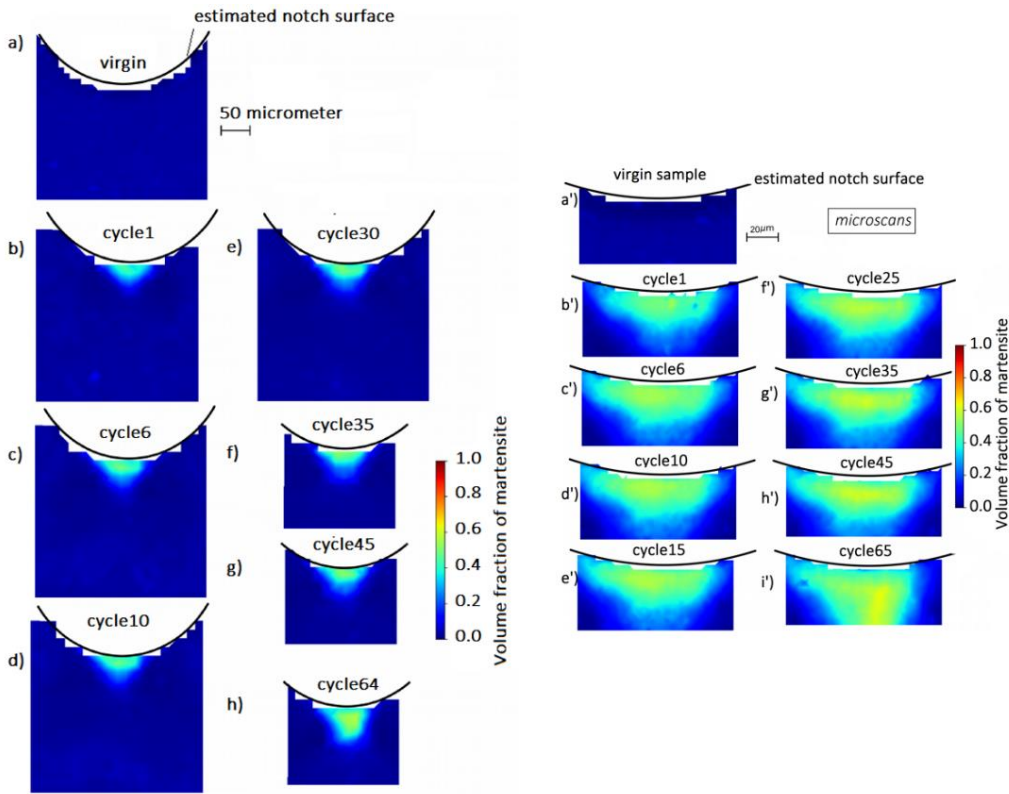


Fig. 4-17 XRD results, the evolution of the remnant martensite at the end of unloading stages upon 65 cycles; (a-h) macro scans; (a'-h') micro scans

▪ *XRD Results comparison to FEM results (plastic-SMA)*

The XRD results confirm the development of the remnant martensite volume fraction zone at the notch-tip at the end of unloading stages, the size of which increases over the cycles (Fig. 4-17) as it

was prematurely predicted by the numerical investigations. The distribution of the remnant martensite ahead of the notch-tip is represented in Fig. 4-18a and Fig. 4-18b, obtained from the numerical results and X-ray microdiffraction experiments, respectively.

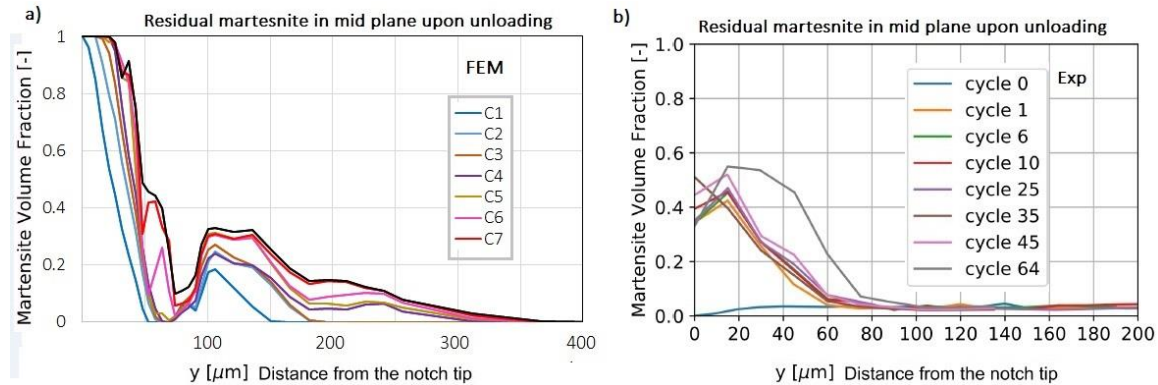


Fig. 4-18 distribution of the residual (compression-induced) martensite ahead of the notch-tip after macroscopic unloading during cyclic loading, a) FEM, b) XRD

4.3.1. Fractography

Figure Fig. 4-19 represents the SEM images of the fatigue fracture surface. Crack initiation is obvious at multiple sites along the notch-tip within the thickness, in Fig. 4-19i; followed by fatigue striations. At the end of the fatigue crack propagation zone, a slight combination of fatigue striations and ductile voids are seen. Then, the transition area between the fatigue part of the fracture on the right, and the final fracture on the left is seen. Relatively denser fatigue striations between the crack initiation and transition areas are seen (Fig. 4-19a,b,d). The area of a cyclic crack growth accounts for about 8% to 9% of the overall fatigue fracture surface at given test conditions. High magnification images of the final rupture area in Fig. 4-19-j to Fig. 4-19-k show that the final rupture zone comprises predominantly dense ductile dimples with a mean size of 2-3 μm; and void nucleation, growth, and coalescence dominating the failure which is in agreement with the results of Gall et al.[243] Wang et al. [244] and Tyc et al. [118].

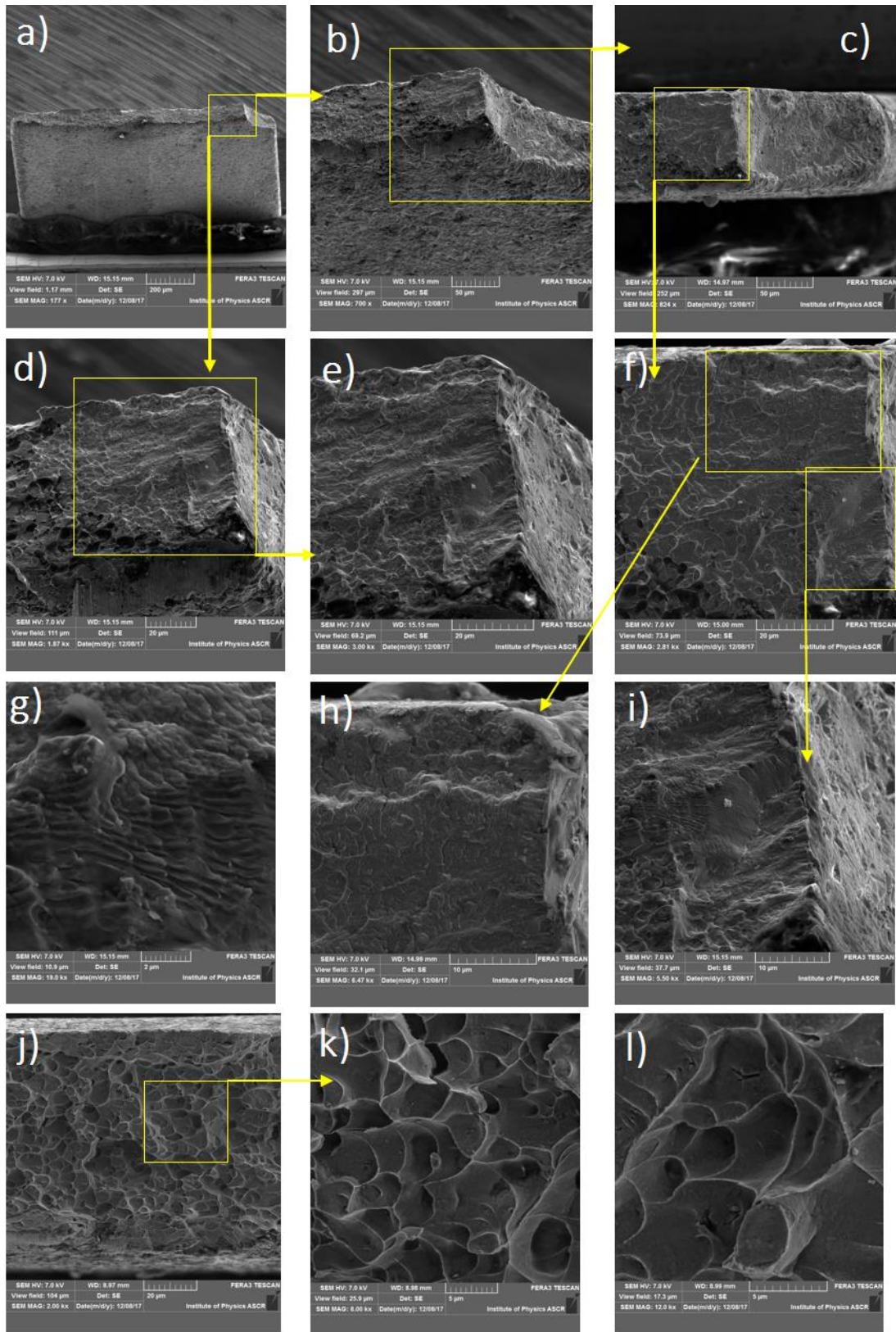


Fig. 4-19 SEM images of the superelastic specimen. Fatigue fracture under mechanical cyclic loading: a to i) the overall appearance of the crack initiation and fatigue crack propagation zones with local high magnifications; j, k, l) Final rupture surface

4.4. Conclusions

The effects of conventional plasticity (yield of martensite at high stress levels beyond the stress plateau stress) at the notch-tip was investigated on the local responses in a thin superelastic ribbon undergoing repeated loading-unloading cycles in mode I. First, the local behavior was compared with a reference case study in which the plasticity was excluded in FE simulations and the comparison revealed that excluding the plasticity from the analyses, results in a notable mismatch between the numerical results and the experimental observations; thus, it turns in significant inaccuracies in the prediction of the material's response to cyclic loading conditions at stress risers. The results revealed that due to the stress concentration effect of the notch, the martensitic transformation upon loading, first nucleates at the highest stress zones around the notch and extends towards the bulk along with the direction of maximum shear (so-called MT-band) by further loading. The transformation strains that evolve along with the MT-band are accommodated by elastic deformation of previously fully transformed material at the notch-tip, triggering a sharp stress increase at the notch-tip (thus, increase of stress concentration factor). The sharp stress increase at the notch-tip turns in the yield of martensite, which hinders the effective stress from the further increase. The elastically transformed bulk ligament induces compressive stresses on the permanently deformed material at the notch-tip, upon reverse martensitic transformation in unloading. The plastic strains accumulate at the notch-tip in loading stages over the cycles, result in the magnitude of compressive stresses and the size under compression to increase; thus, increase the volume fraction of remnant (compression-induced martensite) at the end of cycles. Another effect of plasticity is the fact that from the second cycle the notch-tip experiences both forward and reverse phase transformation upon per macroscopic loading and unloading stages.

Further, it was found out that the material parameters (maximum transformation strain, elastic moduli mismatch between A and M phases), as well as the geometric parameters (notch acuity), have significant effects on the above-discussed local phenomena.

CHAPTER 5. Superelastic notched NiTi ribbon: the effects of martensitic transformation and plasticity on the stress concentration factor

5.1. Introduction

The severe nonlinear behavior induced by the martensitic transformation and the subsequent plastic deformation of martensite results in a complex local redistribution of mechanical gradients at stress risers in superelastic shape memory alloy (SMA) elements. However, the simple linear elastic fracture mechanics (LEFM) equations are being widely used in the evaluation of the fracture response of superelastic parts which has caused non-conclusive remarks on the effects of martensitic transformation on their fracture parameters, e.g. stress intensity factor (SIF) and material toughness. Moreover, the linear elasticity method is frequently used in the literature to evaluate the stress intensity range (ΔK), when the empirical relation between fatigue crack growth rate and ΔK ($da/dN - \Delta K$), is being evaluated. Further, the plastic deformation of detwinned martensite at high stresses well beyond the transformation stress plateau, which is expected at the root of stress risers, is poorly taken into account in the fracture mechanics of shape memory alloys.

This chapter presents a numerical analysis on the role of both forward martensitic transformation and plastic deformation, as well as the notch sharpness, on the local evolutions of stress at the notch-tip, thus, the changes in notch stress concentration factor (K_{tn}) upon the gradual application of the macroscopic tensile load on a thin notched superelastic NiTi ribbon. The results reveal that the heterogeneous evolution of forward martensitic transformation upon monotonic loading results in irregular changes in notch stress concentration factor; i.e. the stress concentration factor evolves in 5 distinct stages upon completion of macroscopic phase transformation stress plateau. Accordingly, the results represent the inefficacy of the LEFM method in the evolution of the stress concentration factor (thus, the SIF) and toughness under monotonic loading, such that the stress intensity range (ΔK) under fatigue loading in superelastic SMA components since under fatigue conditions both the maximum and minimum stress intensity levels are modified to different levels due to the transformation effects and notch-tip plasticity.

The work corresponding to this chapter has been published as:

Pejman Shayanfard, Petr Šittner, Luděk Heller, Pavel Šandera, Finite element analysis on the effect of martensitic transformation and plastic deformation on the stress concentration factor in a thin notched superelastic NiTi ribbon, *Functional Materials Letters*, 2020, Vol 13(05), pp. 2051028, Doi: <https://doi.org/10.1142/S1793604720510285>

and is attached to the end of the thesis.

The paper presents a purely numerical analysis that was, however, inspired by questions raised by related experimental research work, discussed in CHAPTER 4. The part, which is the original work of the author of this dissertation, presents in the cited paper is the analysis primary idea, the processing of all finite element simulations and post-processing of the results, comparison and interpretation of the results and writing the manuscript which was revised thoroughly after comprehensive consultations with coauthors.

CHAPTER 6. NiTi Actuators with Stress Risers: Role of Plasticity

In this chapter, the evolution of local martensitic transformation (MT), plastic deformation, and mechanical gradients are analyzed both experimentally and numerically, in a thin actuator notched NiTi ribbon. While in FE analyses the plastic deformation is taken into account, the results are compared to a reference case-study where the plasticity is excluded from the simulations.

6.1. Numerical Simulation Method

Three-dimensional finite element simulations of thermally induced $A \leftrightarrow M$ phase transformation were carried out on a thin shape memory NiTi ribbon including two-sided semi-circular notches (Fig. 6-1a), to study the role of both MT and plastic deformation of detwinned martensite on the evolution of the local mechanical fields upon thermal cycling under a constant applied macroscopic 200 MPa tensile nominal stress. Since the material model used in this study (model proposed by Choudhry and Yoon [57], introduced in CHAPTER 3) allows us to combine SMA behavior –martensitic transformation– with the plasticity of both phases, the case in which the plasticity occurs in detwinned martensite beyond the transformation stress plateau (plastic-SMA, see shape memory material parameters in section 3.3.2) is examined and the results are compared to a reference case-study where the plasticity is neglected (ideal-SMA):

- *ideal-SMA (iSMA)*: the plasticity was not activated in material options
- *plastic-SMA (pSMA)*: the yield stress of the martensite and austenite were set to 1270 MPa and infinite, respectively.

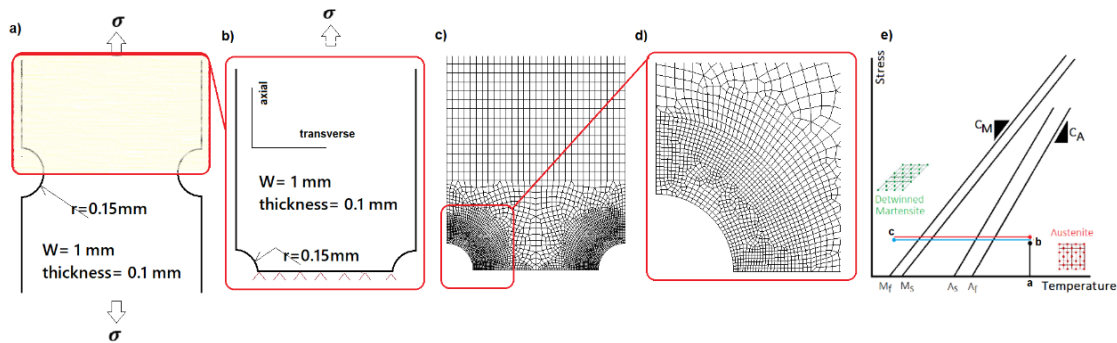


Fig. 6-1 (a) Geometry of simulated double-notched ribbon (b) that was reduced using symmetry (c) and discretized using finite element mesh (d) refined around the notch (e) Schematic of the applied thermomechanical loading path, presented in the stress-temperature phase diagram of SMAs

Taking advantage of symmetry, half of the specimen was considered in simulations (Fig. 6-1b). The width and thickness of the ribbon and the notches' radius are 1mm, 0.1mm, and 0.15mm, respectively. The model was discretized using element 7 which is an eight-node, isoparametric, arbitrary hexahedral⁶ (Fig. 6-1c). The mesh was highly refined in the zone of expected high-stress gradients i.e. around the notch-tip as illustrated in Fig. 6-1d. The loading sequence consisted of two steps similar to the procedure followed in experiments: i) applying 200MPa tensile stress in austenite state

⁶ MSC Marc 2017, Documentation, Vol B: Element Library

at 160°C (path a-b in Fig. 6-1e); ii) homogeneous cooling-heating cycles with a constant rate between 160°C-10°C (path a-b-a in Fig. 6-1e).

6.2. Results and Discussion

6.2.1. The evolution of the inhomogeneous martensitic transformation (MT) upon cooling-heating

The spatial evolution of forward MT upon cooling is heterogeneous. Due to Clausius-Clapeyron relation, during cooling martensite first evolve at the regions with higher stress levels (see the schematic representation of Clausius-Clapeyron relation in stress-temperature diagram shown in Fig. 6-1d). Accordingly, the evolution of the stress at the notch-tip is non-monotonous during the forward MT upon cooling under the constant applied tensile force.

The results reveal that upon the cooling, the stress at the notch-tip and its very close vicinity evolves oppositely to that in distal material points from the notch-tip. During cooling, the stress at the notch-tip and its vicinity increases, while the material points beyond this zone experience stress relaxation. Particularly, within a $\sim 0.036\text{mm}$ distance from the notch-tip – about 25% of the notch radius– (so-called stress rising zone, see Fig. 6-2a) the stress increases, as it is seen from the related stress-temperature evolutions in Fig. 6-2b. Beyond this zone, however, the material experiences

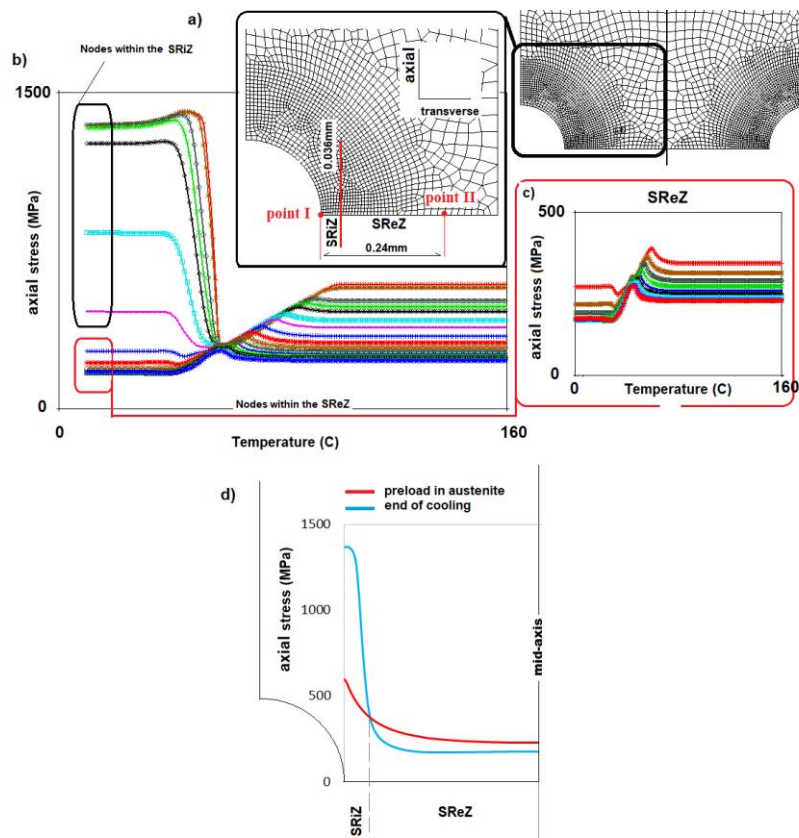


Fig. 6-2 (a) Representation of the SRiZ and SReZ (at the notch-tip cross-section) where the stress rises and relaxes upon cooling, respectively; (b) stress-temperature response of the entire material points at SRiZ and SReZ; (c) magnified stress-response of SReZ; (d) two-dimensional plot of the distribution of the axial stress along with the notch-tip ligament at the preloaded state (red curve) and the end of cooling (blue curve), clearly showing the SRiZ where the stress increases upon cooling, and the SReZ where the stress relaxes during cooling

stress relaxation during cooling as it is seen in Fig. 6-2c, which is the so-called stress relaxing zone (SR_eZ). The delimitation of SR_iZ and SR_eZ, can be simply achieved by plotting the stress distribution at the notch-tip ligament in the preloaded state and the end of cooling (Fig. 6-2d). Moreover, it is possible to delimit SR_iZ and SR_eZ using the temperature evolution of transverse stress along the notch-tip ligament, as is illustrated by the three-dimensional colormap in Fig. 6-3b. In Fig. 6-3b,

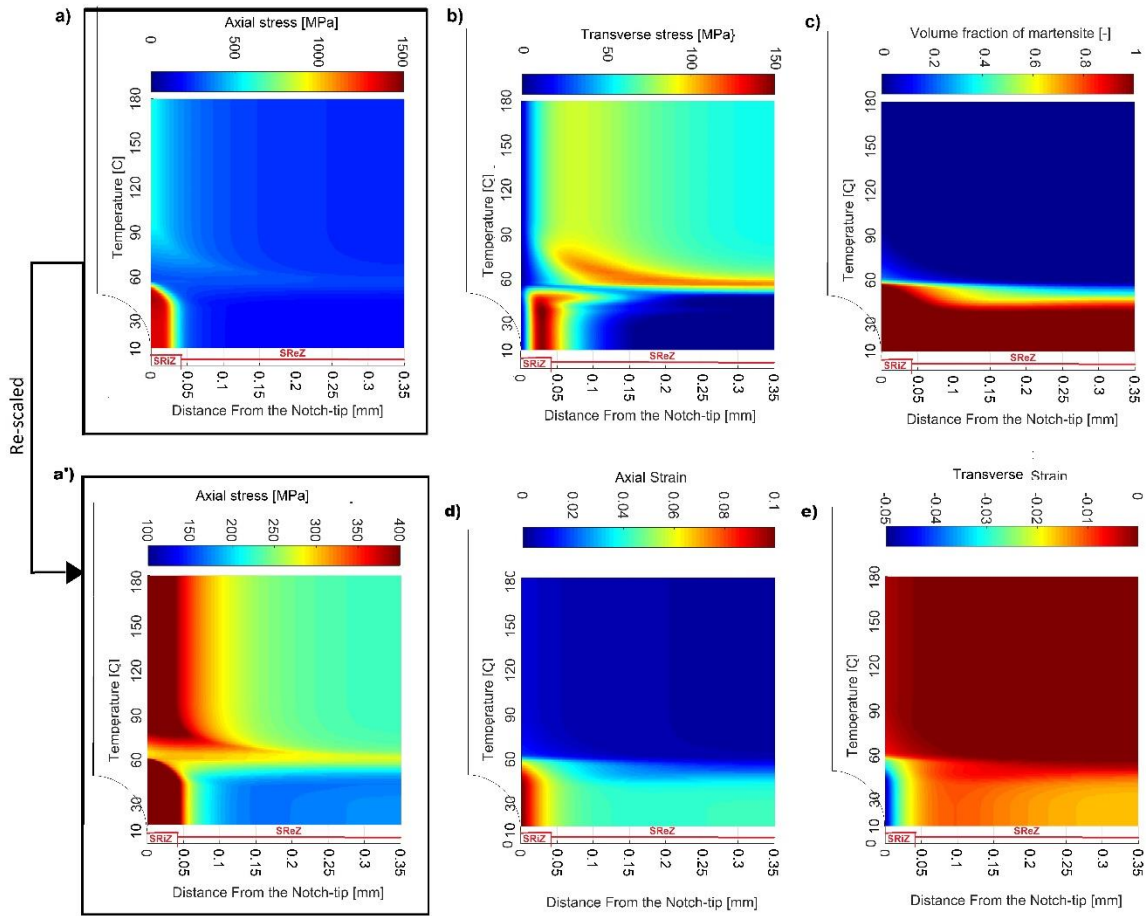


Fig. 6-3 Three-dimensional colormaps representing the temperature evolutions of stress fields and the martensitic transformation upon cooling, along the notch-tip ligament: (a, a') axial stress; (b) transverse stress; (c) volume fraction of martensite;

the vertical cuts through the colormap represent the spatial evolution of the stress along the ligament while the horizontal cuts represent the temperature evolution of the stress for individual material points along the notch ligament. The transverse stress clearly shows local maxima at temperatures below the $\sim 65^{\circ}\text{C}$. These maxima are due to the Poisson effect caused by MT-induced large strains in SR_iZ. Hence, local maxima in transverse stress split the ligament into SR_iZ and SR_eZ. Fig. 6-3a and Fig. 6-3a' represents the three-dimensional colormap of the temperature evolution of axial stress along the notch-tip ligament, while the colorbar scales the stress value between 0-1500 MPa and 100-400 MPa, respectively. Fig. 6-3a clearly shows the stresses within the SR_iZ increase upon cooling, reaching their minima at $\sim 65^{\circ}\text{C}$. In contrast, Fig. 6-3a' illustrates that the stresses within the SR_eZ decrease upon cooling, reaching their maxima at $\sim 65^{\circ}\text{C}$. Fig. 6-3c shows the three-dimensional temperature evolution of martensite volume fraction upon cooling, at the notch-tip ligament, which shows the material near the notch-tip (SR_iZ) undergoes $A \rightarrow M$ phase transformation superior to the

SReZ, due to the stress concentration effect of the notch. Fig. 6-3d and Fig. 6-3e represent, respectively, the corresponding three-dimensional colormaps of the temperature evolutions of the total axial and transverse strain components, which reveal significantly higher strain changes during cooling takes place within the SRiZ in comparison to the SReZ.

To understand such distinct stress state evolutions in SRiZ and SReZ, Fig. 6-4 summarizes the stress-strain-phase fraction-temperature evolutions during cooling under constant 200MPa applied external stress. Distinct stress-strain states that exist in SRiZ and SReZ are analyzed hereinafter in terms of axial stresses and strains at the notch-tip denoted as Point 1 and a distal Point 2 along the notch-tip ligament, respectively, as indicated in Fig. 6-5c. Note that at both points the stress-strain state is nearly uniaxial, which facilitates the analysis.

As discussed above, the temperature-stress and temperature-strain responses at the notch-tip upon uniform cooling-heating is non-monotonous (see black curves in Fig. 6-4a,b). Considering the unrecoverable plastic strains evolved during cooling at the notch-tip, the whole cooling-heating cycle can be explained as below:

- *The first cooling step: accompanied by the local evolution of plastic strains*

The evolutions of stress and strain at the notch-tip can be split into four consecutive stages upon cooling, marked with important turning points (P_0 - P_5) of stress-strain- ξ (martensite volume fraction)-temperature paths depicted in Fig. 6-4a,b,c,d. Fig. 6-5a and Fig. 6-5b represent the colormaps of the total axial strain at turning points P_0 - P_5 obtained from DIC measurements and FE simulations, respectively. The stress-strain-temperature paths at the notch-tip stems from heterogeneous MT around the notch as evidenced by distributions of martensite volume fraction (ξ) at important turning point P_0 - P_5 shown in Fig. 6-5c, which were converted into simplified colormaps in Fig. 6-5d splitting the total transforming sample volume into three fractions according to the degree of martensite straining, i.e., detwinning (the same as it was discussed also in 4.3). The degree of martensite detwinning is supposed to be contrarily proportional to the austenite volume fraction, restraining the martensite from full detwinning. The three fractions are consecutive: i) near-complete austenite ($\xi \leq 0.2$), where the martensite is believed to be highly constrained by the austenite; ii) partially detwinned martensite ($0.2 < \xi < 0.9$), where the austenite is still markedly restraining the martensite from full detwinning; iii) nearly fully detwinned martensite ($\xi \geq 0.9$), where it is almost free to fully detwin.

- *stage I: Martensite nucleation and completion at the notch-tip, path P_0 - P_1 - P_2 :*

In path P_0 - P_2 , the $A \rightarrow M$ martensitic transformation nucleates at notch-tip where the stresses are higher. The temperature dependence of the transformation stress which decreases upon cooling according to Clausius- Clapeyron equation, results in a stress relaxation during the $A \rightarrow M$ phase transformation in path P_0 - P_2 (see path P_0 - P_2 in Fig. 6-4a,b,c and the colormaps showing turning points P_0 - P_2 in Fig. 6-5c,d). The notch-tip follows the superelastic-like stress-strain response shown in Fig. 6-4b (path P_0 - P_2), where the stress relaxation path lies between points P_0 - P_1 . The stress plateau between points P_1 - P_2 in Fig. 6-4b correlates to the fast completion of MT at the notch-tip which takes place in a small temperature increment (see path P_1 - P_2 in Fig. 6-4a,c); where the stress remains constant. This stress relaxation at the notch-tip proceeds into the entire SRiZ, which is compensated by stress increase at SReZ (path P_0 - P_2 in Fig. 6-4aa,bb) because the applied external load is constant

and the equilibrium must hold at the notch-tip cross-section. Nevertheless, this stress increase in SReZ is comparably small not promoting the MT within SReZ, as its size is much larger than that of SRiZ.

The total strain at point P_2 is the summation of the transformation strain and an elastic strain of the austenite phase induced upon pre-loading (see Fig. 6-4d):

$$(\varepsilon^{tot})_{point (P_2)} = \varepsilon_A^{el} + \varepsilon_{A \rightarrow M}^{notch-tip}$$

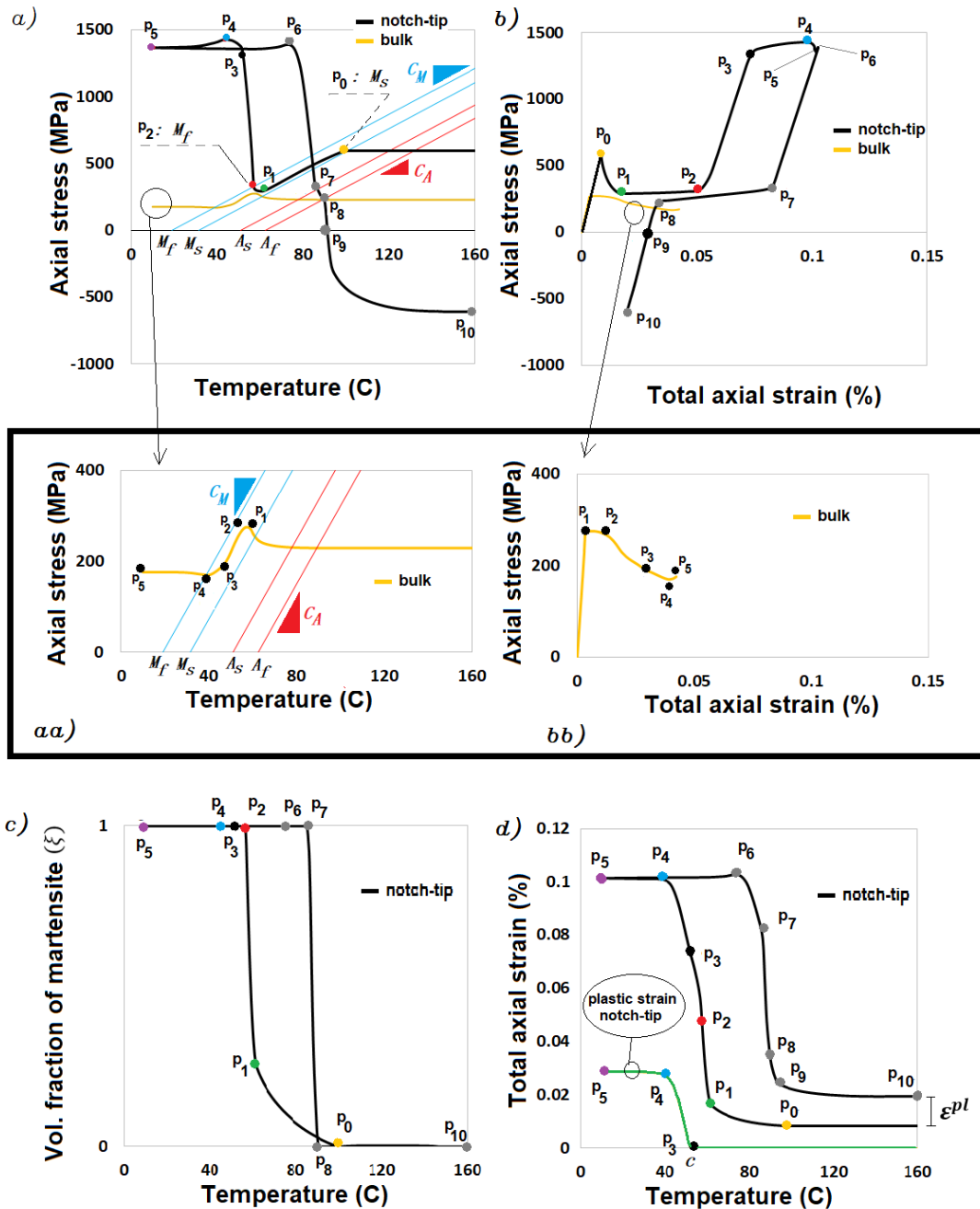


Fig. 6-4 FE results of the comparison between the ideal-SMA case [214] and the present studied case of plastic-SMA material, the evolution of the stress-strain-temperature responses at the notch-tip upon the first cooling stage: a) stress-temperature evolution and the representation of the transformation lines M_s , M_f , A_s and A_f ; b) stress-strain response; c) evolution of volume fraction of martensite; d) simultaneous representation of the evolution of the total strain and the equivalent plastic strain in martensite by the black and orange curves, respectively.

- stage 2: MT propagation into the bulk to the onset of the notch-tip plasticity, path P_2 - P_3

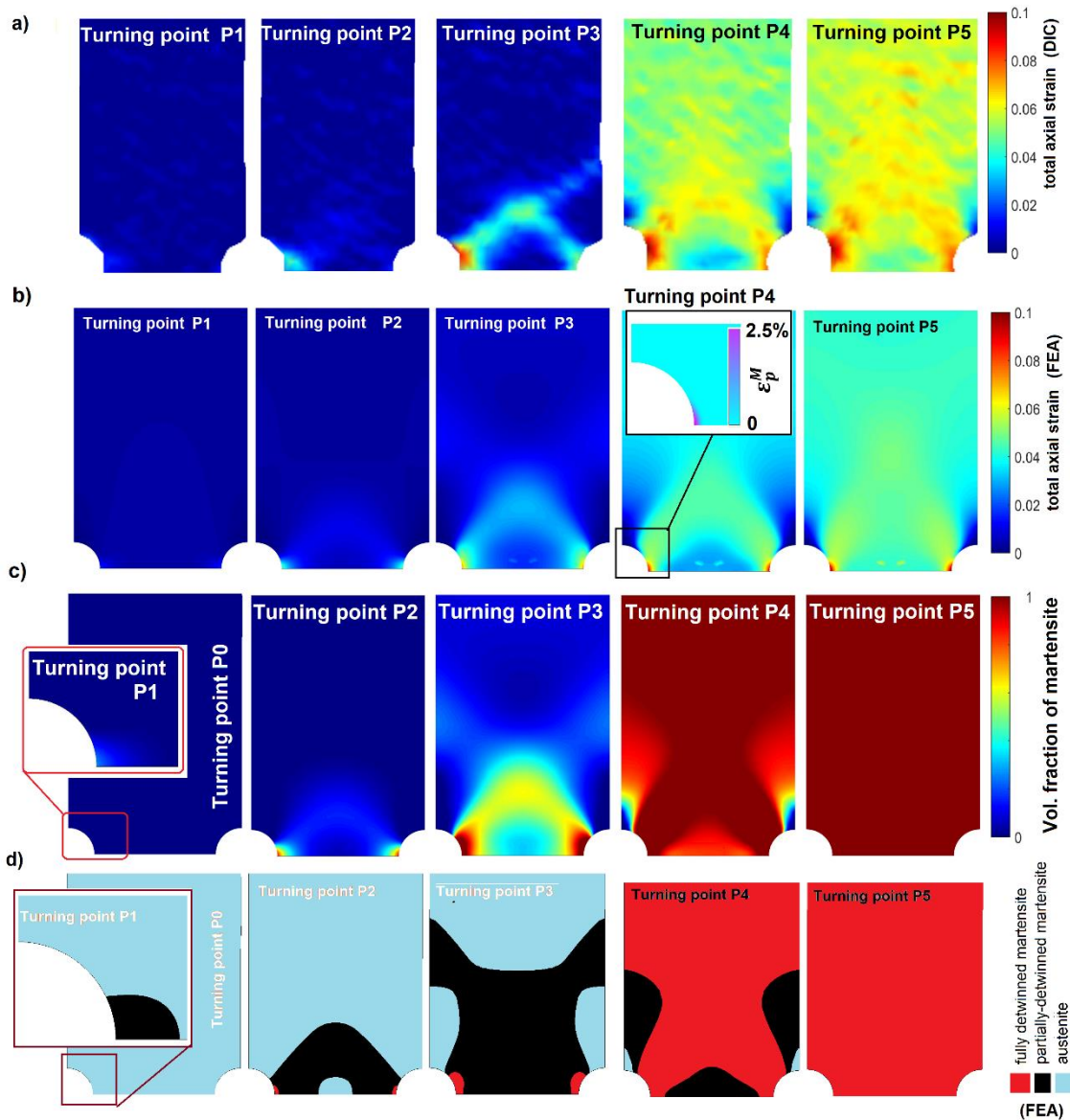


Fig. 6-5 (a) DIC results, colormaps of the spatial distribution of total axial strain through the turning points P_0 - P_5 ; (b) FE results, colormaps of the spatial distribution of total axial strain through the turning points P_0 - P_5 ; (c) FE results, colormaps of the martensite volume fraction at the important turning points P_0 to P_5 , denoted in Fig. 6-4; (d) the simplified representation of martensite volume fraction at the important turning points P_0 to P_5 (denoted in Fig. 6-4), splitting the total transforming sample volume into austenite ($VFM < 0.2$), partially detwinned martensite ($0.2 \leq VFM \leq 0.9$) and fully detwinned martensite ($VFM > 0.9$)

Once the notch-tip and its very close vicinity have fully transformed into the detwinned martensite, it can be regarded as an elastic martensite inclusion, surrounded by austenite ligament (see point P_2 in Fig. 6-4a,c and its corresponding colormaps in Fig. 6-5c,d) which is being transformed to martensite upon further cooling. Further cooling turns into the MT propagation into the bulk towards the direction of maximum shear (so-called MT-band) (see the colormaps at turning point P_3 in Fig. 6-5c,d). The transformation strains being evolved within the MT-band must be accommodated by elastic deformation of the adjacent fully transformed zone at the notch-tip which results in sharp stress increase at the notch-tip (path P_2 - P_3 in Fig. 6-4a,b) and stress relaxation at SReZ (see path P_2 - P_3 in Fig. 6-4aa,bb). Thus:

$$(\varepsilon^{tot})_{point (P_3)} = (\varepsilon^{tot})_{point (P_2)} + (\varepsilon_{A \rightarrow M}^{MT-band})_{el}^{notch-tip}$$

Where $(\varepsilon_{A \rightarrow M}^{MT-band})_{el}^{notch-tip}$ denotes the extra elastic strain of detwinned martensite at the notch-tip induced to accommodate the transformation strains within the MT-band (Fig. 6-4d).

- *stage 3: continuation of MT propagation into the bulk accompanied by plastic deformation at the notch-tip, path P₃-P₄*

Upon propagation of MT towards the bulk along the MT-band, to some cooling extent (to point P₃), the induced transformation strains within the MT-band would be accommodated by elastic deformation of the martensite at the notch-tip as discussed in stage 2. However, once the stress at the notch-tip exceeds the martensitic yield stress σ_M^y , the rest of the transformation strains evolving along with the MT-band are rather accommodated by plastic strains of the yielded detwinned martensite inclusion at the notch-tip (see path P₃-P₄, the yellow curve in Fig. 6-4d), which turns into the saturation of stress to the yield stress (see the strain hardening in path P₃-P₄ in Fig. 6-4b). Thus:

$$(\varepsilon^{tot})_{point (P_4)} = (\varepsilon^{tot})_{point (P_3)} + (\varepsilon_{A \rightarrow M}^{MT-band})_{pl}^{notch-tip}$$

Where, $(\varepsilon_{A \rightarrow M}^{MT-band})_{pl}^{notch-tip}$ is the transformation strains evolved within the MT-band which is accommodated by plastic deformation of plastically deformed detwinned martensite at the notch-tip (see Fig. 6-4e). The stress at SReZ (material point 2) further relaxes in this stage (see Fig. 6-4a-bb).

- *stage 4: MT completion, path P₄-P₅*

The last stage starts at the maximum stress at the notch-tip at turning point P₄ (Fig. 6-4a) that coincides with the near completion of the MT within the notch-tip ligament (see corresponding colormaps of P₄ in Fig. 6-5c,d). A zone of residual austenite remains in the notch-tip ligament at the border between SRiZ and SReZ (see colormap of turning point P₄ in Fig. 6-5c,d), where the stress-bearing capacity is limited by the transformation stress, which must be compensated by higher stresses at adjacent fully martensitic parts of the ligament. By further cooling, the MT completes at this zone thus increasing its loading capacity and allowing for stress relaxation of the notch-tip as shown by path P₄-P₅ in Fig. 6-4a and Fig. 6-4b; turning in rising of the stress at SReZ (Fig. 6-4a,bb).

- ***The first heating stage, plastic-SMA***

When the minimum temperature ($T_{min} < M_f$) is reached in the cooling step at point P₅ (see Fig. 6-4), the whole structure is fully detwinned to martensite, and plastic strains already exist at the notch-tip and its very close vicinity. By heating, the elastic ligament tends to undergo reverse M→A phase transformation and return to its original configuration in a pre-loaded state, which applies compression on the plastically deformed notch-tip zone.

Note that during heating, the reverse MT is superior at the lower stress zones based on the Clausius-Clapeyron equation. Thus, the reverse MT evolves from the bulk and shrinks towards the highest stress area at the notch-tip along with the MT-band. Recovery of transformation strains within the MT-band results in notch-tip to release the elastic deformations induced upon cooling –namely stage 2– in path P₆-P₇ (Fig. 6-4d); which indeed turns into a sharp stress relaxation at the notch-tip (Fig. 6-4a,b). In path P₇-P₈, the reverse MT proceeds at the notch-tip (Fig. 6-4a,c) where the material

follows the thermodynamics of SMAs characterized by reverse plateau stress (Fig. 6-4b). The reverse MT in path P₇-P₈ results in transformation strain (ϵ^{tr}) to be recovered at the notch-tip (Fig. 6-4d). By further heating to initial temperature within the path P₈-P₉ the elastic strain of austenite is recovered and in path P₉-P₁₀ the stress state at the notch-tip turns to compressive (Fig. 6-4a,b). At the end of heating at point P₁₀ the plastic strain ϵ^{pl} remains unrecovered at the notch-tip as it is seen in Fig. 6-4d. Under the present loading conditions, the level of compressive stresses at first heating is not enough to promote (secondary) A→M phase transformation at the notch-tip under compressive stresses; however, by the accumulation of unrecovered strains over the subsequent cycles, the compressive stresses may rise gradually and turn into A→M transformation under the compression as it will be discussed in section 6.2.2.

Briefly, the results comparing plastic-SMA material and the case study in which the plasticity is excluded from the analysis (ideal-SMA, see Fig. 6-6a-d), reveal that the effective stress in plastic-SMA at the notch-tip at the end of cooling is lower, while the total induced strain is higher than that in ideal-SMA. Besides, the plastic deformation at the notch-tip results in compression stress in heating which may arise the secondary phase transformation, i.e. compression-induced A→M, whenever its absolute value exceeds the forward stress plateau.

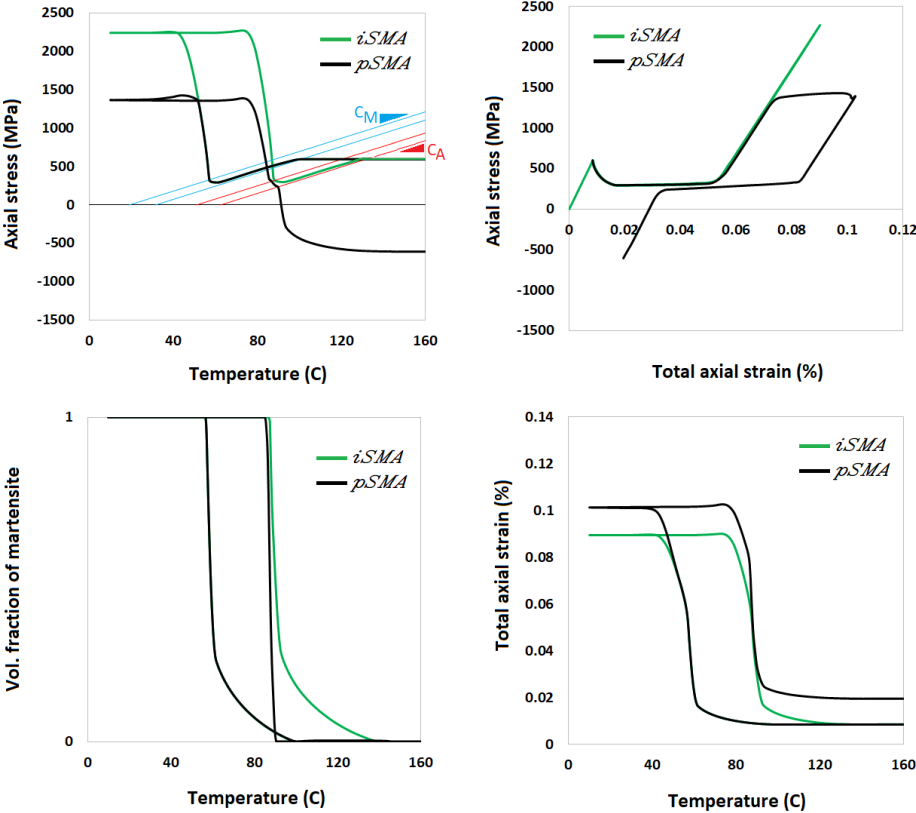


Fig. 6-6 a comparison between the real state behavior of the material at the notch-tip in the plastic-SMA case study, and the predicted behavior when the plasticity is excluded in simulations (ideal-SMA)

6.2.2. Cyclic Response

Fig. 6-7a,b represents the cyclic evolutions of the axial stress and total axial strain at the notch-tip, respectively, obtained from numerical simulations. The plastic strains gradually accumulate in cooling stages at the notch-tip over the thermal cycles (Fig. 6-7a) which turns into higher compressive

stresses at the end of heating stages (Fig. 6-7b). Indeed, the plastic deformation of detwinned martensite at high-stress levels and its effects remain very local; thus, the predicted strain-temperature response at the bulk remains fully reversible during the cyclic $A \leftrightarrow M$ phase transformation (see the yellow curve in Fig. 6-7a). The cumulative unrecovered strains at the notch-tip tend to saturate over the cycles (Fig. 6-7a), resulting in a saturation of consequent compressive stresses (Fig. 6-7b). Fig. 6-8a,b show the evolutions of the total axial strain along with the notch-tip ligament at the end of cooling stages (blue curves) and heating stages (red curves), derived from DIC experiments and numerical analyses, respectively. The results reveal that the unrecovered strains promote through the whole notch-tip ligament.

The experimentally and numerically derived spatial evolutions of the total axial strain at the end of cooling and heating stages over the 8 cycles are represented via the colormaps in Fig. 6-9a1-a8 and Fig. 6-9b1-b8, respectively. Fig. 6-9 reveals that the unrecovered strains nucleate from the notch-tip and further extend into the bulk through the MT-band [214].

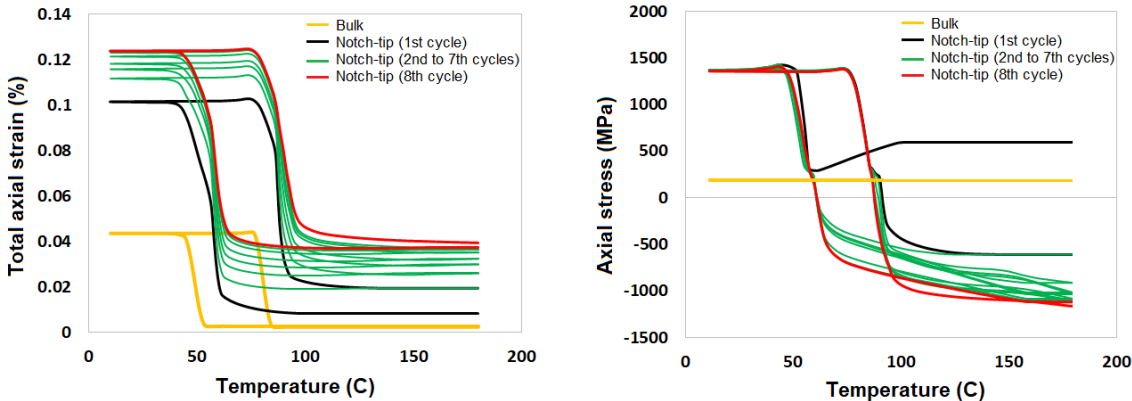


Fig. 6-7 plastic-SMA material response under 200 MPa constant far-field (external) stress: (a) strain-temperature responses at the bulk and the notch-tip upon thermal cycles; (b) stress-temperature response at the bulk and the notch-tip upon thermal cycles

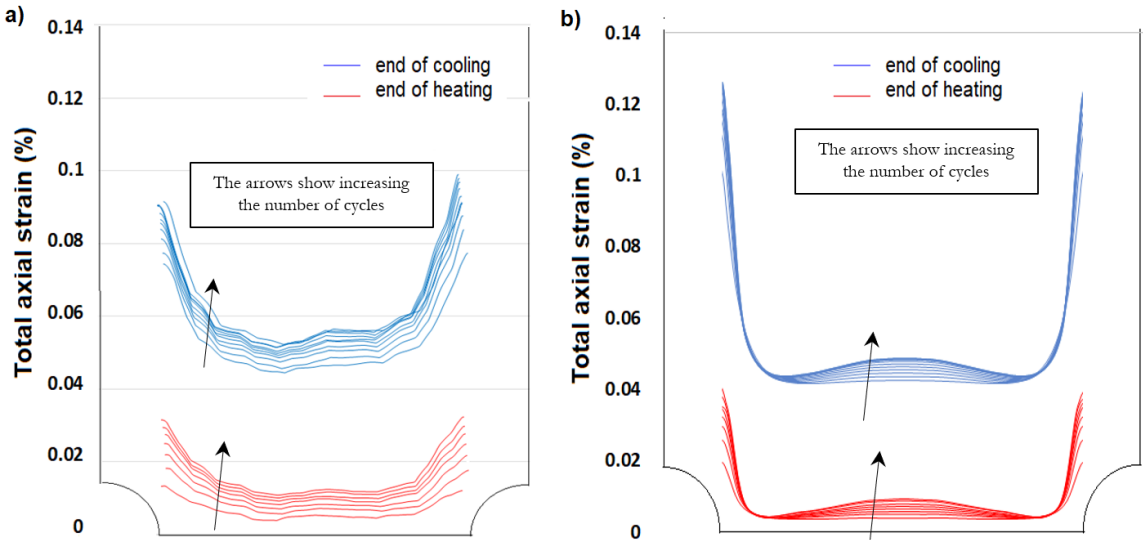


Fig. 6-8 DIC results of the distribution of total axial strain ahead of the notch-tip, red curves correspond to the residual strains at the end of heating stages and the blue curves correspond to the total axial strain at the end of cooling stages

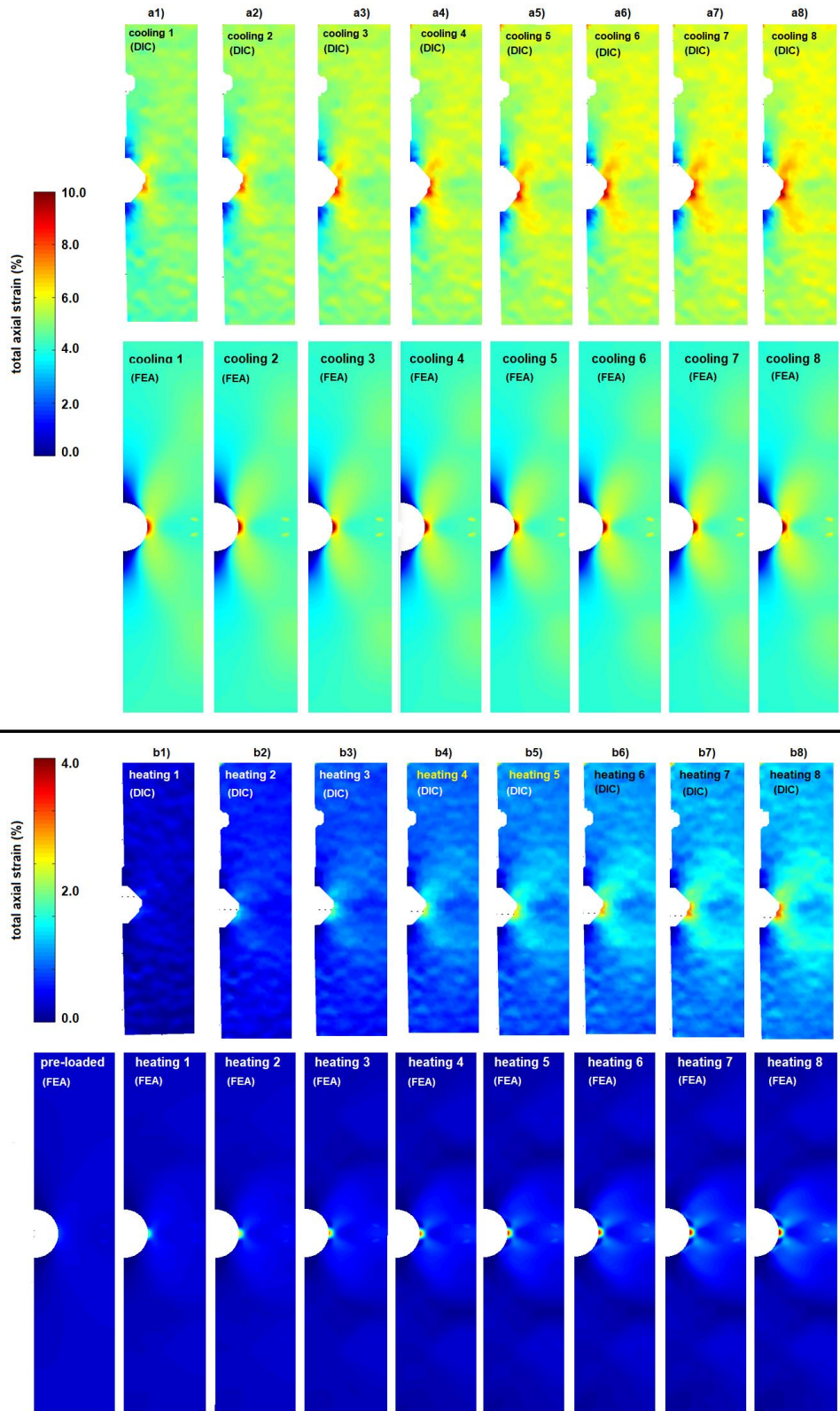


Fig. 6-9 numerical predictions: (a1-a8) the spatial evolution of total axial strain at the end of cooling stages over the 8 thermal cycles obtained from DIC measurements (at the top) and by FE analyses (at the bottom); (b1-b8) the spatial evolution of total axial strain at the preloaded stage and the end of subsequent heating stages over the 8 thermal cycles obtained from DIC measurements (at the top) and by FE analyses (at the bottom)

Fig. 6-10a,c show the numerically derived distribution of axial and transverse stresses ahead of the notch-tip at the end of cooling, respectively, which remain unchanged upon the subsequent cooling stages since the maximum notch-tip axial stress at cooling reaches the yield stress of martensite. Fig. 6-10b depicts the stress distribution at the notch-tip ligament in the preloaded state (black curve) and its changes over the following heating stages. As it is seen the compressive stresses gradually increase at the notch-tip and its very close vicinity. The stress state at the notch-tip turns to a tensile stress state immediately within the SRiZ; the maximum tensile stress is reached at the border of the SRiZ and SReZ, then it reduces sharply in SReZ till it saturates to the nominal stress value at the middle of the notch-tip ligament (Fig. 6-10b). The maxima of the axial stress coincide with the maxima of transverse stress, consistently at the end of both cooling and heating stages (see Fig. 6-10c and Fig. 6-10d, respectively). As explained before, these maxima are due to the Poisson effect caused by MT-induced large strains in SRiZ. Hence, local maxima in transverse stress split the ligament into SRiZ and SReZ.

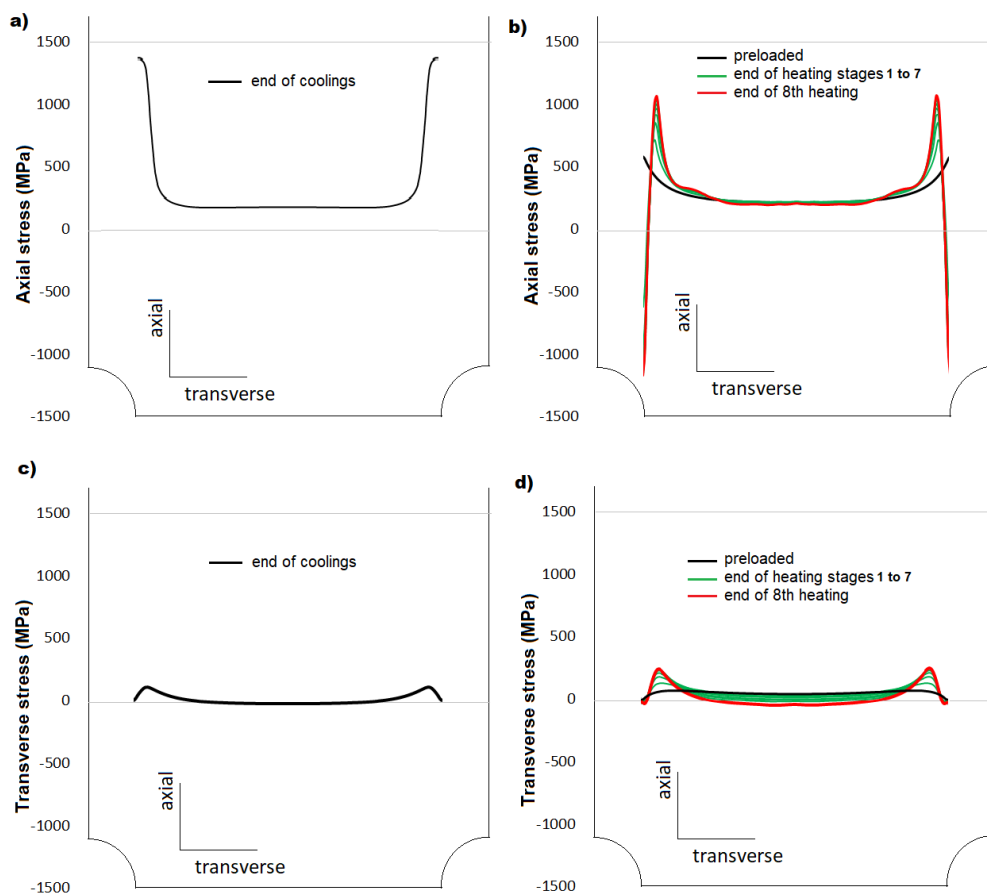


Fig. 6-10 The FE results: a) distribution of the axial stress within the notch-tip ligament at the end of cooling; (b) the evolution of the distribution of the axial stress within the notch-tip ligament at the end of heating stages over the 8 cycles; (c) distribution of the transverse stress within the notch-tip ligament at the end of the cooling

Fig. 6-11b1-b8, Fig. 6-11a1-a8, and Fig. 6-11c1-c8, respectively, represent the evolutions of plastic deformations at the end of cooling stages, compressive stresses at the end of heating, and the remnant (compression-induced) martensite around the notch-tip at the end of heating stages, over the 8 thermal cycles obtained from numerical predictions. The accumulation of plastic strains at the notch-tip during cooling (where the maximum stress is reached at the notch-tip) results in the gradual increase of the compressive stresses (as also discussed above, in Fig. 6-10b) and the zone under compression around

the notch (see colormaps in Fig. 6-11a1-a8); thus, accumulation of remnant (compression-induced) martensite volume fractions (see colormaps in Fig. 6-11c1-c8) at the end of heating stages. As it is seen in Fig. 6-11c1-c8, the compression-induced remnant martensite evolve from the third cycle (where it extends to 0.004 mm from the notch-tip) and gradually accumulate till it extends to 0.125mm distance from the notch-tip at the end of the 8th heating stage. Further, the direction of the propagation of the plastic zone and residual martensite complies with the direction of the MT-band (maximum shear stress) (Fig. 6-11).

Conclusions

The role of plasticity was experimentally and numerically evaluated in the cyclic evolution of martensitic transformation (MT) and mechanical fields around the notch in a thin shape memory NiTi ribbon including two-sided semi-circular notches. The resulting numerical results satisfactorily describe the notch-induced localization of the martensite transformation and the plasticity which affects its reversibility upon thermal cycles under a constant force loading constraint. The results reveal that: i) the stress at the notch-tip reaches its maximum in the martensite phase during the forward MT upon cooling; which means that the stress concentration is amplified by the forward MT, ii) the stress concentration amplification is due to stress-riser induced inhomogeneous MT and accompanying transformation strain, iii) the plastic deformation of martensite turns in reduction of the effective maximum stress during cooling; thus, it decreases the stress concentration amplification triggered by forward MT, iv) the plastic strains evolve in cooling at the notch-tip area results in compressive stresses in heating stage, where the elastically transformed bulk ligament tends to return to its original configuration by the reverse MT ($M \rightarrow A$) by heating, v) the compression induced on the notch-tip area during heating may turn to a secondary phase transformation at the notch-tip, whenever the value of which exceeds the transformation stress plateau; thus, a double phase transition occurs at the subsequent cooling and heating stages at the notch-tip, vi) the plastic strains gradually accumulate over the repeated cooling cycles, resulting in higher compressive stresses in heating stages; thus, accumulation of remnant (compression-induced) martensite at the end of heating stages.

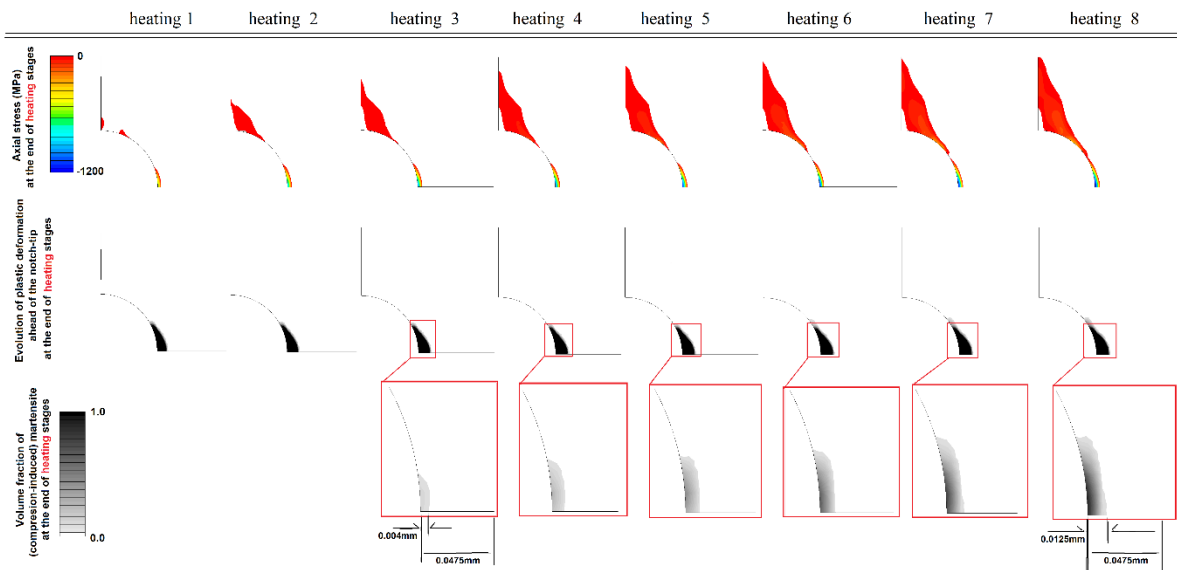


Fig. 6-11 Numerical predictions: (a1-a8) the evolution of compressive stresses at the notch-tip vicinity, induced by accumulation of plastic strains upon cooling stages as depicted in (b1-b8); (c1-c8) the accumulation of compression-induced (remnant) martensite volume fraction over the 8 heating stages.

CHAPTER 7. NiTi Actuators with Stress Risers: Role of Bias Load and Actuation Temperature

7.1. Introduction

NiTi thin elements (wires, ribbons) are widely used in shape memory actuators undergoing repeated thermal cycles under an external force. The NiTi actuators work either under a constant force (CF loading constraint) from a dead weight or they operate against a variable force (VF loading constraint) from an elastic bias spring. The commercially available shape memory alloy wires/ribbons have initial microscopic defects; such as voids, inclusions, and cavities that may potentially act as stress risers (stress concentrators). Joints of the SMA element with other parts in the actuator mechanism would play the role of stress risers, as well. Even in hypothetically perfect medical grade NiTi elements, voids that form at second particles in the very beginnings of cyclic loading can act as stress risers, where the fatigue cracks initiate. Despite their significant effects on actuation performance, the stress risers and their interaction with martensitic transformation and redistribution of mechanical gradients upon thermomechanical cyclic loading have not been studied thoroughly yet.

This issue is studied in the present chapter through finite element analyses of the effects of actuation load type (CF and VF), the stiffness of the bias spring –in the case of VF–, and the maximum temperature (reached upon heating) on the local evolution of martensitic phase transformation and stress/strain fields around the notch during the cyclic thermomechanical loading of a thin NiTi shape memory notched thin ribbon. In all simulations, the ribbon is preloaded in austenite and subjected to the following cooling-heating cycle. To analyze the effect of the bias spring's stiffness, two different spring's stiffnesses are examined in the VF case: $K_{spring} = 100\text{N/mm}$ and $K_{spring} = 20\text{N/mm}$. The level of preload is similar in all simulations (inducing 185MPa nominal stress), and the minimum temperature reached upon cooling is low enough to ensure that the whole structure turns to detwinned martensite. To investigate the effects of the overheating, the cycling under VF loading ($k=20\text{ N/mm}$) is performed in two heating methods:

- by heating only to the onset of completion of reverse transformation ($M \rightarrow A$) in bulk (A_f^{bulk}), while leaving the notch area in the martensite state
- by overheating to the completion of reverse transformation ($M \rightarrow A$) in the entire ribbon, including the notch area

The results show that:

- i. forward martensitic transformation upon cooling has a strong amplification effect on the notch stress concentration factor.
- ii. the evolution of the forward martensitic transformation during cooling results in a sharp stress peak at the notch-tip, the magnitude of which depends on the stiffness of the bias spring; and by heating the notch-tip stress relaxes due to the reverse phase transformation of the surrounding bulk
- iii. overheating during the actuation is unfavorable and harmful to the notch-tip since the complete reverse phase transformation at the notch-tip has a stress rising effect, while incomplete reverse phase transformation at the notch-tip has a stress relaxing effect.

The work corresponding to this chapter has been published as:

Pejman Shayanfard, Luděk Heller, Pavel Šandera, Petr Šittner, Numerical Analysis of NiTi Actuators with Stress Risers: the Role of Bias Load and Actuation Temperature, Engineering Fracture Mechanics, Volume 244, 1 March 2021, 107551, Doi: <https://doi.org/10.1016/j.engfracmech.2021.107551>

and is attached to the end of the thesis.

The paper presents a purely numerical analysis that was, however, inspired by questions raised by related experimental research work, discussed in CHAPTER 6. The part, which is the original work of the author of this dissertation, presents in the cited paper is the analysis primary idea, the processing of all finite element simulations and post-processing of the results, comparison and interpretation of the results and writing the manuscript which was revised thoroughly after comprehensive consultations with coauthors.

CHAPTER 8. NiTi self-expanding stents: A Finite Element Analysis

8.1. Introduction

As the population ages, the superficial femoral and popliteal arteries are the prevalent locations for peripheral arterial disease (Fig. 8-1). A typical symptom in such cases is claudication when a single arterial level is involved. Critical limb ischemia (CLI) is more usual when the femoral disease is part of a multilevel obstructive process. Such cases often require percutaneous transluminal angioplasty followed by stenting to restore vessel patency and blood flow[245]. However, endovascular revascularization of the femoropopliteal (FP) artery has been limited by high rates of restenosis and stent fracture. The unique physical forces that are applied to the FP artery during cyclic leg movement have been blamed to be the source of problems.

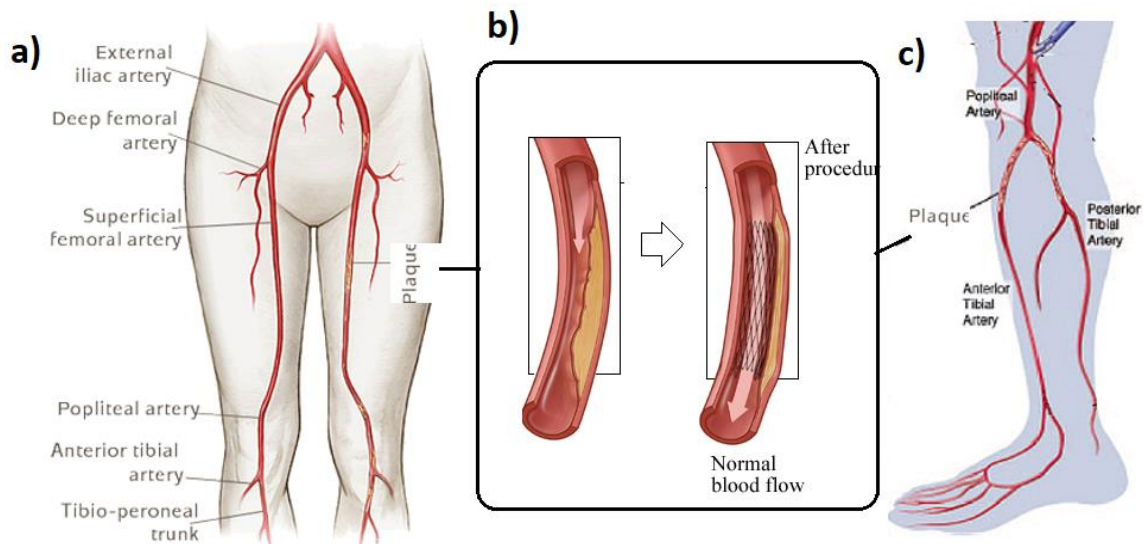


Fig. 8-1 occlusion of (a) superficial femoral, and (c) popliteal artery, (b) restored by the deployment of self-expanding Nitinol stents

Because of extended deformability allowing for minimally invasive deployment and their functional properties, the superelastic Nitinol stents seem to be superior for deployment in regions of torsion and flexion such as the popliteal and superficial femoral artery, in contrast to the undesirable results reported with balloon-expandable stainless steel stents [246,247]. Nevertheless, the clinical investigations have revealed a significant rate of stent fractures, while stent manufacturers and the FDA are attempting to predict which design types of nitinol stents will fracture in what settings.

The stent fracture phenomena could occur due to several reasons including –but not limited to– design and structural properties of the stent and their mechanical response to the deployment loads and the cyclic loads applied due to the operating conditions into the vessel –induced by heart pulsation–. Such that, the stent design could have determining effects on the local stresses and strains under different loading conditions. Stent fracture could lead to several injuries such as re-occlusion and Pseudoaneurysm phenomena. The stent fracture could happen in several modes:

- mode I, which involves only a single strut

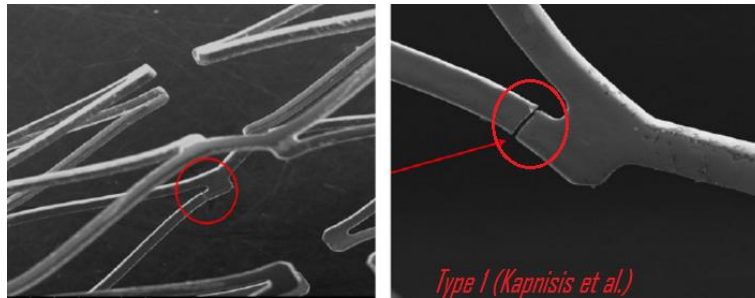


Fig. 8-2 Single strut fracture of an overlapping Nitinol stent, mode I stent fracture [248]

- mode II, which involves multiple struts that can occur at different sites

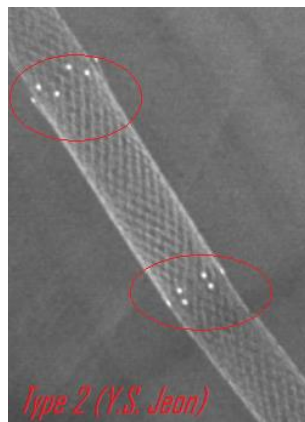


Fig. 8-3 Follow-up X-ray showed multiple fractures of stent struts (mode II stent fracture) [249]

- mode III: Involves multiple strut fractures resulting in a complete transverse fracture without displacement
- mode IV: results in a complete transverse linear fracture with stent displacement
- mode V: Spiral fracture: Complete transverse stent fracture with abundant movement and displacement of fractured fragments of more than 1 mm

According to the trial and clinical studies, Intracoil and S.M.A.R.T Niti self-expanding stents have been reported to show long-term durability and safety, when treated in the superficial femoral/popliteal arteries. A considerable numerical study has been done to evaluate the mechanical behavior of self-expanding Nitinol stents in the literature, however, limited attention has been paid to the Intracoil stent and its interaction with the artery to analyze why they almost show no evidence of fracture.

In this chapter, the deployment procedure and the mechanical stent-artery interaction are analyzed numerically for both Intracoil and S.M.A.R.T stents (Fig. 8-6).

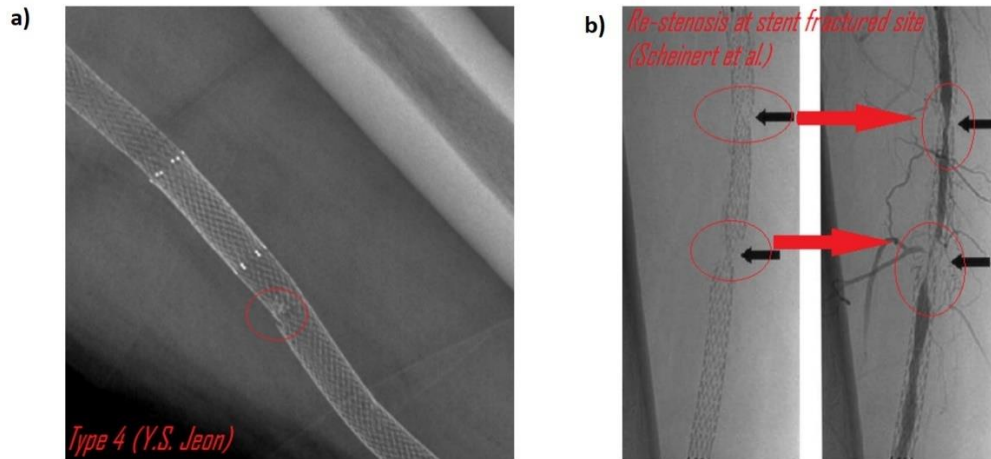


Fig. 8-4 a) Follow-up X-ray showed transverse linear fracture and displacement (mode IV stent fracture) [249]; b) Self-expanding nitinol stent nine months after implantation showing a severe stent fracture in the distal and a moderate stent fracture in the proximal part of the stent [250]



Fig. 8-5 A case of mode 5 stent fracture (red arrow, left) corresponding to pseudoaneurysm (red arrow, right) of the SF artery [251]

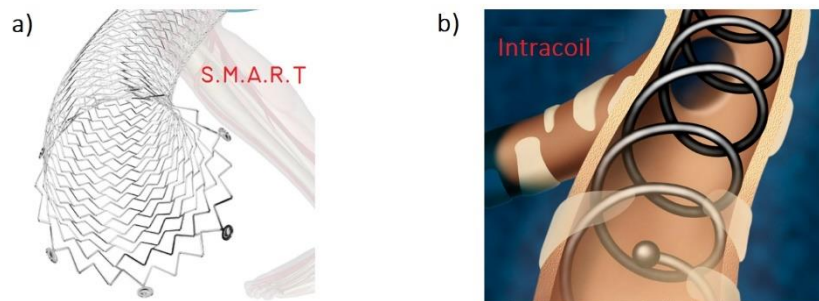


Fig. 8-6 a) S.M.A.R.T NiTi stent; b) Intracoil NiTi stent

8.2. Materials and Methods

The finite element software ANSYS15 APDL is used, in which the material option for superelasticity is based on the SMA model developed by Auricchio et al. [252]. Material parameters of medical graded Nitinol SE508 (Table 8-1, Fig. 8-7)) are chosen [253]. The vessel and plaque are regarded as

hyperelastic materials and modeled using six-parameter Mooney–Rivlin hyperelastic constitutive equations, for which the material parameters are derived in Ref. [253] (Table 8-1). The models are meshed with eight-node Solid185 break elements. Flexible–flexible surface-to-nodes contact is defined between the stent’s outer surface and the inner surface of the plaque, by high order target elements. The Augmented Lagrange contact algorithm is set with automatic pinball calculation and using the full Newton-Raphson method.

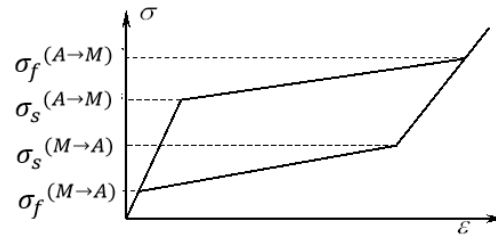


Fig. 8-7 Schematic of the stress-strain response of Superelastic material

Table 8-1 Material parameters of the stent and the tissue used in ANSYS

Stent’s material properties (MPa)				Artery and Plaque material properties							
$\sigma_s^{A \rightarrow M}$	$\sigma_f^{A \rightarrow M}$	$\sigma_s^{M \rightarrow A}$	$\sigma_f^{M \rightarrow A}$	ϵ^*	α	C_1	C_2	C_3	C_4	C_5	C_6
346	365	83	57	0.063	0.09	-0.452	0.51	0.101	1.256	0.0	0.301

Table 8-2 The 3D ANSYS model dimensions

Intracoil model		S.M.A.R.T model			
	Model length	22.40 mm	Strut height	3.19 mm	
	Stent wire diameter	0.15 mm	Strut repeating	12 per ring	
	Stent mean diameter	6.85 mm	Strut thickness	0.22 mm	
	Stent pitch	1.8 mm	Strut width	0.1 mm	
			No. of Bridges at per connection	4 in 360 degree	
	Inner diameter	7 mm	Model Length	13.14 mm	
Artery	Wall thickness	0.5 mm			
	Stenosis- Stenosis length	26.53%- 24.62 mm	Artery	Inner diameter	7 mm
				Wall thickness	0.5 mm
				Stenosis- Stenosis length	26.53%- 13.15mm

8.2.1. Models and Geometry

For the Intracoil stent design, it was found [254] that the difference between the minimum stent’s coil diameter and the inner diameter of the targeted artery has not to be larger than 1mm (see Fig. 8-8b), to avoid the danger of collapse or leaning coils. The Intracoil is available in diameters as large as 8 mm and lengths as long as 60 mm. S.M.A.R.T Nitinol stents are composed of a series of V-shaped struts in circumferential rows that are connected by bridges. Fewer bridges between zigzags make the stent design more open and flexible. The peak-to-peak connection is the original and most common form of bridge connection, though alternatives are not uncommon. Peak-to-valley, valley-to-valley, and mid-strut connections require some circumferential material to be sacrificed from the struts, forcing a compromise in strength or profile. With peak-to-peak connections, however, no circumferential material is sacrificed. In the design of NiTi stents, it is usually imperative to maximize the strength of the design, which explains the nearly exclusive use of pick-to-pick connection strategy in self-expanding stents in the survey, such that in the present study (see Fig. 8-9a and Fig. 8-9b).

Due to symmetry concerns, only half of the S.M.A.R.T stent is modeled (see Fig. 8-9a). A summary of models' dimensions/sizes is presented in Table 8-2, for both modeled stents.

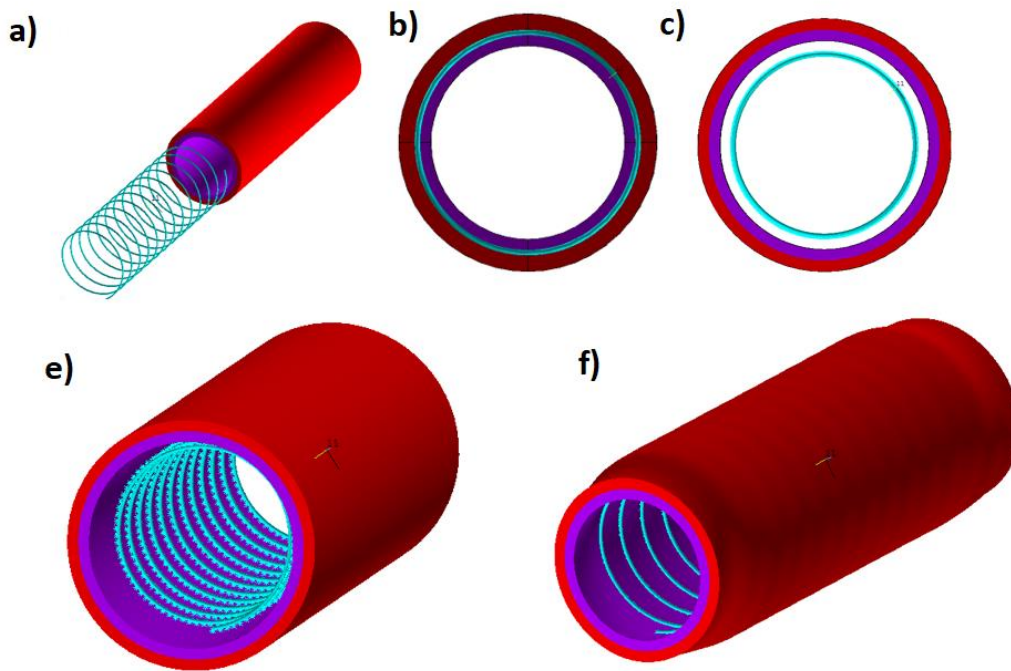


Fig. 8-8 Intracoil NiTi self-expanding stent: a) full model with artery and the plaque, b) the inner coil diameter is 1 mm larger than the inner diameter of the artery in the plaque-induced-closed site, c) the artery is expanded by internal pressure, e) the stent is moved towards the deployment site, f) the internal pressure is released and the stent-plaque contact applies

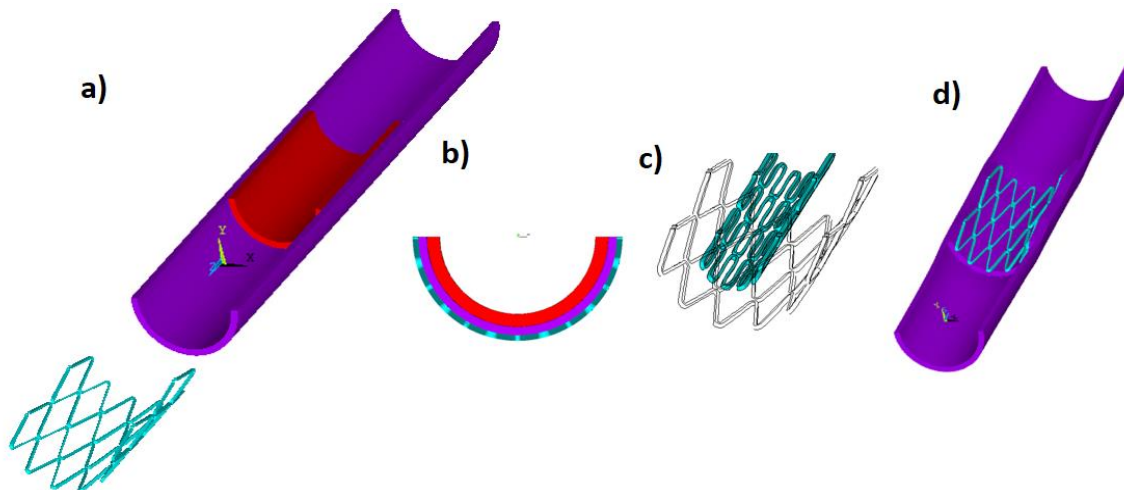


Fig. 8-9 S.M.A.R.T stent, a) the half-model of the stent with the artery and the plaque, b) the outer diameter of the original stent is equal to the outer diameter of the artery, c) the stent is crimped, d) the stent is moved towards the deployment site and the radial constraint is released and the stent-plaque contact applies

8.2.2. Boundary conditions

S.M.A.R.T stent:

i) A uniform spatial radial displacement boundary condition on the outer surface was used to crimp the stent (see Fig. 8-9c)

ii) the stent is moved towards the target lesion by an axial displacement applied to the artery (see Fig. 8-9d)

iii) the crimped stent is allowed to gradually expand till contact is established between the stent and the plaque.

Intracoil stent:

In general, due to forward ($A \rightarrow M$) phase transformation taking place during the crimping stage of the deployment procedure, this stage has to be involved in finite element analysis. However, for the Intracoil model, in this study, it was seen that the maximum induced stresses are lower than $\sigma_f^{(A \rightarrow M)}$, i.e. the whole structure returns to the elastic austenite state after the deployment; thus, there would not be any numerical miscalculation in the simulations if we neglect the complicated, time-consuming crimping stage of the Intracoil model. Accordingly, the artery is expanded by applying pressure (0.15 MPa) on the inner surface of the plaque, such that, it expands to a larger diameter than that of the outer coil diameter of the stent (see Fig. 8-8c). Then, the stent is moved towards the targeted site (see Fig. 8-8e) and the pressure is gradually released from the inner surface of the artery allowing the contact interaction with the stent (see Fig. 8-8f).

8.3. Results and discussion

In general, since the stress state within the stent parts is not homogeneous upon loading-unloading-pulsation, several loading path scenarios can be reached at different sites of a self-expanding stent. Examples are shown in Fig. 8-10 denoted by modes I to V:

- **mode I:** the material remains in elastic austenite at the maximum load, i.e. in the crimping stage. Thus, upon extending and subsequent pulsation fatigue load the material would be cyclically loaded in elastic austenite.
- **mode II:** The material partially transforms into martensite in the crimping stage ($A \rightarrow M+A$), it partially reversely transforms to austenite ($A+M \rightarrow M+A$) and undergoes partial martensitic transformation under the pulsation fatigue load. It means that upon fatigue loading there are mobile band fronts (MBFs) in the zone.
- **Mode III:** similar to mode II, however, the material is cyclically loaded without martensitic transformation, i.e. no mobile band fronts (MBFs) upon fatigue loading.
- **Mode IV:** the material is partially transformed in the crimping stage ($A \rightarrow A+M$), but the stress levels do not reach the reverse plateau stresses. Such that, under the pulsation load the material is elastically loaded without undergoing martensitic transformation, i.e. no MBFs
- **Mode V:** the maximum stress in the crimping stage is high enough to complete forward phase transformation ($A \rightarrow M$), upon self-expanding stage the stresses either reach or not to the

reverse plateau stresses, and the subsequent pulsation fatigue load leads to an elastic cyclic deformation without martensitic transformation involved (no MBFs)

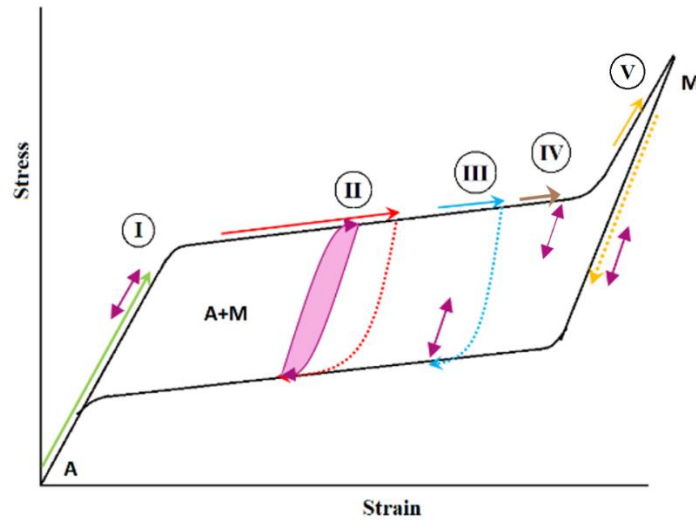


Fig. 8-10 The potentially load-paths applied at different sites of the S.M.A.R.T stent upon the crimping-extension-pulsation procedure. The crimping load are shown in solid arrows, the unloading paths are shown by dashed arrows and the pulsation cyclic load are shown in purple loops

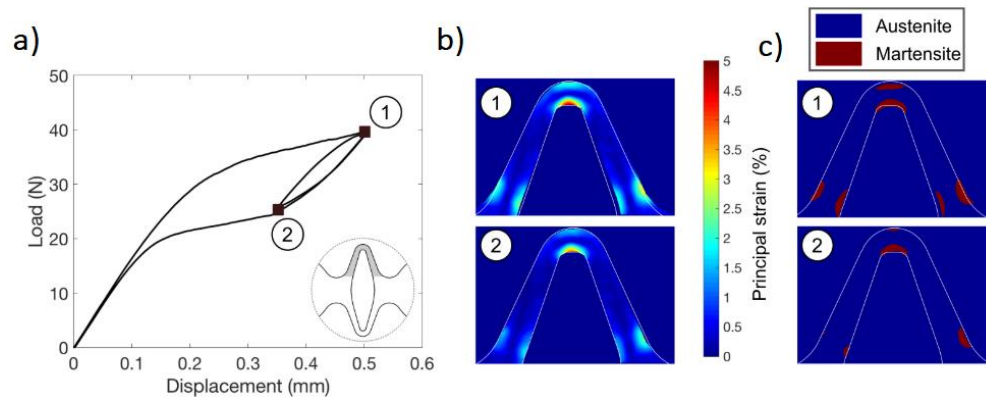


Fig. 8-11 a) Force-displacement curve for a high-purity diamond specimen; b) Principal strain field in the gage from DIC; c) the martensite and austenite regions corresponding to points 1 and 2, redrawn from [255]

The motion of martensite band fronts (MBFs) is a key mechanism for the accumulation of damage upon the fatigue loading of NiTi. It means that a larger motion of martensite band fronts results in a larger accumulation of defects, which turns into a shorter low-cycle fatigue life. In this regard, as it was discussed in section 1.1 under the uniaxial tensile fatigue loading, when the MBFs are involved in the cyclic deformation (mode II in Fig. 8-10) the larger the strain amplitude leads to shorter fatigue life. Further, it is known that among the modes in which the MBFs are not incorporated into the deformation mechanism mode I (Fig. 8-10) is the safest fatigue mode, while the unloading martensite (mode V in Fig. 8-10) is more prone to fatigue with respect to the loading martensite (mode IV in Fig. 8-10) [17]. Relatively similar remarks were outlined by Paranjape et al. [255]. Paranjape et al. [255] analyzed the correlation between the transformation volume amplitude and the fatigue life under both uniaxial (thin superelastic NiTi dog bone samples) and bending (thin NiTi diamond samples) fatigue loading conditions, where they defined the phase transformation volume as the

product of the transformed area –between the max load (point 1 Fig. 8-11a) and min load (point 1 Fig. 8-11b)– and the specimen thickness.

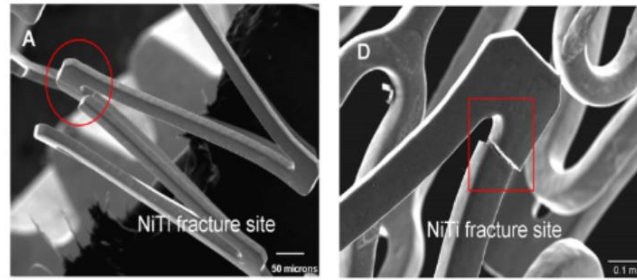


Fig. 8-12 Single strut fracture of a Nitinol stent [248]

Fig. 8-13 represents the finite element results for the S.M.A.R.T stent. Fig. 8-13a and Fig. 8-13b respectively indicate the first principle stress and Von Mises stress induced on the inner wall of the artery in stenosis place. In Fig. 8-13c the distribution of the Von Mises stress in the stent is seen after the crimping stage. The gray color in Fig. 8-13c represent exceeding the stress from the plateau stress, i.e. the completion of the $A \rightarrow M$ phase transformation. The partially transformed $A \rightarrow M$ zones are illustrated in Fig. 8-13d. The fatigue response can be mimicked by comparing the stress state in the unloaded (expansion of the stent into the vessel) state shown in Fig. 8-13e and after the crimping stage. As it is seen in Fig. 8-13c and Fig. 8-13d upon the crimping stage and subsequent unloading –due to self-expansion inside the artery– (Fig. 8-13e) all fatigue load modes **I** to **V** (discussed above) exist within the stent. The most critical parts are illustrated Fig. 8-13d and Fig. 8-13f where the material may undergo either mode **II** to **IV** of cyclic loading modes where the material is prone to fatigue failure. These results agree with the clinical observations of the fatigue fracture of stents with a similar design (Fig. 8-12) [248]. The maximum Von Mises equivalent stress for the Intracoil (Fig. 8-14) stent lies at the elastic regime since the material returned to the full austenite phase (Fig. 8-14) in the whole structure. This decreases the danger of preliminary fatigue failure of the implanted Intracoil stent.

The results predicted patency restoration to the stenosed artery, and the lumen diameter was increased from 6 mm to 6.54 mm (~52.13%) and from 6 mm to 6.94 mm (~95.5%) for S.M.A.R.T and INTRACOIL, respectively. The resultant Von Mises stress on the artery inner wall was ~0.22 MPa and ~0.42 MPa for S.M.A.R.T (Fig. 8-13b) and Intracoil (Fig. 8-14c), respectively. Consequently, even though the Intracoil stent has an equal thickness to the S.M.A.R.T and a smaller outer diameter, it shows superior patency restoration. On the other hand, the small pitch considered in the Intracoil design prevents a high level of tissue prolapse in contrast to the S.M.A.R.T stent. On the contrary, the higher level of the resultant Von Mises on the artery inner wall, besides a little higher tissue prolapse, makes the Intracoil less potential to move from the deployed site.

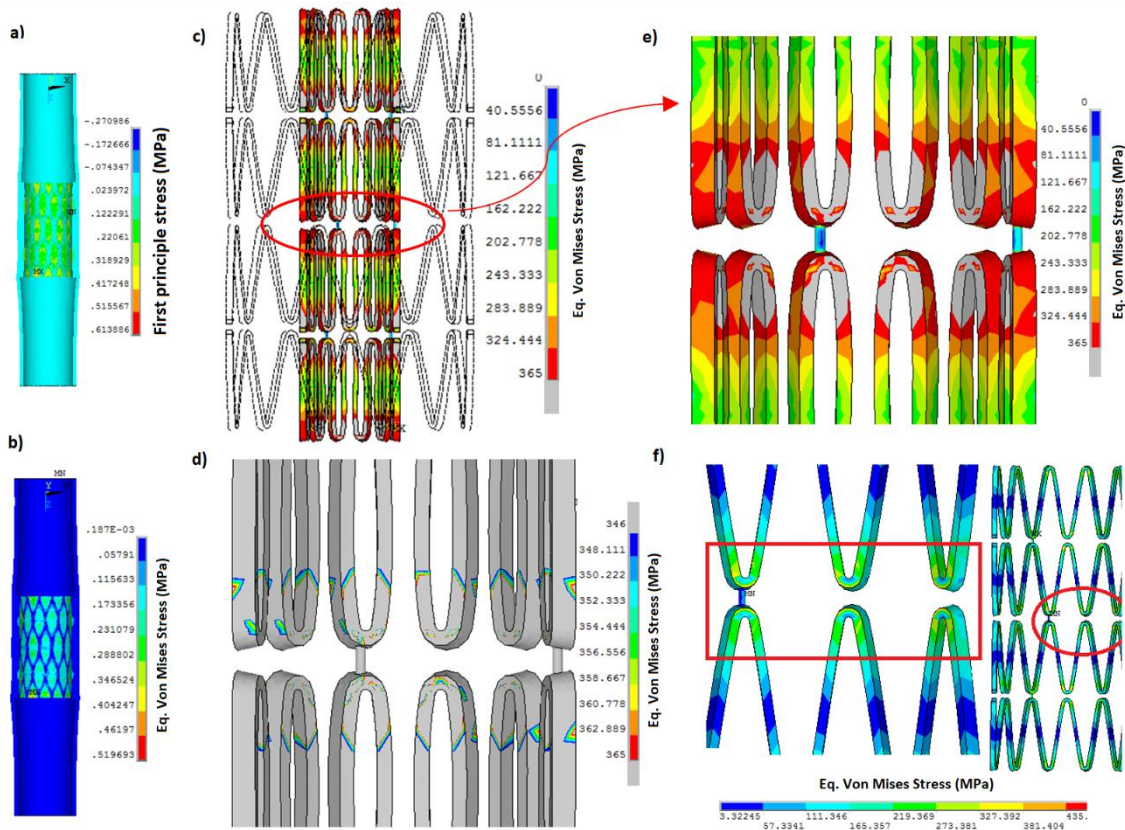


Fig. 8-13 Finite element results for the SMART stent f; a,b) the first principle and Von Mises stress on the stenotic tissue, respectively; c) Von Mises stress distribution in the crimped state, gray zones represent the stresses beyond the plateau stress (i.e. completion of the forward $A \rightarrow M$ transformation); d) the zones at which the stress is in plateau stress range (i.e. partially transformed regions); e) magnified of the gray zones shown in Fig. 8-13c; f) the Von Mises stress distribution after the stent is extended inside the artery

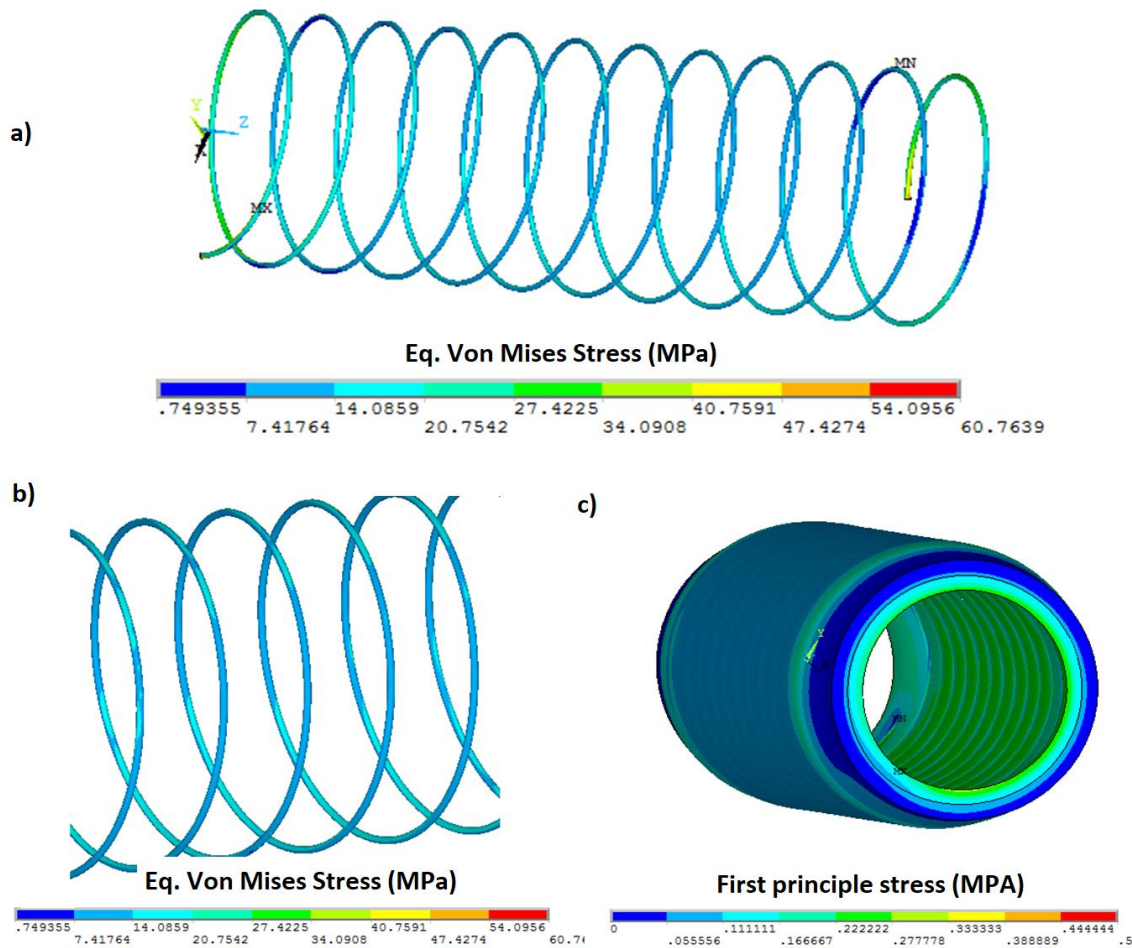


Fig. 8-14 Finite element results for the Intracoil NiTi self-expanding stent: a) Von Mises stress distribution on the stent after completion of the deployment; b) Von Mises stress distribution after removing the elements near the applied BCs site; c) first principle stress distribution on the artery and plaque tissue,

8.4. Conclusions

Delivery of the Intracoil and s.m.a.r.t self-expanding superelastic Nitinol stents and their release inside a stenotic site of the artery was numerically analyzed. Intracoil was successful in ~95.5% restoring patency to the stenosed artery, s.m.a.r.t resolved only ~52.13% of the artery closure. It was observed that the maximum stress for the Intracoil stent remains in the elastic regime, which decreases the danger of preliminary fatigue failure of the implanted Intracoil stent. However, in the case of the s.m.a.r.t stent, some regions of the structure remain in a partially transformed state, where the mechanical fatigue failure is expected under the blood pulsation induced fatigue load.

REFERENCES

- [1] J. Morais, P.G. De Morais, C. Santos, A.C. Costa, P. Candeias, Shape Memory Alloy Based Dampers for Earthquake Response Mitigation, *Procedia Struct. Integr.* 5 (2017) 705–712. <https://doi.org/10.1016/j.prostr.2017.07.048>.
- [2] L. Petrini, F. Migliavacca, Biomedical Applications of Shape Memory Alloys, *J. Metall.* 2011 (2011) 1–15. <https://doi.org/10.1155/2011/501483>.
- [3] D. Stoeckel, A. Pelton, T. Duerig, Self-expanding Nitinol stents: Material and design considerations, *Eur. Radiol.* 14 (2004) 292–301. <https://doi.org/10.1007/s00330-003-2022-5>.
- [4] L.C. Brinson, I. Schmidt, R. Lammring, Stress-induced transformation behavior of a polycrystalline NiTi shape memory alloy : micro and macromechanical investigations via in situ optical microscopy, 52 (2004) 1549–1571. <https://doi.org/10.1016/j.jmps.2004.01.001>.
- [5] D. Broek, *Elementary engineering fracture mechanics*, Springer Netherlands, Dordrecht, 1986. <https://doi.org/10.1007/978-94-009-4333-9>.
- [6] S. Daly, G. Ravichandran, K. Bhattacharya, Stress-induced martensitic phase transformation in thin sheets of Nitinol, *Acta Mater.* (2007). <https://doi.org/10.1016/j.actamat.2007.02.011>.
- [7] J.A. Shaw, S. Kyriakides, Initiation and Propagation of Localized Deformation in the Pseudoelastic Response of {N}i{T}i, *Proc. SPIE Symp. Smart Struct. Mater.* 13 (1998) 837–871. <https://doi.org/10.1117/12.316850>.
- [8] T.A. Sawaguchi, G. Kasträter, A. Yawny, M. Wagner, G. Eggeler, Crack initiation and propagation in 50.9 at. pct Ni-Ti pseudoelastic shape-memory wires in bending-rotation fatigue, *Metall. Mater. Trans. A.* (2003). <https://doi.org/10.1007/s11661-003-0186-x>.
- [9] K.E. Perry, A. Teiche, Fatigue Crack Initiation in Superelastic Nitinol, *Fatigue Fract. Met. Med. Mater. Devices.* (2013) 35–52. <https://doi.org/10.1520/STP155920130030>.
- [10] E. Sgambitterra, C. Maletta, F. Furgiuele, Investigation on Crack Tip Transformation in NiTi Alloys: Effect of the Temperature, *Shape Mem. Superelasticity.* (2015). <https://doi.org/10.1007/s40830-015-0018-z>.
- [11] S.W. Robertson, A.R. Pelton, R.O. Ritchie, Mechanical fatigue and fracture of Nitinol, *Int. Mater. Rev.* 57 (2012) 1–37. <https://doi.org/10.1179/1743280411Y.0000000009>.
- [12] A.L. Mckelvey, R.O. Ritchie, Fatigue-crack propagation in Nitinol, a shape-memory and superelastic endovascular stent material, *J Biomed Mater Res.* 47 (1999) 301–308.
- [13] M.F.X. Wagner, N. Nayan, U. Ramamurty, Healing of fatigue damage in NiTi shape memory alloys, *J. Phys. D. Appl. Phys.* 41 (2008). <https://doi.org/10.1088/0022-3727/41/18/185408>.
- [14] G. Kang, D. Song, Review on structural fatigue of NiTi shape memory alloys: Pure mechanical and thermo-mechanical ones, *Theor. Appl. Mech. Lett.* 5 (2015) 245–254. <https://doi.org/10.1016/j.taml.2015.11.004>.
- [15] J.A. Shaw, S. Kyriakides, THERMOMECHANICAL ASPECTS OF NiTi, 43 (1995) 1243–1281.
- [16] J.A. Shaw, S. Kyriakides, ON THE NUCLEATION AND PROPAGATION OF PHASE TRANSFORMATION FRONTS IN A NiTi ALLOY, 45 (1997) 683–700.
- [17] L. Zheng, Y. He, Z. Moumni, Lüders-like band front motion and fatigue life of pseudoelastic polycrystalline NiTi shape memory alloy, *SMM.* 123 (2016) 46–50. <https://doi.org/10.1016/j.scriptamat.2016.05.042>.
- [18] X. Zhang, P. Feng, Y. He, T. Yu, Q. Sun, Experimental study on rate dependence of macroscopic domain and stress hysteresis in NiTi shape memory alloy strips, *Int. J. Mech. Sci.* 52 (2010) 1660–1670. <https://doi.org/10.1016/j.ijmecsci.2010.08.007>.
- [19] P. Sittner, Y. Liu, V. Novak, On the origin of Lüders-like deformation of NiTi shape memory alloys, *J. Mech. Phys. Solids.* 53 (2005) 1719–1746. <https://doi.org/10.1016/j.jmps.2005.03.005>.
- [20] Y. Chen, O. Tyc, L. Kadeřávek, O. Molnárová, L. Heller, P. Šittner, Temperature and microstructure dependence of localized tensile deformation of superelastic NiTi wires, *Mater. Des.* 174 (2019). <https://doi.org/10.1016/j.matdes.2019.107797>.
- [21] Y.J. He, Q.P. Sun, Rate-dependent domain spacing in a stretched NiTi strip, *Int. J. Solids Struct.* 47 (2010) 2775–2783. <https://doi.org/10.1016/j.ijsolstr.2010.06.006>.
- [22] E. Hornbogen, G. Eggeler, Surface aspects in fatigue of Shape Memory Alloys (SMA), *Materwiss. Werksttech.* 35 (2004) 255–259. <https://doi.org/10.1002/mawe.200400759>.
- [23] S.W. Robertson, A.R. Pelton, R.O. Ritchie, Mechanical fatigue and fracture of Nitinol, *Int. Mater. Rev.* (2012). <https://doi.org/10.1179/1743280411Y.0000000009>.
- [24] P. Shayanfard, L. Heller, D. Dostálová, E. Alarcon, M. Frost, P. Sedlák, P. Šandera, P. Šittner, J. Pokluda, J. Horníková, EFFECT OF MARTENSITIC TRANSFORMATION ON LOCAL STRESSES AND STRAINS AT A NOTCH OF CYCLICALLY LOADED SUPERELASTIC NITI RIBBON, (n.d.).
- [25] P. Shayanfard, P. Sittner, L. Heller, P. Sandera, Finite Element Analysis on the Effect of Martensitic Transformation and Plastic Deformation on the Stress Concentration Factor in a Thin Notched Superelastic NiTi Ribbon, *Funct. Mater. Lett.* 13 (2020) 2051028.
- [26] Y. Wu, A. Ojha, L. Patriarca, H. Sehitoglu, Fatigue Crack Growth Fundamentals in Shape Memory Alloys, *Shape Mem. Superelasticity.* 1 (2015) 18–40. <https://doi.org/10.1007/s40830-015-0005-4>.
- [27] M. K. N. MERCIER, O., Fatigue of NiTi thermoelastic martensites, *Mater. Sci. Eng. A273-275* (19998) 134–148.
- [28] T. Baxevanis, A.F. Parrinello, D.C. Lagoudas, On the driving force for crack growth during thermal actuation of

- shape memory alloys, *J. Mech. Phys. Solids*. 89 (2016) 255–271. <https://doi.org/10.1016/j.jmps.2015.12.011>.
- [29] C.N. Saikrishna, K. V. Ramaiah, J. Bhagyaraj, Gouthama, S.K. Bhaumik, Influence of stored elastic strain energy on fatigue behaviour of NiTi shape memory alloy thermal actuator wire, *Mater. Sci. Eng. A*. 587 (2013) 65–71. <https://doi.org/10.1016/j.msea.2013.08.048>.
- [30] S.W. Robertson, A.R. Pelton, R.O. Ritchie, S.W. Robertson, A.R. Pelton, R.O. Ritchie, Mechanical fatigue and fracture of Nitinol Mechanical fatigue and fracture of Nitinol, 6608 (2013). <https://doi.org/10.1179/1743280411Y.0000000009>.
- [31] B. Malard, J. Pilch, P. Sittner, R. Delville, C. Curfs, In situ investigation of the fast microstructure evolution during electropulse treatment of cold drawn NiTi wires, *Acta Mater.* 59 (2020) 1542–1556. <https://doi.org/10.1016/j.actamat.2010.11.018>.
- [32] R. Delville, B. Malard, J. Pilch, P. Sittner, D. Schryvers, Microstructure changes during non-conventional heat treatment of thin Ni – Ti wires by pulsed electric current studied by transmission electron microscopy, *Acta Mater.* 58 (2020) 4503–4515. <https://doi.org/10.1016/j.actamat.2010.04.046>.
- [33] P. Šittner, P. Sedlák, H. Seiner, P. Sedmák, J. Pilch, R. Delville, On the coupling between martensitic transformation and plasticity in NiTi : Experiments and continuum based modelling, 98 (2018) 249–298. <https://doi.org/10.1016/j.pmatsci.2018.07.003>.
- [34] L. Heller, H. Seiner, P. Š, P. Sedlák, O. Tyc, L. Kade, On the plastic deformation accompanying cyclic martensitic transformation in thermomechanically loaded NiTi, (2018). <https://doi.org/10.1016/j.ijplas.2018.07.007>.
- [35] P. Sedmák, P. Šittner, J. Pilch, C. Curfs, Instability of cyclic superelastic deformation of NiTi investigated by synchrotron X-ray diffraction, *Acta Mater.* 94 (2015) 257–270. <https://doi.org/10.1016/j.actamat.2015.04.039>.
- [36] D.C. Lagoudas, P.B. Entchev, Modeling of transformation-induced plasticity and its effect on the behavior of porous shape memory alloys . Part I : constitutive model for fully dense SMAs, 36 (2004) 865–892. <https://doi.org/10.1016/j.mechmat.2003.08.006>.
- [37] P. Šittner, L. Heller, P. Sedlák, Y. Chen, O. Tyc, O. Molnárová, L. Kadeřávek, H. Seiner, B2 ⇒ B19' ⇒ B2T Martensitic Transformation as a Mechanism of Plastic Deformation of NiTi, *Shape Mem. Superelasticity*. 5 (2019) 383–396. <https://doi.org/10.1007/s40830-019-00250-5>.
- [38] D. Song, G. Kang, Q. Kan, C. Yu, C. Zhang, The effect of martensite plasticity on the cyclic deformation of super-elastic NiTi shape memory alloy, *Smart Mater. Struct.* 23 (2014). <https://doi.org/10.1088/0964-1726/23/1/015008>.
- [39] B. Strnadep, S. Ohashi, H. Ohtsuka, T. Ishihara, S. Miyazaki, Cyclic stress-strain characteristics of Ti-Ni and Ti-Ni-Cu shape memory alloys, 202 (1995) 148–156.
- [40] R. Delville, B. Malard, J. Pilch, P. Sittner, D. Schryvers, Transmission electron microscopy investigation of dislocation slip during superelastic cycling of Ni-Ti wires, *Int. J. Plast.* 27 (2011) 282–297. <https://doi.org/10.1016/j.ijplas.2010.05.005>.
- [41] Z. Moumni, W. Zaki, H. Maitournam, Cyclic Behavior and Energy Approach to the Fatigue of Shape Memory Alloys, *J. Mech. Mater. Struct.* 4 (2009) 395–411. <https://doi.org/10.2140/jomms.2009.4.395>.
- [42] S. Leclercq, C. LExcellent, A general macroscopic description of the thermomechanical behavior of shape memory alloys, *J. Mech. Phys. Solids*. 44 (1996) 953–957. [https://doi.org/10.1016/0022-5096\(96\)00013-0](https://doi.org/10.1016/0022-5096(96)00013-0).
- [43] E. Patoor, D.C. Lagoudas, P.B. Entchev, L.C. Brinson, X. Gao, Shape memory alloys , Part I : General properties and modeling of single crystals, 38 (2006) 391–429. <https://doi.org/10.1016/j.mechmat.2005.05.027>.
- [44] W. Zaki, Z. Moumni, A three-dimensional model of the thermomechanical behavior of shape memory alloys, *J. Mech. Phys. Solids*. 55 (2007) 2455–2490. <https://doi.org/10.1016/j.jmps.2007.03.012>.
- [45] D. Lagoudas, D. Hartl, Y. Chemisky, L. Machado, P. Popov, Constitutive model for the numerical analysis of phase transformation in polycrystalline shape memory alloys, *Int. J. Plast.* 32–33 (2012) 155–183. <https://doi.org/10.1016/j.ijplas.2011.10.009>.
- [46] S. Materials, R. Mehrabi, M. Kadkhodaei, 3D phenomenological constitutive modeling of shape memory alloys based on microplane theory My IOPscience theory View the table of contents for this issue , or go to the journal homepage for more, (2013). <https://doi.org/10.1088/0964-1726/22/2/025017>.
- [47] R. Mehrabi, M. Kadkhodaei, M.T. Andani, M. Elahinia, Microplane modeling of shape memory alloy tubes under tension, torsion, and proportional tension–torsion loading, *J. Intell. Mater. Syst. Struct.* 26 (2014) 144–155. <https://doi.org/10.1177/1045389X14522532>.
- [48] J. Wang, Z. Moumni, W. Zhang, A thermomechanically coupled finite-strain constitutive model for cyclic pseudoelasticity of polycrystalline shape memory alloys, *Int. J. Plast.* 97 (2017) 194–221. <https://doi.org/10.1016/j.ijplas.2017.06.003>.
- [49] T.J. Lim and D.L. McDowell, Degradation of an Ni-Ti alloy during cyclic loading, *Smart Struct. Mater.* 2189 (1994) 326–341.
- [50] C. LExcellent, S. Leclercq, B. Gabry, G. Bourbon, The two way shape memory effect of shape memory alloys : an experimental study and a phenomenological model, 16 (2000) 1155–1168.
- [51] C. Yu, G. Kang, Q. Kan, D. Song, A micromechanical constitutive model based on crystal plasticity for thermo-mechanical cyclic deformation of NiTi shape memory alloys, *Int. J. Plast.* 44 (2013) 161–191. <https://doi.org/10.1016/j.ijplas.2013.01.001>.
- [52] C. Yu, G. Kang, Q. Kan, Y. Zhu, Rate-dependent cyclic deformation of super-elastic NiTi shape memory alloy : Thermo-mechanical coupled and physical mechanism-based constitutive model, *Int. J. Plast.* 72 (2015) 60–90.

- <https://doi.org/10.1016/j.ijplas.2015.05.011>.
- [53] L. Xu, A. Solomou, A Three-Dimensional Constitutive Modeling for Shape Memory Alloys Considering Two-Way Shape Memory Effect and Transformation-Induced Plasticity, (2019) 1–12. <https://doi.org/10.2514/6.2019-1195>.
- [54] D.J. Hartl, D.C. Lagoudas, Constitutive modeling and structural analysis considering simultaneous phase transformation and plastic yield in shape memory alloys, (2009). <https://doi.org/10.1088/0964-1726/18/10/104017>.
- [55] X.M. Wang, B.X. Xu, Z.F. Yue, Micromechanical modelling of the effect of plastic deformation on the mechanical behaviour in pseudoelastic shape memory alloys, *Int. J. Plast.* 24 (2008) 1307–1332. <https://doi.org/10.1016/j.ijplas.2007.09.006>.
- [56] G. Scalet, F. Niccoli, C. Garion, P. Chiggiato, C. Maletta, Mechanics of Materials A three-dimensional phenomenological model for shape memory alloys including two-way shape memory effect and plasticity, *Mech. Mater.* 136 (2019) 103085. <https://doi.org/10.1016/j.mechmat.2019.103085>.
- [57] S. Choudhry, J.W. Yoon, A General Thermo-Mechanical Shape Memory Alloy Model : Formulation and Applications, *AIP Conf. Proc.* 712 (2004) 1589–1594.
- [58] W.A. Wood, Recent Observations on Fatigue Failure in Metals, in: *Symp. Basic Mech. Fatigue*, ASTM International, West Conshohocken, PA, 1959: pp. 110–121. <https://doi.org/10.1520/STP39313S>.
- [59] S. Miyazaki, SHAPE MEMORY AND RELATED PHENOMENA, *Prog. Mater. Sci.* 36 (1992) 203–224. <https://doi.org/10.1007/s40830-017-0122-3>.
- [60] Kaushik Bhattacharya, Microstructure of Martensite Why it forms and how it gives rise to the shape-memory effect, 2003. <https://doi.org/10.1017/CBO9781107415324.004>.
- [61] K. Otsuka, X. Ren, Physical metallurgy of Ti-Ni-based shape memory alloys, *Prog. Mater. Sci.* 50 (2005) 511–678. <https://doi.org/10.1016/j.pmatsci.2004.10.001>.
- [62] D.C. Lagoudas, *Shape Memory Alloys Modeling and Engineering Applications*, n.d.
- [63] T. Saburi, C.M. Wayman, Crystallographic similarities in shape memory martensites, *Acta Metall.* 27 (1979) 979–995. [https://doi.org/10.1016/0001-6160\(79\)90186-X](https://doi.org/10.1016/0001-6160(79)90186-X).
- [64] M. Brojan, Shape memory alloys in medicine, in: 1995: pp. 26–31.
- [65] L.C. Brinson, One-dimensional constitutive behavior of shape memory alloys: Thermomechanical derivation with non-constant material functions and redefined martensite internal variable, *J. Intell. Mater. Syst. Struct.* 4 (1993) 229–242. <https://doi.org/10.1177/1045389X9300400213>.
- [66] P. Popov, D.C. Lagoudas, A 3-D constitutive model for shape memory alloys incorporating pseudoelasticity and detwinning of self-accommodated martensite, *Int. J. Plast.* 23 (2007) 1679–1720. <https://doi.org/10.1016/j.ijplas.2007.03.011>.
- [67] X. Gao, R. Qiao, L.C. Brinson, Phase diagram kinetics for shape memory alloys: A robust finite element implementation, *Smart Mater. Struct.* 16 (2007) 2102–2115. <https://doi.org/10.1088/0964-1726/16/6/013>.
- [68] M.A. Qidwai, D.C. Lagoudas, On thermomechanics and transformation surfaces of polycrystalline NiTi shape memory alloy material, 2000. [https://doi.org/10.1016/S0749-6419\(00\)00012-7](https://doi.org/10.1016/S0749-6419(00)00012-7).
- [69] P. Shayanfard, M. Kadkhodaei, S. Safaee, Proposition of R-phase transformation strip in the phase diagram of Ni-Ti shape memory alloy using electromechanical experiments, *J. Intell. Mater. Syst. Struct.* 28 (2017). <https://doi.org/10.1177/1045389X17698587>.
- [70] P. Sedlák, M. Frost, B. Benešová, T. Ben Zineb, P. Šittner, Thermomechanical model for NiTi-based shape memory alloys including R-phase and material anisotropy under multi-axial loadings, *Int. J. Plast.* 39 (2012) 132–151. <https://doi.org/10.1016/j.ijplas.2012.06.008>.
- [71] P. Lukáš, P. Šittner, D. Lugovoy, D. Neov, M. Ceretti, In situ neutron diffraction studies of the R-phase transformation in the NiTi shape memory alloy, *Appl. Phys. A Mater. Sci. Process.* 74 (2002) 1121–1123. <https://doi.org/10.1007/s003390101201>.
- [72] F.G.R. Fowkes, D. Rudan, I. Rudan, V. Abovans, J.O. Denenberg, M.M. Mcdermott, P.E. Norman, U.K.A. Sampson, L.J. Williams, G.A. Mensah, M.H. Criqui, Comparison of global estimates of prevalence and risk factors for peripheral artery disease in 2000 and 2010 : a systematic review and analysis, *Lancet.* 382 (2013) 1329–1340. [https://doi.org/10.1016/S0140-6736\(13\)61249-0](https://doi.org/10.1016/S0140-6736(13)61249-0).
- [73] L. Roger, A.S. Go, D.M. Lloyd-jones, R.J. Adams, J.D. Berry, T.M. Brown, M.R. Carnethon, S. Dai, G. De Simone, E.S. Ford, C.S. Fox, H.J. Fullerton, C. Gillespie, K.J. Greenlund, S.M. Hailpern, J.A. Heit, P.M. Ho, V.J. Howard, B.M. Kissela, S.J. Kittner, D.T. Lackland, J.H. Lichtman, L.D. Lisabeth, D.M. Makuc, G.M. Marcus, A. Marelli, D.B. Matchar, M.M. Mcdermott, J.B. Meigs, C.S. Moy, D. Mozaffarian, M.E. Mussolino, G. Nichol, N.P. Paynter, W.D. Rosamond, P.D. Sorlie, R.S. Stafford, T.N. Turan, M.B. Turner, N.D. Wong, J. Wylie-rosett, A. Heart, Heart Disease and Stroke Statistics — 2011 Update A Report From the American Heart Association, (2011) 18–209. <https://doi.org/10.1161/CIR.0b013e3182009701>.
- [74] S. Tyagi, S. Singh, S. Mukhopadhyay, U.A. Kaul, Self- and balloon-expandable stent implantation for severe native coarctation of aorta in adults, *Am. Heart J.* 146 (2003) 920–928. [https://doi.org/10.1016/S0002-8703\(03\)00434-4](https://doi.org/10.1016/S0002-8703(03)00434-4).
- [75] M.D. Martin Schillinger, M.D., Schila Sabeti, M.D., Christian Loewe, M.D., Petra Dick, M.D., Jasmin Amighi, M.D. Wolfgang Mlekusch, M.D., Oliver Schlager, M.D., Manfred Cejna, M.D., Johannes Lammer, M.D., and Erich Minar, Balloon Angioplasty versus Implantation of Nitinol Stents in the Superficial Femoral Artery, *N. Engl. J. Med.* (2015) 687–696. <https://doi.org/10.1056/NEJMoal505949>.

- [76] K. Dai, X. Wu, X. Zu, An investigation of the selective stress-shielding effect of shape-memory sawtooth-arm embracing fixator, *Mater. Sci. Forum.* 394–395 (2002) 17–24. <https://doi.org/10.4028/www.scientific.net/msf.394-395.17>.
- [77] <https://novastep.life/product/nitinol-compression-clips/>, (n.d.).
- [78] Application of Shape Memory Alloys in Seismic Isolation : A Review, 47 (2014) 153–171.
- [79] S. Materials, An overview of vibration and seismic applications of NiTi shape memory alloy, (2002).
- [80] H. Ma, C. Cho, Feasibility study on a superelastic SMA damper with re-centring capability, *Mater. Sci. Eng. A.* 473 (2008) 290–296. <https://doi.org/10.1016/j.msea.2007.04.073>.
- [81] J.C. Su, X.W. Liu, B.Q. Yu, Z.D. Li, M. Li, C.C. Zhang, Shape memory Ni-Ti alloy swan-like bone connector for treatment of humeral shaft nonunion, *Int. Orthop.* 34 (2010) 369–375. <https://doi.org/10.1007/s00264-009-0726-0>.
- [82] C. Song, T.G. Frank, P.A. Campbell, A. Cuschieri, Thermal modelling of shape-memory alloy fixator for minimal-access surgery, *Mater. Sci. Forum.* 394–395 (2002) 53–56. <https://doi.org/10.4028/www.scientific.net/msf.394-395.53>.
- [83] M.M. Kheirikhah, S. Rabiee, M.E. Edalat, A review of shape memory alloy actuators in robotics, in: *Rob. 2010 Robot Soccer World Cup XIV. Rob. 2010. Lect. Notes Comput. Sci.*, Springer, Berlin, Heidelberg, 2010: pp. 206–217. https://doi.org/10.1007/978-3-642-20217-9_18.
- [84] O.K. Rediniotis, D.C. Lagoudas, L.N. Wilson, Development of a Shape Memory Alloy actuated biomimetic hydrofoil, 38th Aersp. Sci. Meet. Exhib. (2000). <https://doi.org/10.2514/6.2000-522>.
- [85] W. Coral, C. Rossi, J. Colorado, D. Lemus, A. Barrientos, SMA-Based Muscle-Like Actuation in Biologically Inspired Robots: A State of the Art Review, *Smart Actuation Sens. Syst. - Recent Adv. Futur. Challenges.* (2012). <https://doi.org/10.5772/50209>.
- [86] A.L. Browne, P.W. Alexander, N. Mankame, P. Usoro, L. Nancy, J. Aase, P. Sarosi, A.C. Keefe, G.P. Mcknight, C. Churchill, J. Shaw, J. Brown, A. Arbor, SMA HEAT ENGINES: ADVANCING FROM A SCIENTIFIC CURIOSITY TO A PRACTICAL REALITY, in: *SMART Mater. Struct. NDT Aersp. Conf.*, 2011. Over 60%25 of energy that is generated is lost as waste heat with close to 90%25 of this waste heat %5Cnbeing classified as low grade being at temperatures less than 200°C.
- [87] E.H. Schiller, Heat Engine Driven by Shape Memory Alloys : Prototyping and Design, 2002.
- [88] D. Avirovik, R.A. Kishore, D. Vuckovic, S. Priya, Miniature Shape Memory Alloy Heat Engine for Powering Wireless Sensor Nodes, *Energy Harvest. Syst.* 1 (2014) 13–18. <https://doi.org/10.1515/ehs-2013-0003>.
- [89] S. Degeratu, L. Alboteanu, S. Rizescu, D. Coman, N.G. Bizdoaca, C. Caramida, Active solar panel tracking system actuated by shape memory alloy springs, 2014 Int. Conf. Appl. Theor. Electr. ICATE 2014 - Proc. (2014). <https://doi.org/10.1109/ICATE.2014.6972678>.
- [90] N.J. Ganesh, S. Maniprakash, L. Chandrasekaran, S.M. Srinivasan, A.R. Srinivasa, Design and development of a sun tracking mechanism using the direct SMA actuation, *J. Mech. Des. Trans. ASME.* 133 (2011). <https://doi.org/10.1115/1.4004380>.
- [91] M. Follador, M. Cianchetti, A. Arienti, C. Laschi, A general method for the design and fabrication of shape memory alloy active spring actuators, *Smart Mater. Struct.* 21 (2012). <https://doi.org/10.1088/0964-1726/21/11/115029>.
- [92] W. Huang, Shape memory alloys and their application to actuators for deployable structures, *Engineering.* (1998) 192. <http://www.ntu.edu.sg/home/mwmhuang/cambridge/Phd2side.pdf>.
- [93] H. Meier, L. Oelschlaeger, Numerical thermomechanical modelling of shape memory alloy wires, *Mater. Sci. Eng. A.* 378 (2004) 484–489. <https://doi.org/10.1016/j.msea.2003.09.113>.
- [94] W. Huang, On the selection of shape memory alloys for actuators, *Mater. Des.* 23 (2002) 11–19. [https://doi.org/10.1016/S0261-3069\(01\)00039-5](https://doi.org/10.1016/S0261-3069(01)00039-5).
- [95] R. Featherstone, Y.H. Teh, Improving the speed of shape memory alloy actuators by faster electrical heating, *Springer Tracts Adv. Robot.* 21 (2006) 67–76. https://doi.org/10.1007/11552246_7.
- [96] S. Hirose, K. Ikuta, Y. Umetani, Development of shape-memory alloy actuators. Performance assessment and introduction of a new composing approach, *Adv. Robot.* 3 (1989) 3–16. <https://doi.org/10.1163/156855389X00145>.
- [97] J. Mohd Jani, M. Leary, A. Subic, M.A. Gibson, A review of shape memory alloy research, applications and opportunities, *Mater. Des.* 56 (2014) 1078–1113. <https://doi.org/10.1016/j.matdes.2013.11.084>.
- [98] C.N. Saikrishna, K. V Ramaiah, D. Paul, S.K. Bhaumik, Acta Materialia Enhancement in fatigue life of NiTi shape memory alloy thermal actuator wire, 102 (2016). <https://doi.org/10.1016/j.actamat.2015.09.034>.
- [99] P. Shayanfard, M. Kadkhodaei, Numerical and Experimental Investigation on Electro-Thermo-Mechanical Behavior of NiTi Shape Memory Alloy Wires, *Iran. J. Sci. Technol. Trans. Mech. Eng.* 8 (2018). <https://doi.org/10.1007/s40997-018-0183-8>.
- [100] M. Elahinia, Shape Memory Alloy Actuators Design , Fabrication , and, 2016.
- [101] D. Stoeckel, Shape memory actuators for Automotive applications, *Mater. Des.* 11 (1990) 21–28. [https://doi.org/10.1016/0261-3069\(91\)90088-L](https://doi.org/10.1016/0261-3069(91)90088-L).
- [102] S.C.N. Bhaumik S.K., Ramaiah K.V., Nickel–Titanium Shape Memory Alloy Wires for Thermal Actuators, in: Vinoy K., Ananthasuresh G., Pratap R., Krupanidhi S, *Micro Smart Devices Syst.*, Springer Tracts in Mechanical Engineering. Springer, New Delhi, 2014.
- [103] J. Van Humbeeck, Non-medical applications of shape memory alloys, *Mater. Sci. Eng. A.* 273–275 (1999) 134–

- [104] G. Eggeler, E. Hornbogen, A. Yawny, A. Heckmann, M. Wagner, Structural and functional fatigue of NiTi shape memory alloys, *Mater. Sci. Eng. A*. 378 (2004) 24–33. <https://doi.org/10.1016/j.msea.2003.10.327>.
- [105] T. Hashimoto, H. Tobushi, T. Nakahara, Y. Shimeno, Low-cycle fatigue of TiNi shape memory alloy and formulation of fatigue life, *Nihon Kikai Gakkai Ronbunshu, A Hen/Transactions Japan Soc. Mech. Eng. Part A*. 64 (1998) 2548–2554. <https://doi.org/10.1299/kikaia.64.2548>.
- [106] T.A. Sawaguchi, G. Kausträter, A. Yawny, M. Wagner, G. Eggeler, Crack initiation and propagation in 50.9 at. pct Ni-Ti pseudoelastic shape-memory wires in bending-rotation fatigue, *Metall. Mater. Trans. A*. (2003). <https://doi.org/10.1007/s11661-003-0186-x>.
- [107] M. Wagner, T. Sawaguchi, G. Kausträter, D. Höffken, G. Eggeler, Structural fatigue of pseudoelastic NiTi shape memory wires, *Mater. Sci. Eng. A*. 378 (2004) 105–109. <https://doi.org/10.1016/j.msea.2003.11.058>.
- [108] R. Matsui, H. Tobushi, Y. Furuichi, H. Horikawa, Tensile deformation and rotating-bending fatigue properties of a highelastic thin wire, a superelastic thin wire, and a superelastic thin tube of NiTi alloys, *J. Eng. Mater. Technol. Trans. ASME*. 126 (2004) 384–391. <https://doi.org/10.1115/1.1789952>.
- [109] A.M. Figueiredo, P. Modenesi, V. Buono, Low-cycle fatigue life of superelastic NiTi wires, *Int. J. Fatigue*. 31 (2009) 751–758. <https://doi.org/10.1016/j.ijfatigue.2008.03.014>.
- [110] M. Kollerov, E. Lukina, D. Gusev, P. Mason, P. Wagstaff, Impact of material structure on the fatigue behaviour of NiTi leading to a modified Coffin–Manson equation, *Mater. Sci. Eng. A*. 585 (2013) 356–362. <https://doi.org/10.1016/j.msea.2013.07.072>.
- [111] R. Rudolf, J. Ferčec, V. Lazić, V. Veselinović, S. Tomić, Characterisation of NiTi orthodontic archwires characteristic functional properties BT - CMBEBIH 2017, in: A. Badnjevic (Ed.), Springer Singapore, Singapore, 2017: pp. 323–332.
- [112] T. Duerig, A. Pelton, D. Sto, An overview of nitinol medical applications, *Mater. Sci. Eng. A*. 275 (1999) 149–160. [https://doi.org/10.1016/S0921-5093\(99\)00294-4](https://doi.org/10.1016/S0921-5093(99)00294-4).
- [113] W. Predki, M. Klönne, A. Knopik, Cyclic torsional loading of pseudoelastic NiTi shape memory alloys: Damping and fatigue failure, *Mater. Sci. Eng. A*. 417 (2006) 182–189. <https://doi.org/10.1016/j.msea.2005.10.037>.
- [114] C. Dunand-Châtelle, Z. Moumni, Experimental analysis of the fatigue of shape memory alloys through power-law statistics, *Int. J. Fatigue*. 36 (2012) 163–170. <https://doi.org/10.1016/j.ijfatigue.2011.07.014>.
- [115] Z. Moumni, A. Van Herpen, P. Riberty, Fatigue analysis of shape memory alloys: Energy approach, *Smart Mater. Struct.* 14 (2005). <https://doi.org/10.1088/0964-1726/14/5/017>.
- [116] C. Maletta, E. Sgambitterra, F. Furgiuele, R.C. and A. Tuissi, Fatigue of pseudoelastic NiTi within the stress-induced transformation regime : a modified Coffin – Manson approach, (2012). <https://doi.org/10.1088/0964-1726/21/11/112001>.
- [117] C. Maletta, L. Bruno, P. Corigliano, V. Crupi, E. Guglielmino, Crack-tip thermal and mechanical hysteresis in shape memory alloys under fatigue loading, *Mater. Sci. Eng. A*. (2014). <https://doi.org/10.1016/j.msea.2014.08.007>.
- [118] O. Tyc, J. Pilch, P. Sittner, Fatigue of superelastic NiTi wires with different plateau strain, *Procedia Struct. Integr.* 2 (2016) 1489–1496. <https://doi.org/10.1016/j.prostr.2016.06.189>.
- [119] M. Rahim, J. Frenzel, M. Frotscher, J. Pftzing-Micklich, R. Steegmüller, M. Wohlschlägel, H. Mughrabi, G. Eggeler, Impurity levels and fatigue lives of pseudoelastic NiTi shape memory alloys, *Acta Mater.* 61 (2013) 3667–3686. <https://doi.org/10.1016/j.actamat.2013.02.054>.
- [120] A.R. Pelton, J. DiCello, S. Miyazaki, Optimisation of processing and properties of medical grade Nitinol wire, *Minim. Invasive Ther. Allied Technol.* 9 (2000) 107–118. <https://doi.org/10.3109/13645700009063057>.
- [121] J.E. Schaffer, D.L. Plumley, Fatigue performance of nitinol round wire with varying cold work reductions, *J. Mater. Eng. Perform.* 18 (2009) 563–568. <https://doi.org/10.1007/s11665-009-9363-4>.
- [122] J.E. Schaffer, Structure-Property Relationships in Conventional and Nanocrystalline NiTi Intermetallic Alloy Wire, 18 (2009) 582–587. <https://doi.org/10.1007/s11665-009-9369-y>.
- [123] A.R. Pelton, V. Schroeder, M.R. Mitchell, X.Y. Gong, M. Barney, S.W. Robertson, Fatigue and durability of Nitinol stents, *J. Mech. Behav. Biomed. Mater.* 1 (2008) 153–164. <https://doi.org/10.1016/j.jmbbm.2007.08.001>.
- [124] N.B. Morgan, J. Painter, A. Moffat, Mean strain effects and microstructural observations during in vitro fatigue testing of NiTi, *SMST-2003. Proc.* 79 (2004) 303–310. <https://doi.org/10.1111/j.2044-8295.1988.tb02271.x>.
- [125] M.J. Mahtabi, N. Shamsaei, B. Rutherford, Mean strain effects on the fatigue behavior of superelastic Nitinol alloys : An experimental investigation, *Procedia Eng.* 133 (2015) 646–654. <https://doi.org/10.1016/j.proeng.2015.12.645>.
- [126] L.Y. Miyazaki S, Mizukoshi K, Ueki T, Sakuma T, Fatigue-life-of-Ti-50-at-Ni-and-Ti-40Ni-10Cu-at-shape-memory-alloy-wires, *Materials-Science-and-Engineering. A273-275* (1999) 658–663.
- [127] A.R. Pelton, J. Fino-Decker, L. Vien, C. Bonsignore, P. Saffari, M. Launey, M.R. Mitchell, Rotary-bending fatigue characteristics of medical-grade Nitinol wire, *J. Mech. Behav. Biomed. Mater.* 27 (2013) 19–32. <https://doi.org/10.1016/j.jmbbm.2013.06.003>.
- [128] D. Song, G. Kang, Q. Kan, C. Yu, C. Zhang, Experimental observations on uniaxial whole-life transformation ratchetting and low-cycle stress fatigue of super-elastic NiTi shape memory alloy micro-tubes, *Smart Mater. Struct.* 24 (2015). <https://doi.org/10.1088/0964-1726/24/7/075004>.
- [129] D. Song, G. Kang, Q. Kan, C. Yu, C. Zhang, Non-proportional multiaxial whole-life transformation ratchetting

- and fatigue failure of super-elastic NiTi shape memory alloy micro-tubes, *Int. J. Fatigue*. 80 (2015) 372–380. <https://doi.org/10.1016/j.ijfatigue.2015.06.028>.
- [130] D. Song, G. Kang, Q. Kan, C. Yu, C. Zhang, Non-proportional multiaxial transformation ratchetting of super-elastic NiTi shape memory alloy: Experimental observations, *Mech. Mater.* 70 (2014) 94–105. <https://doi.org/10.1016/j.mechmat.2013.12.003>.
- [131] X.M. Wang, Y.F. Wang, Z.Z. Lu, C.H. Deng, Z.F. Yue, An experimental study of the superelastic behavior in NiTi shape memory alloys under biaxial proportional and non-proportional cyclic loadings, *Mech. Mater.* 42 (2010) 365–373. <https://doi.org/10.1016/j.mechmat.2009.11.010>.
- [132] L. Heller, P. Šittner, P. Sedlák, H. Seiner, O. Tyc, L. Kadeřávek, P. Sedmák, M. Vronka, Beyond the strain recoverability of martensitic transformation in NiTi, *Int. J. Plast.* 116 (2019) 232–264. <https://doi.org/10.1016/j.ijplas.2019.01.007>.
- [133] P. Sedmak, P. Sittner, J. Pilch, C. Curfs, Instability of cyclic superelastic deformation of NiTi investigated by synchrotron X-ray diffraction, *Acta Mater.* 94 (2015) 257–270. <https://doi.org/10.1016/j.actamat.2015.04.039>.
- [134] S. Miyazaki, T. Imai, Y. Igo, K. Otsuka, Effect of cyclic deformation on the pseudoelasticity characteristics of Ti-Ni alloys, *Metall. Trans. A*. 17 (1986) 115–120. <https://doi.org/10.1007/BF02644447>.
- [135] N. Nayan, D. Roy, V. Buravalla, U. Ramamurty, Unnotched fatigue behavior of an austenitic Ni – Ti shape memory alloy, 497 (2008) 333–340. <https://doi.org/10.1016/j.msea.2008.07.025>.
- [136] N.S.E.P.M.B.A. Eberhardt, Constitutive equations for polycrystalline thermoelastic shape memory alloys. Part I. Intragranular interactions and behavior of the grain, *Mater. Des.* 102 (2016) 213–224.
- [137] P.Ā. Thamburaja, Constitutive equations for martensitic reorientation and detwinning in shape-memory alloys, 53 (2005) 825–856. <https://doi.org/10.1016/j.jmps.2004.11.004>.
- [138] M. Frotscher, S. Wu, T. Simon, C. Somsen, A. Dlouhy, G. Eggeler, Elementary deformation and damage mechanisms during fatigue of pseudoelastic NiTi microstents, *Adv. Eng. Mater.* (2011). <https://doi.org/10.1002/adem.201180001>.
- [139] S. Mao, X. Han, M.H. Wu, Z. Zhang, F. Hao, D. Liu, Y. Zhang, B. Hou, Effect of cyclic loading on apparent young's modulus and critical stress in nano-subgrained superelastic NiTi shape memory alloys, *Mater. Trans.* 47 (2006) 735–741. <https://doi.org/10.2320/matertrans.47.735>.
- [140] C. Maletta, E. Sgambitterra, F. Furgiuele, R. Casati, A. Tuissi, Fatigue properties of a pseudoelastic NiTi alloy: Strain ratcheting and hysteresis under cyclic tensile loading, *Int. J. Fatigue*. 66 (2014) 78–85. <https://doi.org/10.1016/j.ijfatigue.2014.03.011>.
- [141] S. Nemat-Nasser, W.G. Guo, Superelastic and cyclic response of NiTi SMA at various strain rates and temperatures, *Mech. Mater.* 38 (2006) 463–474. <https://doi.org/10.1016/j.mechmat.2005.07.004>.
- [142] K.C. Atili, B.E. Franco, I. Karaman, D. Gaydos, R.D. Noebe, Influence of crystallographic compatibility on residual strain of TiNi based shape memory alloys during thermo-mechanical cycling, *Mater. Sci. Eng. A*. 574 (2013) 9–16. <https://doi.org/10.1016/j.msea.2013.02.035>.
- [143] D.M. Norfleet, P.M. Sarosi, S. Manchiraju, M.F.X. Wagner, M.D. Uchic, P.M. Anderson, M.J. Mills, Transformation-induced plasticity during pseudoelastic deformation in Ni-Ti microcrystals, *Acta Mater.* 57 (2009) 3549–3561. <https://doi.org/10.1016/j.actamat.2009.04.009>.
- [144] X.M. Wang, Q.T. Zhou, H. Liu, C.H. Deng, Z.F. Yue, Experimental study of the biaxial cyclic behavior of thin-wall tubes of NiTi shape memory alloys, *Metall. Mater. Trans. A Phys. Metall. Mater. Sci.* 43 (2012) 4123–4128. <https://doi.org/10.1007/s11661-012-1225-2>.
- [145] G. Kang, Q. Kan, C. Yu, D. Song, Y. Liu, Whole-life transformation ratchetting and fatigue of super-elastic NiTi Alloy under uniaxial stress-controlled cyclic loading, *Mater. Sci. Eng. A*. 535 (2012) 228–234. <https://doi.org/10.1016/j.msea.2011.12.071>.
- [146] D.C. Lagoudas, D.A. Miller, L. Rong, P.K. Kumar, Thermomechanical fatigue of shape memory alloys, *Smart Mater. Struct.* 18 (2009). <https://doi.org/10.1088/0964-1726/18/8/085021>.
- [147] S. Padula, S. Qiu, D. Gaydos, R. Noebe, G. Bigelow, A. Garg, R. Vaidyanathan, Effect of upper-cycle temperature on the load-biased, strain-temperature response of NiTi, *Metall. Mater. Trans. A Phys. Metall. Mater. Sci.* 43 (2012) 4610–4621. <https://doi.org/10.1007/s11661-012-1267-5>.
- [148] E.Y. Panchenko, Y.I. Chumlyakov, I. V. Kireeva, A. V. Ovsyannikov, H. Sehitoglu, I. Karaman, Y.H.J. Maier, Effect of disperse Ti₃N₄ particles on the martensitic transformations in titanium nickelide single crystals, *Phys. Met. Metallogr.* 106 (2008) 577–589. <https://doi.org/10.1134/S0031918X08120065>.
- [149] J. Khalil-Allafi, A. Dlouhy, G. Eggeler, Ni₄Ti₃-precipitation during aging of NiTi shape memory alloys and its influence on martensitic phase transformations, *Acta Mater.* 50 (2002) 4255–4274. [https://doi.org/10.1016/S1359-6454\(02\)00257-4](https://doi.org/10.1016/S1359-6454(02)00257-4).
- [150] K. Gall, H. Sehitoglu, Y.I. Chumlyakov, Y.L. Zuev, I. Karaman, The role of coherent precipitates in martensitic transformations in single crystal and polycrystalline Ti-50.8at%Ni, *Scr. Mater.* 39 (1998) 699–705. [https://doi.org/10.1016/S1359-6462\(98\)00236-X](https://doi.org/10.1016/S1359-6462(98)00236-X).
- [151] J.I. Kim, S. Miyazaki, Effect of nano-scaled precipitates on shape memory behavior of Ti-50.9at.%Ni alloy, *Acta Mater.* 53 (2005) 4545–4554. <https://doi.org/10.1016/j.actamat.2005.06.009>.
- [152] K. Gall, H. Sehitoglu, R. Anderson, I. Karaman, Y.I. Chumlyakov, I. V. Kireeva, On the mechanical behavior of single crystal NiTi shape memory alloys and related polycrystalline phenomenon, *Mater. Sci. Eng. A*. 317 (2001) 85–92. [https://doi.org/10.1016/S0921-5093\(01\)01183-2](https://doi.org/10.1016/S0921-5093(01)01183-2).
- [153] M. Nishida, C.M. Wayman, T. Honma, Precipitation processes in near-equiatomic TiNi shape memory alloys,

- Metall. Trans. A. 17 (1986) 1505–1515. <https://doi.org/10.1007/BF02650086>.
- [154] H. Sehitoglu, J. Jun, X. Zhang, I. Karaman, Y. Chumlyakov, H.J. Maier, K. Gall, Shape memory and pseudoelastic behavior of 51.5%Ni-Ti single crystals in solutionized and overaged state, *Acta Mater.* 49 (2001) 3609–3620. [https://doi.org/10.1016/S1359-6454\(01\)00216-6](https://doi.org/10.1016/S1359-6454(01)00216-6).
- [155] A. Evirgen, I. Karaman, J. Pons, R. Santamarta, R.D. Noebe, Role of nano-precipitation on the microstructure and shape memory characteristics of a new Ni_{50.3}Ti_{34.7}Zr₁₅ shape memory alloy, *Mater. Sci. Eng. A.* 655 (2016) 193–203. <https://doi.org/10.1016/j.msea.2015.12.076>.
- [156] A. EVIRGEN, MICROSTRUCTURAL CHARACTERIZATION AND SHAPE MEMORY RESPONSE OF Ni-RICH NiTiHf AND NiTiZr HIGH TEMPERATURE SHAPE MEMORY ALLOYS, Texas A&M University, 2014.
- [157] K. Otsuka, X. Ren, Recent developments in the research of shape memory alloys, *Intermetallics.* 7 (1999) 511–528. [https://doi.org/10.1016/S0966-9795\(98\)00070-3](https://doi.org/10.1016/S0966-9795(98)00070-3).
- [158] D.R. Coughlin, P.J. Phillips, G.S. Bigelow, A. Garg, R.D. Noebe, M.J. Mills, Characterization of the microstructure and mechanical properties of a 50.3Ni-29.7Ti-20Hf shape memory alloy, *Scr. Mater.* 67 (2012) 112–115. <https://doi.org/10.1016/j.scriptamat.2012.03.036>.
- [159] H.E. Karaca, E. Acar, G.S. Ded, B. Basaran, H. Tobe, R.D. Noebe, G. Bigelow, Y.I. Chumlyakov, Shape memory behavior of high strength NiTiHfPd polycrystalline alloys, *Acta Mater.* 61 (2013) 5036–5049. <https://doi.org/10.1016/j.actamat.2013.04.039>.
- [160] G. Kang, Q. Kan, L. Qian, Y. Liu, Ratchetting deformation of super-elastic and shape-memory NiTi alloys, *Mech. Mater.* 41 (2009) 139–153. <https://doi.org/10.1016/j.mechmat.2008.09.001>.
- [161] C. Yu, G. Kang, Q. Kan, Crystal plasticity based constitutive model of NiTi shape memory alloy considering different mechanisms of inelastic deformation, *Int. J. Plast.* 54 (2014) 132–162. <https://doi.org/10.1016/j.ijplas.2013.08.012>.
- [162] Y. Liu, Z. Xie, Detwinning in shape memory alloy, 2007. [http://www3.ntu.edu.sg/home/mliuy/Newfiles/articles/Book Chapter - Detwinning in Shape Memory Alloy.pdf](http://www3.ntu.edu.sg/home/mliuy/Newfiles/articles/Book%20Chapter%20-%20Detwinning%20in%20Shape%20Memory%20Alloy.pdf).
- [163] S. Miyazaki, K. Otsuka, Y. Suzuki, TRANSFORMATION PSEUDOELASTICITY AND DEFORMATION BEHAVIOR IN A Ti-50.6at%Ni ALLOY, *Scr. Metall.* 15 (1981) 287–292.
- [164] J.S. Olsen, Z.L. Zhang, J.K. Hals, H. Lu, Effect of notches on the behavior of superelastic round-bar NiTi-specimens, *Smart Mater. Struct.* 21 (2012). <https://doi.org/10.1088/0964-1726/21/3/039501>.
- [165] X. Wang, B. Xu, Z. Yue, X. Tong, Fracture behavior of the compact tension specimens in NiTi shape memory alloys, *Mater. Sci. Eng. A.* (2008). <https://doi.org/10.1016/j.msea.2007.07.056>.
- [166] Y. Lu, L. Qiao, W. Chu, In-situ study of martensitic transformation and nucleation, propagation of crack in CuNiAl shape memory alloy, *Sci. China, Ser. A Math. Physics, Astron.* 44 (2001) 932–939. <https://doi.org/10.1007/BF02880143>.
- [167] G.M. Vasko, P.H. Leo, T.W. Shield, Prediction and observation of crack tip microstructure in shape memory CuAlNi single crystals, *J. Mech. Phys. Solids.* 50 (2002) 1843–1867. www.elsevier.com/locate/jmps.
- [168] G.M. Loughran, T.W. Shield, P.H. Leo, Fracture of shape memory CuAlNi single crystals, *Int. J. Solids Struct.* (2003). [https://doi.org/10.1016/S0020-7683\(02\)00550-4](https://doi.org/10.1016/S0020-7683(02)00550-4).
- [169] S.W. Robertson, A. Mehta, A.R. Pelton, R.O. Ritchie, Evolution of crack-tip transformation zones in superelastic Nitinol subjected to in situ fatigue: A fracture mechanics and synchrotron X-ray microdiffraction analysis, *Acta Mater.* (2007). <https://doi.org/10.1016/j.actamat.2007.07.028>.
- [170] S. Gollerthan, M.L. Young, A. Baruj, J. Frenzel, W.W. Schmahl, G. Eggeler, Fracture mechanics and microstructure in NiTi shape memory alloys, *Acta Mater.* 57 (2009) 1015–1025. <https://doi.org/10.1016/j.actamat.2008.10.055>.
- [171] M.R. Daymond, M.L. Young, J.D. Almer, D.C. Dunand, Strain and texture evolution during mechanical loading of a crack tip in martensitic shape-memory NiTi, *Acta Mater.* (2007). <https://doi.org/10.1016/j.actamat.2007.03.013>.
- [172] M.L. Young, S. Gollerthan, A. Baruj, J. Frenzel, W.W. Schmahl, G. Eggeler, Strain mapping of crack extension in pseudoelastic NiTi shape memory alloys during static loading, *Acta Mater.* 61 (2013) 5800–5806. <https://doi.org/10.1016/j.actamat.2013.06.024>.
- [173] V. Tallebot, C. Lexcellent, P. Malécot, R. Laydi, Analysis of the phase transformation near the crack tip in Shape Memory Alloys, ESOMAT 2009 - 8th Eur. Symp. Martensitic Transform. 06034 (2009). <https://doi.org/10.1051/esomat/200906034>.
- [174] S. Gollerthan, M.L. Young, K. Neuking, U. Ramamurty, G. Eggeler, Direct physical evidence for the back-transformation of stress-induced martensite in the vicinity of cracks in pseudoelastic NiTi shape memory alloys, *Acta Mater.* (2009). <https://doi.org/10.1016/j.actamat.2009.08.015>.
- [175] E. Sgambitterra, C. Maletta, F. Furgiuele, Temperature dependent local phase transformation in shape memory alloys by nanoindentation, *Scr. Mater.* (2015). <https://doi.org/10.1016/j.scriptamat.2015.01.020>.
- [176] S. Daly, A. Miller, G. Ravichandran, K. Bhattacharya, An experimental investigation of crack initiation in thin sheets of nitinol, *Acta Mater.* (2007). <https://doi.org/10.1016/j.actamat.2007.07.038>.
- [177] E. Sgambitterra, S. Lesci, C. Maletta, Effects of Higher Order Terms in Fracture Mechanics of Shape Memory Alloys Bydigital Image Correlation, in: *Procedia Eng.*, 2015. <https://doi.org/10.1016/j.proeng.2015.06.263>.
- [178] Y. Freed, L. Banks-Sills, Crack growth resistance of shape memory alloys by means of a cohesive zone model, *J. Mech. Phys. Solids.* (2007). <https://doi.org/10.1016/j.jmps.2007.03.002>.

- [179] X.M. Wang, Y.F. Wang, A. Baruj, G. Eggeler, Z.F. Yue, On the formation of martensite in front of cracks in pseudoelastic shape memory alloys, *Mater. Sci. Eng. A.* (2005). <https://doi.org/10.1016/j.msea.2004.11.029>.
- [180] N. Shafaghi, B. Haghgouyan, C.C. Can Aydiner, G. Anlas, Experimental and Computational Evaluation of Crack-tip Displacement Field and Transformation Zone in NiTi, *Mater. Today Proc.* 2 (2015) S763–S766. <https://doi.org/10.1016/j.matpr.2015.07.394>.
- [181] T. Baxevanis, A.F. Parrinello, D.C. Lagoudas, 32 On the fracture toughness enhancement due to stress-induced phase transformation in shape memory alloys, *Int. J. Plast.* 50 (2013) 158–169. <https://doi.org/10.1016/j.ijplas.2013.04.007>.
- [182] S.H. Ardakani, H. Ahmadian, S. Mohammadi, Thermo-mechanically coupled fracture analysis of shape memory alloys using the extended finite element method, *Smart Mater. Struct.* 24 (2015) 45031. <https://doi.org/10.1088/0964-1726/24/4/045031>.
- [183] X.K. Zhu, J.A. Joyce, Review of fracture toughness (G, K, J, CTOD, CTOA) testing and standardization, *Eng. Fract. Mech.* 85 (2012) 1–46. <https://doi.org/10.1016/j.engfracmech.2012.02.001>.
- [184] J. Pokluda, P. Sandera, *Micromechanisms of Fracture and Fatigue: In a Multi-scale Context (Engineering Materials and Processes)*, (n.d.).
- [185] D. Broek, J.R. Rice, *Elementary Engineering Fracture Mechanics*, *J. Appl. Mech.* (1975). <https://doi.org/10.1115/1.3423697>.
- [186] A. A. Griffith, *The Phenomena of Rupture and Flow in Solids* Author (s): A . A . Griffith Source : *Philosophical Transactions of the Royal Society of London . Series A , Containing Papers of a Mathematical or Physical Character , Vol . 221 (1921) , pp . 163-198* Publish, *Philos. Trans. R. Soc. London. Ser. A, Contain. Pap. a Math. or Phys. Character.* 221 (2016) 163–198.
- [187] T. Edition, *FRACTURE*, n.d.
- [188] W.M. Garrison, N.R. Moody, Ductile fracture, *J. Phys. Chem. Solids.* 48 (1987) 1035–1074. [https://doi.org/10.1016/0022-3697\(87\)90118-1](https://doi.org/10.1016/0022-3697(87)90118-1).
- [189] J.R. Rice, A path independent integral and the approximate analysis of strain concentration by notches and cracks, *J. Appl. Mech. Trans. ASME.* 35 (1964) 379–388. <https://doi.org/10.1115/1.3601206>.
- [190] A.A. Wells, Application of fracture mechanics at and beyond general yielding, *Br. Weld. J.* 10 (1963) 563–570. <https://doi.org/10.1002/9780470827826.ch7>.
- [191] T. Baxevanis, D.C. Lagoudas, Fracture mechanics of shape memory alloys: review and perspectives, *Int. J. Fract.* (2015). <https://doi.org/10.1007/s10704-015-9999-z>.
- [192] S.W. Robertson, R.O. Ritchie, In vitro fatigue-crack growth and fracture toughness behavior of thin-walled superelastic Nitinol tube for endovascular stents: A basis for defining the effect of crack-like defects, *Biomaterials.* 28 (2007) 700–709. <https://doi.org/10.1016/j.biomaterials.2006.09.034>.
- [193] T. Baxevanis, D.C. Lagoudas, Fracture mechanics of shape memory alloys: review and perspectives, *Int. J. Fract.* 191 (2015) 191–213. <https://doi.org/10.1007/s10704-015-9999-z>.
- [194] S.W. Robertson, R.O. Ritchie, A Fracture-Mechanics-Based Approach to Fracture Control in Biomedical Devices Manufactured From Superelastic Nitinol Tube, (2007) 26–33. <https://doi.org/10.1002/jbmb>.
- [195] S. Yi, S. Gao, Fracture toughening mechanism of shape memory alloys due to martensite transformation, *Int. J. Solids Struct.* 37 (2000) 5315–5327. [https://doi.org/10.1016/S0020-7683\(99\)00213-9](https://doi.org/10.1016/S0020-7683(99)00213-9).
- [196] T. Leitner, I. Sabirov, R. Phipps, A. Hohenwarter, The effect of severe grain refinement on the damage tolerance of a superelastic NiTi shape memory alloy, *J. Mech. Behav. Biomed. Mater.* 71 (2017) 337–348. <https://doi.org/10.1016/j.jmbbm.2017.03.020>.
- [197] A. Ahadi, Q. Sun, Grain size dependence of fracture toughness and crack-growth resistance of superelastic NiTi, *Scr. Mater.* (2016). <https://doi.org/10.1016/j.scriptamat.2015.10.036>.
- [198] B. Haghgouyan, C. Hayrettin, T. Baxevanis, I. Karaman, D.C. Lagoudas, Fracture toughness of NiTi—Towards establishing standard test methods for phase transforming materials, *Acta Mater.* 162 (2019) 226–238. <https://doi.org/10.1016/j.actamat.2018.09.048>.
- [199] E. Sgambitterra, L. Bruno, C. Maletta, Stress induced martensite at the crack tip in NiTi alloys during fatigue loading, *Frat. Ed Integrita Strutt.* 30 (2014) 167–173. <https://doi.org/10.3221/IGF-ESIS.30.22>.
- [200] R.O. Ritchie, Mechanisms of Fatigue-Crack Propagation in Ductile and Brittle Solids, *Int. J. Fract.* 100 (1999) 55–83. <https://doi.org/10.1023/A:1018655917051>.
- [201] R. Thomson, *Y* , , , , *Y* , , , , 72 (1994) 852–856.
- [202] T. Ungár, J. Frenzel, S. Gollerthan, G. Ribárik, L. Balogh, G. Eggeler, On the competition between the stress-induced formation of martensite and dislocation plasticity during crack propagation in pseudoelastic NiTi shape memory alloys, *J. Mater. Res.* (2017) 1–10. <https://doi.org/10.1557/jmr.2017.267>.
- [203] B. Haghgouyan, N. Shafaghi, C.C. Aydiner, G. Anlas, Experimental and computational investigation of the effect of phase transformation on fracture parameters of an SMA, *Smart Mater. Struct.* 25 (2016) 075010. <https://doi.org/10.1088/0964-1726/25/7/075010>.
- [204] J. Eftis, N. Subramonian, H. Liebowitz, Crack border stress and displacement equations revisited, *Eng. Fract. Mech.* 9 (1977) 189–210. [https://doi.org/10.1016/0013-7944\(77\)90063-7](https://doi.org/10.1016/0013-7944(77)90063-7).
- [205] E. Sgambitterra, S. Lesci, C. Maletta, Effects of Higher Order Terms in Fracture Mechanics of Shape Memory Alloys Bydigital Image Correlation, *Procedia Eng.* 109 (2015) 457–464. <https://doi.org/10.1016/j.proeng.2015.06.263>.
- [206] C. Maletta, F. Furgiuele, Analytical modeling of stress-induced martensitic transformation in the crack tip region

- of nickel-titanium alloys, *Acta Mater.* (2010). <https://doi.org/10.1016/j.actamat.2009.08.060>.
- [207] J. Luo, J. He, X. Wan, T. Dong, Y. Cui, X. Xiong, Fracture properties of polycrystalline NiTi shape memory alloy, *Mater. Sci. Eng. A.* (2016). <https://doi.org/10.1016/j.msea.2015.12.014>.
- [208] C. Maletta, E. Sgambitterra, F. Niccoli, Temperature dependent fracture properties of shape memory alloys: Novel findings and a comprehensive model, *Sci. Rep.* 6 (2016) 1–11. <https://doi.org/10.1038/s41598-016-0024-1>.
- [209] B. Haghgouyan, S. Jape, T. Baxevanis, I. Karaman, D.C. Lagoudas, Stable crack growth in NiTi shape memory alloys: 3D finite element modeling and experimental validation, *Smart Mater. Struct.* 28 (2019). <https://doi.org/10.1088/1361-665X/ab14a9>.
- [210] C. Maletta, E. Sgambitterra, F. Furgiuele, Crack tip stress distribution and stress intensity factor in shape memory alloys, *Fatigue Fract. Eng. Mater. Struct.* 36 (2013) 903–912. <https://doi.org/10.1111/ffe.12055>.
- [211] S. Daly, A. Miller, G. Ravichandran, K. Bhattacharya, An experimental investigation of crack initiation in thin sheets of nitinol, *Acta Mater.* 55 (2007) 6322–6330. <https://doi.org/10.1016/j.actamat.2007.07.038>.
- [212] R.L. Holtz, K. Sadananda, M.A. Imam, Fatigue thresholds of Ni-Ti alloy near the shape memory transition temperature, *Int. J. Fatigue.* 21 (1999) 137–145. www.elsevier.com/locate/ijfatigue.
- [213] T. Baxevanis, C.M. Landis, D.C. Lagoudas, 96 On the Fracture Toughness of Pseudoelastic Shape Memory Alloys, *J. Appl. Mech.* 81 (2013) 041005. <https://doi.org/10.1115/1.4025139>.
- [214] P. Shayanfard, L. Heller, P. Šandera, P. Šittner, Thermomechanically transforming Notched NiTi Thin ribbon : Effect of Martensitic Transformation on Stress Gradients, *Struct. Integr. Procedia.* 23 (2019) 620–625. <https://doi.org/10.1016/j.prostr.2020.01.155>.
- [215] S. Jape, T. Baxevanis, D.C. Lagoudas, Stable Crack Growth During Thermal Actuation of Shape Memory Alloys, *Shape Mem. Superelasticity.* 2 (2016) 104–113. <https://doi.org/10.1007/s40830-015-0046-8>.
- [216] S. Jape, T. Baxevanis, D.C. Lagoudas, On the fracture toughness and stable crack growth in shape memory alloy actuators in the presence of transformation-induced plasticity, *Int. J. Fract.* 209 (2018) 117–130. <https://doi.org/10.1007/s10704-017-0245-8>.
- [217] A.L. McKelvey, R.O. Ritchie, Fatigue-crack growth behavior in the superelastic and shape-memory alloy nitinol, *Metall. Mater. Trans. A Phys. Metall. Mater. Sci.* 32 (2001) 731–743. <https://doi.org/10.1007/s11661-001-1008-7>.
- [218] W.S. Lepage, T.M. Pollock, J.A. Shaw, Grain size effects on NiTi shape memory alloy fatigue crack growth, *J. Mater. Res.* 33 (2018) 91–107. <https://doi.org/10.1557/jmr.2017.395>.
- [219] G.Z. Wang, F.Z. Xuan, S.T. Tu, Z.D. Wang, Effects of triaxial stress on martensite transformation, stress-strain and failure behavior in front of crack tips in shape memory alloy NiTi, *Mater. Sci. Eng. A.* 527 (2010) 1529–1536. <https://doi.org/10.1016/j.msea.2009.10.038>.
- [220] Y. You, Y. Zhang, Z. Moumni, G. Anlas, W. Zhang, Effect of the thermomechanical coupling on fatigue crack propagation in NiTi shape memory alloys, *Mater. Sci. Eng. A.* (2017). <https://doi.org/10.1016/j.msea.2016.12.126>.
- [221] L. Zheng, Y. He, Z. Moumni, Investigation on fatigue behaviors of NiTi polycrystalline strips under stress-controlled tension via in-situ macro-band observation, *Int. J. Plast.* 90 (2017) 116–145. <https://doi.org/10.1016/j.ijplas.2016.12.008>.
- [222] C. Maletta, M.L. Young, Stress-induced martensite in front of crack tips in niti shape memory alloys: Modeling versus experiments, *J. Mater. Eng. Perform.* 20 (2011) 597–604. <https://doi.org/10.1007/s11665-011-9852-0>.
- [223] C. Maletta, F. Furgiuele, Analytical modeling of stress-induced martensitic transformation in the crack tip region of nickel-titanium alloys, *Acta Mater.* 58 (2010) 92–101. <https://doi.org/10.1016/j.actamat.2009.08.060>.
- [224] C. Maletta, F. Furgiuele, Fracture control parameters for NiTi based shape memory alloys, *Int. J. Solids Struct.* 48 (2011) 1658–1664. <https://doi.org/10.1016/j.ijsolstr.2011.02.014>.
- [225] C. Morin, Z. Moumni, W. Zaki, Thermomechanical coupling in shape memory alloys under cyclic loadings: Experimental analysis and constitutive modeling, *Int. J. Plast.* 27 (2011) 1959–1980. <https://doi.org/10.1016/j.ijplas.2011.05.005>.
- [226] H. Yin, Y. He, Q. Sun, Journal of the Mechanics and Physics of Solids Effect of deformation frequency on temperature and stress oscillations in cyclic phase transition of NiTi shape memory alloy, *J. Mech. Phys. Solids.* 67 (2014) 100–128. <https://doi.org/10.1016/j.jmps.2014.01.013>.
- [227] C. Morin, Z. Moumni, W. Zaki, Thermomechanical coupling in shape memory alloys under cyclic loadings : Experimental analysis and constitutive modeling, *Int. J. Plast.* 27 (2011) 1959–1980. <https://doi.org/10.1016/j.ijplas.2011.05.005>.
- [228] H. Soul, A. Isalgue, A. Yawny, V. Torra, F.C. Lovey, Pseudoelastic fatigue of NiTi wires : frequency and size effects on damping capacity, (2010). <https://doi.org/10.1088/0964-1726/19/8/085006>.
- [229] C. Grabe, O.T. Bruhns, Tension / torsion tests of pseudoelastic , polycrystalline NiTi shape memory alloys under temperature control, 482 (2008) 109–113. <https://doi.org/10.1016/j.msea.2007.03.117>.
- [230] Y.J. He, Q.P. Sun, Frequency-dependent temperature evolution in NiTi shape memory alloy, (2010). <https://doi.org/10.1088/0964-1726/19/11/115014>.
- [231] R. Slavkovic, Development of Stress-Induced Martensitic Transformation in TiNi Shape Memory Alloy, 23 (2014) 2505–2514. <https://doi.org/10.1007/s11665-014-0959-y>.
- [232] Y. You, X. Gu, Y. Zhang, Z. Moumni, G. Anlas, W. Zhang, Effect of thermomechanical coupling on stress-induced martensitic transformation around the crack tip of edge cracked shape memory alloy, *Int. J. Fract.* 216 (2019) 123–133. <https://doi.org/10.1007/s10704-019-00346-0>.

- [233] R.O.R. J.M. Stankiewicz, S.W. Robertson, Fatigue-crack growth properties of thin-walled superelastic austenitic Nitinol tube for endovascular stents, *J. Biomed. Mater. Res. Part A*. 33 (2015) 97–103. <https://doi.org/10.1002/jbm.a>.
- [234] A.L. McKelvey, R.O. Ritchie, Fatigue-crack growth in the superelastic endovascular stent material nitinol, *Mater. Res. Soc. Symp. - Proc.* (1999). [https://doi.org/10.1002/\(SICI\)1097-4636\(19991205\)47:3<301::AID-JBM3>3.0.CO;2-H](https://doi.org/10.1002/(SICI)1097-4636(19991205)47:3<301::AID-JBM3>3.0.CO;2-H).
- [235] L. Xu, A. Solomou, T. Baxevanis, D. Lagoudas, Finite strain constitutive modeling for shape memory alloys considering transformation-induced plasticity and two-way shape memory effect, *Int. J. Solids Struct.* (2020). <https://doi.org/10.1016/j.ijsolstr.2020.03.009>.
- [236] D. Ghodsiyeh, A. Golshan, J.A. Shirvanehdeh, Review on current research trends in wire electrical discharge machining (WEDM), *Indian J. Sci. Technol.* 6 (2013) 154–166. <https://doi.org/10.1016/j.ijmachtools.2006.08.026>.
- [237] Y. Xiao, P. Zeng, L. Lei, Experimental observations on mechanical response of three-phase NiTi shape memory alloy under uniaxial tension, *Mater. Res. Express*. 3 (2016) 105701.
- [238] P. Sedmák, J. Pilch, L. Heller, J. Kopeček, J. Wright, P. Sedlák, M. Frost, P. Šittner, Grain-resolved analysis of localized deformation in nickel-titanium wire under tensile load, *Science* (80-.). 353 (2016) 559–562. <https://doi.org/10.1126/science.aad6700>.
- [239] A. Duval, M. Haboussi, T. Ben Zineb, Modelling of localization and propagation of phase transformation in superelastic SMA by a gradient nonlocal approach, *Int. J. Solids Struct.* 48 (2011) 1879–1893. <https://doi.org/10.1016/j.ijsolstr.2011.02.019>.
- [240] Y. Chen, O. Tyc, O. Molnárová, L. Heller, P. Šittner, Tensile Deformation of Superelastic NiTi Wires in Wide Temperature and Microstructure Ranges, *Shape Mem. Superelasticity*. 5 (2019) 42–62. <https://doi.org/10.1007/s40830-018-00205-2>.
- [241] L. Wang, P. Feng, Y. Wu, A Temperature-Dependent Model of Shape Memory Alloys Considering Tensile-Compressive Asymmetry and the Ratcheting Effect, (2020).
- [242] L. Wang, P. Feng, Y. Wu, Z. Liu, A tensile-compressive asymmetry model for shape memory alloys with a redefined martensite internal variable, *Smart Mater. Struct.* 28 (2019). <https://doi.org/10.1088/1361-665X/ab3e12>.
- [243] K.E.N. Gall, N. Yang, H. Sehitoglu, Y.I.Y. Chumlyakov, Fracture of precipitated NiTi shape memory alloys, ... *J. Fract.* (2001) 189–207. <http://www.springerlink.com/index/u5812666h676p740.pdf>.
- [244] X.M. Wang, W. Cao, C.H. Deng, H. Liu, J. Pfetzinger-Micklich, Z.F. Yue, The effect of notches on the fatigue behavior in NiTi shape memory alloys, *Mater. Sci. Eng. A*. 610 (2014) 188–196. <https://doi.org/10.1016/j.msea.2014.04.109>.
- [245] R. Ní Ghriallais, M. Bruzzi, A Computational Analysis of the Deformation of the Femoropopliteal Artery With Stenting, *J. Biomech. Eng.* 136 (2014) 071003. <https://doi.org/10.1115/1.4027329>.
- [246] J.H. Rogers, J.R. Laird, Overview of new technologies for lower extremity revascularization, *Circulation*. 116 (2007) 2072–2085. <https://doi.org/10.1161/CIRCULATIONAHA.107.715433>.
- [247] R.M. Conroy, I.L. Gordon, J.M. Tobis, T. Hiro, S. Kasaoka, E.A. Stemmer, S.E. Wilson, Angioplasty and stent placement in chronic occlusion of the superficial femoral artery: Technique and results, *J. Vasc. Interv. Radiol.* 11 (2000) 1009–1020. [https://doi.org/10.1016/S1051-0443\(07\)61331-1](https://doi.org/10.1016/S1051-0443(07)61331-1).
- [248] K.K. Kapnis, D.O. Halwani, B.C. Brott, P.G. Anderson, J.E. Lemons, A.S. Anayiotos, Stent overlapping and geometric curvature influence the structural integrity and surface characteristics of coronary nitinol stents, *J. Mech. Behav. Biomed. Mater.* 20 (2013) 227–236. <https://doi.org/10.1016/j.jmbbm.2012.11.006>.
- [249] Y. Lin, X. Tang, W. Fu, R. Kovach, J.C. George, D. Guo, Stent Fractures After Superficial Femoral Artery Stenting, *J. Endovasc. Ther.* 22 (2015) 319–326. <https://doi.org/10.1177/1526602815580783>.
- [250] D. Scheinert, S. Scheinert, J. Sax, C. Piorkowski, S. Bräunlich, M. Ulrich, G. Biamino, A. Schmidt, Prevalence and clinical impact of stent fractures after femoropopliteal stenting, *J. Am. Coll. Cardiol.* 45 (2005) 312–315. <https://doi.org/10.1016/j.jacc.2004.11.026>.
- [251] A. Babaev, P. Hari, S. Zavlunova, A. Kurayev, Role of nitinol stent fractures in the development of in-stent restenosis in the superficial femoral artery, *Vasc. Dis. Manag.* 13 (2016) 7–16.
- [252] F. Auricchio, A robust integration-algorithm for a finite-strain shape-memory-alloy superelastic model, *Int. J. Plast.* 17 (2001) 971–990. [https://doi.org/10.1016/S0749-6419\(00\)00050-4](https://doi.org/10.1016/S0749-6419(00)00050-4).
- [253] W. Wu, M. Qi, X.P. Liu, D.Z. Yang, W.Q. Wang, Delivery and release of nitinol stent in carotid artery and their interactions: A finite element analysis, *J. Biomech.* 40 (2007) 3034–3040. <https://doi.org/10.1016/j.jbiomech.2007.02.024>.
- [254] Information on: <http://www.fda.gov>, U.S. Food and Drug Administration, IntraCoil® SelfExpanding Peripheral Stent, SUMMARY OF SAFETY AND EFFECTIVENESS DATA, (n.d.).
- [255] H.M. Paranjape, B. Ng, I. Ong, L. Vien, C. Huntley, Phase transformation volume amplitude as a low-cycle fatigue indicator in nickel–titanium shape memory alloys, *Scr. Mater.* 178 (2020) 442–446. <https://doi.org/10.1016/j.scriptamat.2019.12.014>.